Mathematical Modeling of Neuronal Dynamics during Disease

Christoffer Gretarsson Alexandersen
Linacre College
University of Oxford

A thesis submitted for the degree of
Doctor of Philosophy

Hilary 2024

Abstract

We currently do not understand how neuronal activity leads to cognition. However, we can observe how neuronal activity changes as cognition becomes abnormal. Brain diseases tell us what aspects of neuronal functioning are necessary to maintain brain function and cognition. An essential step to understanding brain function is knowing how to fix it as it becomes dysfunctional. However, studying brain diseases in humans can be challenging because these conditions often span years or decades, making longitudinal studies difficult. Additionally, researchers are restricted to noninvasive measurement methods when studying human subjects. As a result, neuroscience is relying increasingly on quantitative sciences to find patterns in large and complex datasets. Mathematical modeling has become an essential tool to assimilate biological theories and test them in light of experimental data. In this thesis, we study the mathematical modeling of brain diseases. We cover various aspects of modeling, such as developing and analyzing new model formulations, simulating large-scale mathematical models of the human brain, and fitting them to data. First, we integrate mathematical models of Alzheimer's disease progression and neuronal activity, showing that toxic proteins may cause alterations in brain activity consistent with clinical observations. Second, we develop a model for how neuronal activity affects disease progression, demonstrating the pivotal role neuronal activity plays in shaping disease trajectories. Third, we fit a model for brain-wide neuronal activity to brain cancer patients, discovering significant alterations in brain dynamics. Overall, we develop and analyze mathematical models to study brain diseases and their impact on neuronal activity, demonstrating the benefit of mathematical modeling in studying the mechanisms of brain disease.

Contents

Chapter 1

Introduction

The diseases of the brain not only harm us but change the very fabric of our being. Despite valiant efforts spanning decades of research, most brain diseases—such as Alzheimer's disease, Parkinson's disease, and frontotemporal dementia—are incurable. Brain diseases are challenging to study, as quantitative measurements of the human brain are restricted to post-mortem surgery and noninvasive imaging techniques. As such, building an understanding of brain diseases is a formidable challenge. Some neuroscientists have thus turned to theory, using mathematical models to test their hypotheses about disease mechanisms [1, 2]. Furthermore, mathematical modeling can predict disease trajectories and inform new treatment strategies [3–7]. Perhaps most importantly, mathematics provides a language to express scientific theories quantitatively, allowing us to understand these devastating diseases more deeply [8].

Most classes of brain diseases, such as neurodegenerative disease, involve temporal and spatial progression. That is, the disease initiates in some brain region and then *spreads* to other parts of the brain. In neurodegenerative disease, many clinicians believe that the progression of the disease is mediated by the spreading of toxic proteins throughout the brain [9, 10]. For example, in Alzheimer's disease, the toxic proteins amyloid-β and tau propagate throughout the brain, damaging neural tissue on the way [11]. As a disease spreads throughout the brain, symptoms appear. Neuroimaging technologies such as electroencephalography (EEG) and magnetoencephalography (MEG) measure the activities of neurons across the brain. These techniques have demonstrated reproducible changes in neuronal activity specific to different diseases. For example, in Alzheimer's disease, the frequency of neuronal firing slows down [12–14], whereas in brain cancer, there is a surge in activity near tumors [15, 16].

Mathematical neuroscience has a long history, dating back to the Hodgkin-Huxley neuron model [17]. However, we must zoom out to a larger scale to understand neuronal activity at the brain level. Neural mass models are a class of mathematical models designed to capture the behavior of neuronal *populations* as opposed to single neurons. These models typically describe the average activity levels of a neuronal population. Moreover, to study neuronal dynamics at the whole-brain scale, neural masses may be coupled together on brain networks called *connectomes* [18, 19]. These brain networks are constructed using neuroimaging techniques and represent the physical structure of the brain [20].

Since neurodegenerative diseases spread throughout the brain, models of spreading processes on networks have been applied to brain disease modeling [2, 21]. These models typically propagate on the same brain networks as the whole-brain neural mass models, as many diseases appear to spread from neuron to neuron via their physical connections [22, 23]. Mathematical models of disease progression and neuronal dynamics have both been studied extensively in isolation. However, research combining these mathematical models has been limited.

In this thesis, we explore the application of mathematical modeling to gain insights into brain diseases, such as neurodegenerative disease and brain cancer. To better understand the underlying mechanisms of neurological diseases, we create mathematical models that combine the modeling of disease progression with the modeling of neuronal activity.

More precisely, we focus on the following research questions: (1) In Alzheimer's disease, are changes in neuronal activity caused by the spreading of toxic proteins? (2) How does neuronal activity impact the progression of neurodegenerative diseases? (3) How do brain tumors affect neuronal activity? The first and second questions are investigated by analyzing and simulating novel mathematical model formulations. The third question is explored by fitting an existing mathematical model to clinical data. The thesis is structured as follows:

- In Chapter 2, we cover the basics of neurobiology. We introduce the concept of neurons and the structure of the human brain, represented as a network. Moreover, we introduce noninvasive methods to measure neuronal activity and how it is affected by diseases such as Alzheimer's disease and brain cancer. This chapter provides the necessary background to formulate mathematical models of neuronal activity and disease, as presented next.

- In Chapter 3, we introduce mathematical models of neuronal activity and disease. First, we discuss models for the local dynamics of neuronal activity. Second, we construct mathematical models of neuronal activity at the whole-brain scale using brain networks. Third, we formulate models for the spreading of brain diseases throughout the brain. These models will form the basis for the following chapters.

- In Chapter 4, we formulate a multiscale model of Alzheimer's disease combining models of disease progression and neuronal dynamics. The model captures how Alzheimer's disease propagates throughout the brain and its effect on neuronal activity. We test a recently proposed hypothesis of Alzheimer's disease mechanism and demonstrate that it successfully reproduces the hallmark changes in neuronal activity seen in patients. However, this model ignores the impact neuronal activity can have on disease spreading. This chapter is based on the paper by Alexandersen *et al.* [24].

- In Chapter 5, we formulate a mathematical model to capture how neuronal activity affects disease progression. It has recently become clear from clinical research that the spreading of neurodegenerative disease is affected by neuronal activity. Analyzing our mathematical model, we find that neuronal activity can accelerate disease progression and induce symmetry breaking in spreading patterns. Nonetheless, we have not yet investigated pathological neuronal activity quantitatively in light of clinical data. This chapter is based on the preprint by Alexandersen *et al.* [25].

- In Chapter 6, we incorporate clinical data into a whole-brain neural mass model to study the effect of brain cancer on neuronal dynamics. Using neuronal activity measurements of brain cancer patients, we find that cancer patients have stronger communication between brain regions than healthy controls and that tumors contribute to this difference. This chapter is based on the preprint by Alexandersen *et al.* [26].

- In Chapter 7, we discuss future directions and challenges in applying mathematical modeling to brain diseases.

Mathematical models enable quantitative predictions, making them invaluable tools in understanding neurological phenomena, including brain diseases. These models help formulate hypotheses about disease mechanisms, explain changes in neuronal dynamics, and uncover novel theories of the workings of our brain.

Chapter 2

The neurobiology of disease

The human brain is a remarkably complex organ responsible for generating all of our thoughts and emotions. Its vast and intricate network of neurons gives rise to these complicated cognitive processes. However, neurological disease can disrupt the normal functioning of these neurons, leading to cognitive dysfunction and even death.

This chapter provides an introduction to basic neurobiology and disease mechanisms, with a focus on Alzheimer's disease and brain cancer. First, we discuss the fundamental concept of neurons, followed by an overview of the structure of the human brain and its representation as a brain network. Second, we explore oscillatory brain activity and its connection to cognition. Third, we introduce neurodegenerative diseases like Alzheimer's disease, as well as brain cancer. Finally, we discuss the impact of these diseases on brain activity. This chapter provides the essential information to create mathematical models of brain disease and neuronal activity, which will be discussed in the next chapter.

2.1 Morphology and function of neurons

Neurons are the basic building blocks of the nervous system. In the human brain, the number of neurons is estimated to be over 120 billion [27]. Although our focus will remain on neurons, it is worth mentioning that they are not alone. Neurons enjoy the company of a diverse family of cell types called glia, which play a part in inflammatory responses, homeostasis, and many other physiological processes [28]. Our main attention will be directed towards neuronal cells, however, as the mathematical models we will be discussing do not take the glia into account.

Neurons have three main components: cell bodies, dendrites, and axons. The cell body is the home of all the organelles necessary for a cell to survive and function. It is from the cell body that dendrites and axons protrude. The dendrites are highly

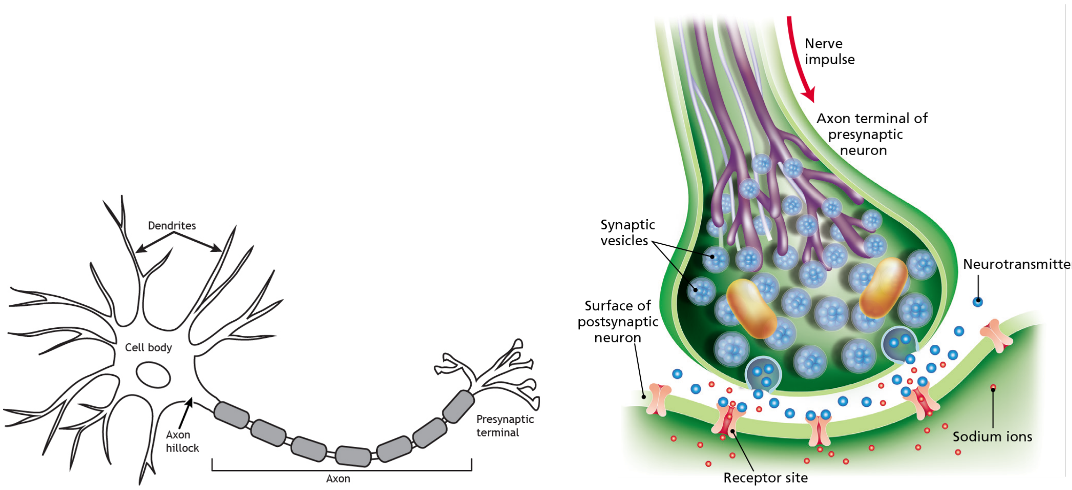

(a) (b)

Figure 2.1: *(a)* The main components of a neuron. The cell body contains the cell contents itself. Dendrites protrude out of the cell body and branch extensively. The axon does not branch (at least not as extensively). The axon hillock is a structure marking the beginning of the axon. Presynaptic terminals form at the end of axons. These presynaptic terminals will connect to the dendrites of other neurons. Figure taken from Henley [29]. *(b)* The synapse consists of the presynaptic axon terminal and the postsynaptic dendrite. As an action potential reaches the axon terminal, neurotransmitter vesicles are released into the synaptic cleft. The neurotransmitters bind to the receptors on the postsynaptic dendrite receptors. These receptors induce changes in ion permeability through biochemical reaction pathways, increasing the chances of an action potential occurring in the postsynaptic neuron. Figure taken from Quinton [30].

branched structures emanating from the cell body [28]. A typical neuron will have several branches of dendrites, each up to 1mm in length. In contrast, neurons typically have only one axon, which can range in length from a few micrometers to a full meter. To use a computational metaphor: dendrites receive *input* from other neurons, the cell body *processes* the input, and the axon delivers *output* to other neurons.

The cell body of a neuron at rest has an accumulation of negative charge compared to the outside (extracellular) environment. This results in a negative voltage potential (relative to the outside of the cell). This negative potential is called the *resting potential* and lies between -60 and -90 mV. The negative resting potential is maintained by a mixture of diffusive and electrostatic forces acting on K^+ ions. The potassium levels inside the cell are higher than in the outside environment, as considerable amounts of energy are spent pumping K^+ into the cell using the sodium-potassium pump enzyme. As such, diffusive forces push K^+ out. Organic acids, phosphates, and other negatively charged molecules inside the cell produce an electrostatic force pushing

K^+ inside. As the transport of K^+ into and out of the cell reaches equilibrium, it so happens that the net ionic charge inside the neuron is negative, producing a negative resting potential. All of this is possible due to the selective permeability of the neuron, leaving larger molecules and specific ions unable to leave and enter the cell body. This permeability can be regulated by ion channels in the cell membrane in order to change the membrane potential, an essential feature to produce action potentials.

Action potentials are characterized by a sudden increase in resting potential that propagates along the axon away from the cell body. As the neuron receives input from other neurons through its dendrites, its resting potential increases (also called depolarization). An action potential is elicited if the resting potential is increased beyond a threshold voltage level. This action potential then propagates through the neurons, providing input to other neurons at the other end of the axon. After a spike, the membrane potential decreases beyond the resting potential (also called hyperpolarization). The membrane potential then slowly approaches the resting potential again. The cell cannot produce other action potentials for a short period directly after an action potential; this is called the *aboslute refractory period*. The absolute refractory period limits the highest firing rate (average spikes per second) a neuron can achieve.

The rise and fall of the action potential are mediated through *voltage-gated ion channels*. These membrane protein channels are selectively permeable to a specific ion, and the membrane potential regulates their permeability. The orchestrated opening and closing of these channels give rise to the characteristic shape of the voltage potential. Put simply, as a neuron becomes depolarized by incoming action potentials from other cells, voltage-gated sodium channels open, leading to an influx of sodium ions. This causes the neuron to further depolarize. As the membrane potential increases, voltage-gated potassium channels open, causing potassium ions to leave the neuron, which causes hyperpolarization. These sequences of events lead to the rise and fall of the membrane potential, which also propagates spatially throughout the axon. The dynamics of ion channels opening and closing is at the heart of the Hodgkin-Huxley neuronal model [17], the canonical mathematical model of neuronal activity.

As the action potential propagates, it will eventually reach the end of the axon, called the *axon terminal*. Typically, axons terminate at the dendrites of other neurons. The axon terminal and dendrite form the *synapse*, the site of neuronal communication (see Fig. 2.1b). The action potential triggers the release of neurotransmitters from the axon terminal into the extracellular space between the axon and dendrite, called the *synaptic cleft*. The neurotransmitters then bind to receptors on the dendrite membrane, triggering changes in ion permeability. Some neurotransmitters such as glutamate are *excitatory*, increasing the chances of the postsynaptic cell (the neuron receiving the input) to elicit an action potential. Other neurotransmitters such as GABA are *inhibitory* and decrease the chance of eliciting an action potential in the postsynaptic neuron. The presynaptic neuron (the neuron releasing the neurotransmitters through its axon terminal) generally releases excitatory or inhibitory neurotransmitters only, though numerous exceptions exist. For this reason, neurons are broadly classified as either *excitatory* or *inhibitory* neurons. The balance between excitatory and inhibitory neuronal dynamics is central to mathematical models of neuronal activity, as we will see in Section 3.1.2, and is thought to give rise to oscillations in neuronal activity, as discussed in Section 2.4.

2.2 The anatomy and function of the human brain

As we will be considering mathematical modeling at the scale of the entire brain, it is instructive to introduce the basics of human brain structure. As discussed in the next section, network representations of the human brain are widely used in data analysis and mathematical modeling of whole-brain phenomena.

Together with the spinal cord, the brain is part of the central nervous system. The brain has a high fat content and comprises neurons, glial cells, and blood vessels. The brain has two main components: grey matter and white matter (see Fig. 2.2b). The grey matter is mainly on the folded outskirts of the brain, while the white matter is primarily in the inner section. Grey matter mainly contains the cell bodies of neurons, whereas white matter contains axons. The axons in the white matter are often long, connecting distant brain regions. These long axons are sheathed with myelin, a substance that increases conductivity along the axon. It is the myelin that gives the white matter its color. The grey matter gets its color from the higher density of cell bodies. Roughly speaking, the grey matter processes information, whereas the white matter transmits information [31].

The brain can be divided into three main structures: the cerebrum, the brainstem, and the cerebellum (see Fig. 2.2c). The cerebrum, which is the brain's largest part, includes the cerebral cortex (or cortex for short) which is the grey matter of the cerebrum. The cerebral cortex is split into two hemispheres and is responsible for muscle coordination, temperature regulation, speech, vision, hearing, emotion, learning, and problem-solving [32]. The brainstem connects the cerebrum to the spinal cord. It has a highly specialized structure and facilitates hearing, movement, and balance. The brainstem also regulates other physiological processes like breathing, blood flow, vomiting, and coughing. The cerebellum is the smallest part of the brain and has, like the cerebrum, two hemispheres. It is involved in posture, balance, and voluntary movements [31].

The cerebrum can be divided into four major parts, referred to as *lobes* (see Fig. 2.2a). These four lobes have somewhat specialized functions, though much of cognition is decentralized and involves the cooperation of different lobes. The brain has four lobes: frontal, parietal, occipital, and temporal. The frontal lobe controls decision-making, movement, and speech. The parietal lobe handles pain, speech comprehension, and orientation. The occipital lobe processes vision and the temporal lobe manages short-term memory, speech, and musical rhythm. Furthermore, the front and back of the cortex are referred to as the *anterior* and *posterior* cortex [31, 32].

Roughly speaking, the cortex consists of two neuron classes: excitatory and inhibitory neurons. Approximately 25% of the cortical neurons are inhibitory, while the remaining 75% are excitatory. This ratio is relatively constant across species and is thought to be crucial to cognitive function [33]. The relative contribution of excitation and inhibition in the cortex is called the excitatory-inhibitory balance (EI balance) and is a fundamental concept in the study of neuronal activity. Most inhibitory and excitatory neurons connect to nearby neurons. However, some neurons have long-range axons. These long-range connections extend through the white matter and connect to distant neurons, often in other lobes. Most of the long-range connections in the brain are formed by excitatory neurons that connect with other excitatory neurons [34]. The ratio of excitatory-to-inhibitory neurons and the absence of inhibitory long-range connections are widely used to constrain mathematical models of neuronal activity (see Section 3.1.2).

Some additional structures in the brain collectively form the *limbic system* (see Fig. 2.2d). Important structures of the limbic system include the hypothalamus, amygdala, and hippocampus. The hypothalamus regulates temperature, sleep, hunger, and thirst. The amygdala—of which there are two, one in each hemisphere— regulates emotion and stress. The hippocampus—of which there are also two—is involved in memory, learning, and navigation [31].

Our interest lies in cognition and its detriment due to disease, so we are primarily concerned with the cerebral cortex. There are exceptions, however. For example, the hippocampus is affected by Alzheimer's disease and is the primary suspect in memory-related symptoms. Nonetheless, most of our knowledge of brain activity stems from the cortex and will be the focus for the next couple of sections.

2.3 The human brain as a network

In studying the structure and function of the brain, it is helpful to represent it as a network. A network in which nodes represent brain regions and links represent axonal connections is called a *structural connectome*. These brain networks form the foundation for data analysis and mathematical modeling of brain structure and function. It should be noted, though, that many brain networks do not include all parts of the brainstem and often ignore the cerebellum completely. In other words, structural connectomes mainly focus on the cortex (cerebrum). It should be mentioned that some neuroscientists are critical of this network-centric perspective, preferring a continuum-based view [36, 37].

The links of a connectome are constructed using diffusion tensor imaging (DTI) and tractography [20, 38]. DTI measures the direction in which water molecules diffuse, which, incidentally, is parallel to the direction of white-matter axonal fibers. The water diffusion tensors are then used to represent axonal fibers with directional voxels. Tractography is the process of estimating fiber pathways by tracking the voxel directions. As such, tractography produces a 3D map of the axonal pathways in the brain (shown in upper-left of Fig. 2.3a).

The nodes of a connectome are constructed from a parcellation, which is a map splitting the 3D structure of the brain into N discretized gray-matter regions (shown in lower-left of Fig. 2.3a). As such, the spatial extent and size of brain regions are dependent on the particular parcellation. The connectome is finally assembled by connecting these regions with tractography-estimated white-matter fibers. Multiple fibers may connect the same brain regions and are combined. Moreover, each estimated fiber has a length. Typically, connectome links are supplemented with information on the number of fibers and their respective lengths. Connectome graphs constructed this way are undirected, as DTI does not differentiate between afferent and efferent axonal fibers [38]. An example of a structural connectome is given in Figure 2.3a.

Typically, an N-node connectome graph is described by the N-by-N weighted adjacency matrix $\mathbf{W}$ in which a nonzero ijth-element denotes a link between node i and j. The definition of the link weights (elements of the weighted adjacency matrix) may vary but are usually inversely related to the distance between nodes. An example

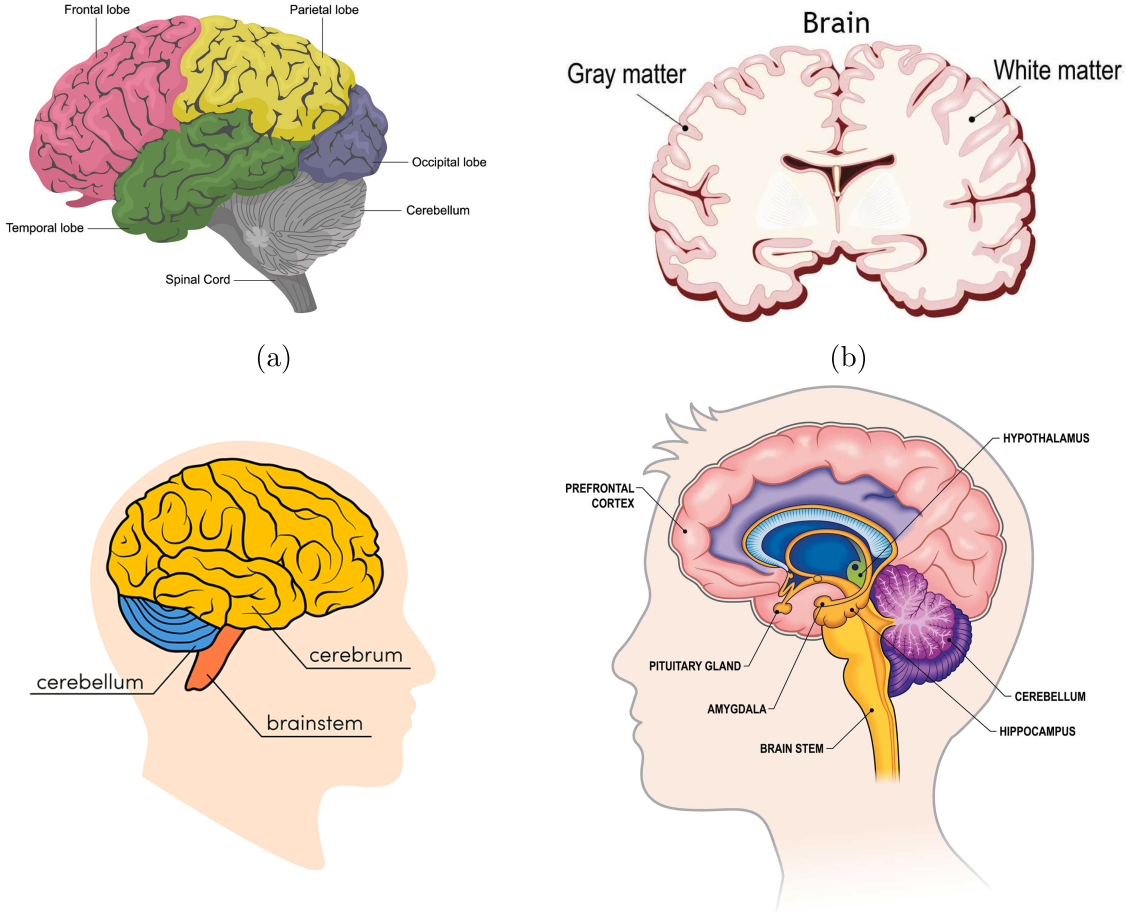

(a) (b) (c) (d)

Figure 2.2: *(a)* The different lobes of the human cortex. These are usually credited with information processing, cognition, and problem-solving. *(b)* The brain consists of grey and white matter. The grey matter contains neurons, whereas the white matter contains axons connecting physically distant brain regions. *(c)* The human brain can be broadly separated into the cerebrum, cerebellum, and brain stem. *(d)* The limbic system consists of highly specialized brain structures found on the border between the brain stem and cortex. Figures are taken from *Brain Anatomy and How the Brain Works* [35].

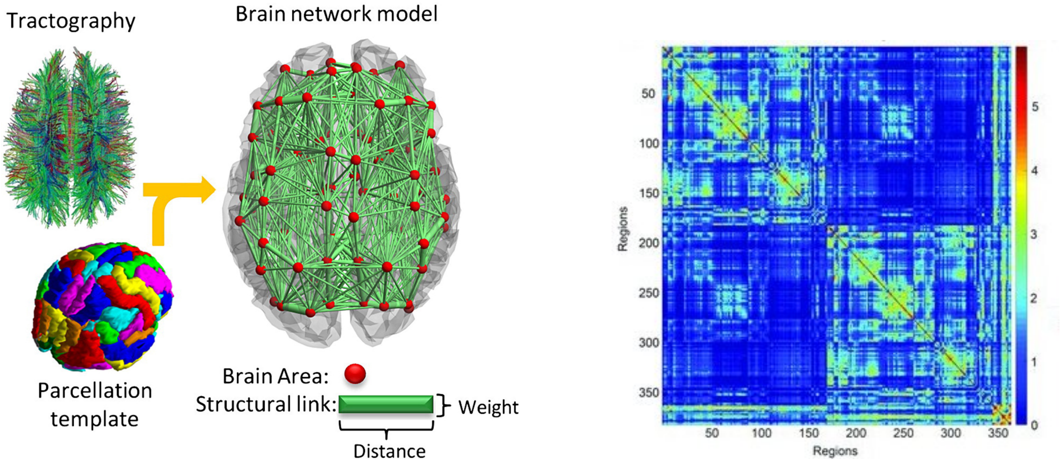

(a) (b)

Figure 2.3: *(a)* A simplified overview of the construction process of a structural connectome. A parcellation spits the brain into discrete regions, which will become the nodes of the connectome. Tractography maps the axonal bundles of the brain, which are used to create the links in the connectome. The nodes (parcellation) and links (tractography) are put together to form a structural connectome, a network of the brain. *(b)* A matrix representation of a structural connectome. Figures taken from Cabral *et al.* [39] and Stefanovski *et al.* [40].

of a structural connectivity matrix is given in Figure 2.3b. These connectome matrices are essential features of the whole-brain models we will introduce in Chapter 3. Having now discussed the structural aspects of the brain, we move on to its functional aspects and, in particular, neuronal dynamics at a larger scale.

2.4 Oscillatory neuronal activity: brain waves

When large networks of neurons synchronize and fire in unison, they often fire in waves. At first, the neurons fire rapidly, then slow down, then fire rapidly again, slow down, and so on. This behavior is reflected in the electromagnetic field at the scalp of the brain. When electrodes are placed on the brain's scalp, one can see waves in the electric potential readings. This phenomenon is called brain waves (also brain rhythms or neural oscillations). These brain waves are thought to originate from the interplay between excitatory and inhibitory neurons. Moreover, brain waves have been hypothesized to play a pivotal part in cognition and can be measured noninvasively without requiring surgery. As such, brain waves are extensively studied, as they can be measured by relatively cheap and ethical methods. Many mathematical models of neuronal activity focus on phenomena related to brain waves [41, 42].

2.4.1 Cognitive function of brain waves

The discovery of brain waves was made nearly a century ago. Electrodes were placed on the scalp of subjects asked to sit and relax (see Fig. 2.4a). Doing so, brain waves with 10 Hz frequencies were present when the subjects closed their eyes (see Fig. 2.4b) and disappeared once the eyes were opened again. These 10 Hz brain waves are known today as *alpha waves*, which are prominent during resting conditions in the posterior (towards the back) lobes. The alpha waves contribute to idle mental behavior and inward attention [43].

Brain waves operating at other frequencies have been discovered and contribute to different cognitive functions [44]. Accordingly, brain waves are categorized by their frequencies into *frequency bands*: delta (0.5–4Hz), theta (4–8Hz), alpha (8–12Hz), beta (12–30Hz), and gamma (30–120Hz).

Delta oscillations are a key characteristic of sleep, anesthesia, and sedation [45]. Theta oscillations are linked to memory encoding and retrieval [46]. Beta oscillations are prominent in motor tasks, such as reaching and pushing [47]. Gamma oscillations are particularly active during memory formation [48] and seem to couple distant brain regions during learning tasks [49]. Moreover, cross-correlations between different frequency bands may be related to cognitive function as well [50].

2.4.2 Measuring brain waves

Electroencephalogram (EEG) and magnetoencephalogram (MEG) are non-invasive technologies that record brain rhythms. EEG/MEG (which we will refer to as E/MEG from now on) measures the changes in the electromagnetic field recorded across the subject's scalp. EEG uses electrodes placed directly on the subject's scalp, whereas MEG uses a sensitive magnetometer placed on the head like a helmet. As neurons fire in unison, the flux of ions into the cell bodies induces changes in the surrounding electromagnetic field. However, for the changes in the electromagnetic field to be detectable at the brain's scalp, tens to hundreds of thousands of neurons must synchronize. As such, E/MEG measures the synchronized firing of large populations of neurons. Both methodologies have excellent time resolution, though MEG has a significantly better spatial resolution than EEG. EEG remains more popular, however, as MEG equipment is substantially more expensive than their EEG counterparts [51].

E/MEG signals have to be heavily preprocessed to study brain waves. Signal artifacts must be removed due to head movement, muscle twitches, and heart rate

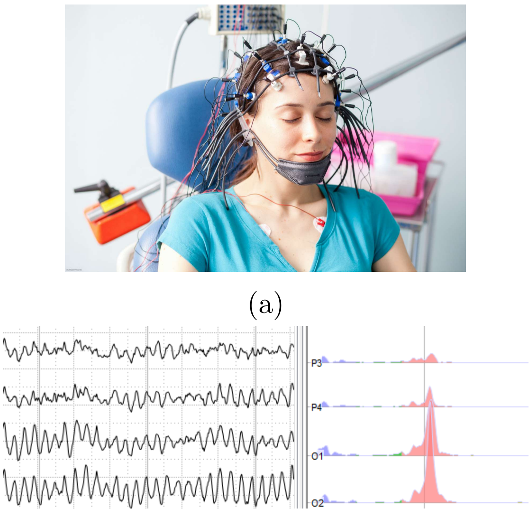

(a)

(b)

Figure 2.4: *(a)* An example of an EEG set-up. Electrodes are put on the subject's scalp, measuring the surface electric potential. Only the synchronized activity of tens of thousands of neurons induces a strong enough change in the electric potential to be measured. *(b)* Examples of EEG signals at four different recording sites with the actual signal on the left and the spectral density of the corresponding signals to the right. The subject is recorded in resting state and exhibits neural oscillations in the alpha range. Figures are taken from *EEG Recording and Brain Waves — BioSerendipity* [52] and Cherninskyi [53], respectively.

fluctuations. Moreover, the signals recorded at each sensor (electrode or magnetometer) must be related to brain regions. A connectome parcellation defines these brain regions (see Section 2.3). This is an infamously difficult *inverse problem*, asking what signal from the *brain regions* can give rise to the observed signals at the *sensors*. The signals emanating from the brain regions will mix into the sensor signals, making the transformation from sensors to brain regions difficult. Sophisticated computational methods to solve the inverse problem in E/MEG exist but will not be discussed here. These processed signals can, for example, be used to diagnose epileptic patients and identify which regions are initiating their seizures.

To study brain waves, however, more processing is needed. E/MEG signals are riddled with noise, so brain waves are not always apparent to the human eye. Computing the power spectra of E/MEG signals reveals that the noise has a strong $1/f$-component (pink noise, see Fig. 2.9). The power spectrum decays according to $1/f^\alpha$ where f is the frequency and $\alpha > 0$. Brain waves are thus identified as components in the power spectra that deviate from the $1/f$ component. The spectral properties of the signals reveal which frequency of brain waves are present; researchers can determine which brain waves are present during different conditions such as resting state, problem-solving, or exercise. Moreover, neuroscientists hypothesize that brain waves are a means of communication between brain regions [54]. As such, correlations in brain waves between regions are of great interest.

2.4.3 Correlations in brain activity: functional connectivity

When studying brain wave correlations, E/MEG signals are first filtered into a frequency band. For example, the E/MEG signal may be filtered into the alpha band (8–12 Hz) using a Butterworth filter. After the signal in each brain region has been filtered, correlations between the regions can be computed. A zoo of correlation metrics exists for studying brain waves. These brain wave correlations are collectively called *functional connectivity*[1]. The motivation behind this term is that if two brain regions have correlated brain waves, they are thought to activate each other to achieve some cognitive function. The study of functional connectivity is a research field in and of itself [55].

Brain activity correlations can be measured in the time or frequency domain [56]. In the time domain, the processed E/MEG signal is compared directly. Common choices for time-domain FC metrics are Pearson correlation, cross-correlation, mutual information, and Granger causality [55, 56].

Due to the importance of brain wave frequency, it is common to compute correlations in the frequency domain. The frequency-domain correlations are designed to capture a sense of *synchronicity* between brain regions, which is believed to reflect neuronal communication. As such, the processed E/MEG signal is often transformed to amplitude-phase space by the Hilbert transform, where correlations can be computed from amplitudes and phases. Popular choices of frequency-domain correlation metrics are the coherence coefficient, envelope correlation, phase-locking value, and phase-lag index [56, 57]. The coherence coefficient is simply the cross-correlation computed in the frequency domain. The envelope correlation is the Pearson correlation of the amplitude of the Hilbert-transformed signals. The phase-locking value is the modulus of the complex-valued phase difference between two signals averaged over time.

---

[1] Functional connectivity also refers to correlations between signals measured by functional magnetic resonance imaging (fMRI). There are also oscillatory signals in fMRI, though these occur at a much slower frequency than E/MEG. The oscillations found in fMRI are not considered brain waves and are not discussed here.

When the E/MEG signal is transformed from sensor space to region space, components of the sensors may bleed into separate regions, leading to components in the region-space signal that are perfectly synchronized. These spurious correlations are synchronized with zero lag. Hence, several metrics, such as the phase-lag index, are designed to remove these zero-lag correlations. The phase-lag index (PLI) [57] is computed as follows

$$\mathrm{PLI}(x, y) = |\langle \mathrm{sign}\,(\sin(\theta_x - \theta_y))\rangle_t|, \tag{2.1}$$

where θ_k is the phase of the Hilbert transform of signal k and $\langle \cdot \rangle_t$ is the time average. The PLI measures the consistency of the phase difference over time. For example, if signal x is leading in phase ahead of signal y for all time, then $\mathrm{PLI}(x, y) = 1$. The PLI is symmetric, so the same goes if y leads ahead of x. If signals x and y swap lead randomly, the PLI will be close to zero. If x and y are perfectly synchronized, the PLI is also zero; hence, as promised, PLI ignores zero-lag correlations. Note that the PLI formula takes the absolute value to avoid negative values and constrains its value between 0 and 1. This is done to simplify analysis when combining functional connectivity into a network. In Chapter 6, we fit a whole-brain model of neuronal activity to empirical PLI.

Functional connectivity (FC) of brain waves is often represented as a network. As FCs are correlations between brain regions, one can construct a corresponding correlation matrix, referred to as a functional connectivity matrix. Figure 2.6 illustrates how FC matrices are typically constructed. These FC matrices can naturally be interpreted as networks, in which the brain regions are nodes and their functional connectivities are the links. The FC matrices are the weighted adjacency matrices of functional connectivity networks (see Fig. 2.5 for examples).

As such, network science tools lend themselves naturally to studying functional connectivity. Community detection has identified several tightly-connected clusters in FC graphs [59]. Though many of these FC clusters are controversial, a few have been endorsed by the neuroscientific community. For example, the default-mode network is a collection of brain regions that co-activate during resting-state conditions and has been reproduced reliably by various research groups. Other networks include the visual, somatosensory, and central executive networks. Psychiatric disorders and neurological diseases often feature changes to functional connectivity [60, 61]. Moreover, one of the main goals of mathematical models of neuronal activity at the whole-brain scale is to explain and predict functional connectivity patterns (discussed in Section 3.1.3).

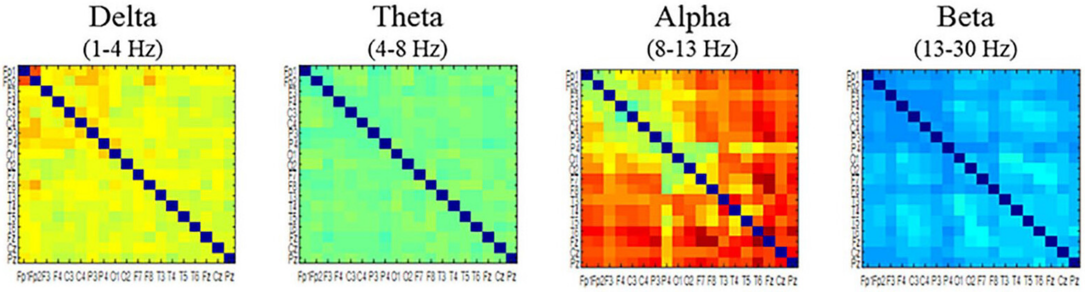

Figure 2.5: Functional connectivity computed for various frequency bands. The EEG signal was preprocessed and filtered into separate frequency bands, after which their phases were computed using the Hilbert transform. Correlations between the phases were then computed by the phase-lag index (2.1). The matrices contain the phase-lag indices computed between each region pair. The PLI matrices are symmetric because the PLI is a symmetric correlation measure. The figure is taken from Mohammadi & Moradi [58].

2.5 Summary of healthy neurobiology

Using a computational metaphor: neurons are processing units. They receive input from other neurons, and if that input surpasses a certain threshold, they emit output to other neurons in the form of action potentials. The reception, processing, and transmission of action potentials involve various cellular processes. Notably, the healthy functioning of neurons depends on the production of ion channels that regulate the voltage difference between neurons and their environment.

The human brain consists of the cerebrum, brainstem, and cerebellum. The cerebrum includes the cerebral cortex, the primary site of cognition. The cerebral cortex can be further split into four parts: the frontal lobe, parietal lobe, occipital lobe, and temporal lobe. These have somewhat separated functions and are connected by long-range axons. Connectomes are brain networks representing the physical structure of the brain.

The activity of neurons can be studied on the whole-brain scale using imaging methods such as EEG and MEG. These methods capture changes in the electromagnetic field induced by populations of neurons firing in synchrony. The synchronized firing appears as waves in the electromagnetic signals measured by E/MEG. These *brain waves*, also called neural oscillations and brain rhythms, are believed to play a pivotal role in cognition and overall brain health.

A standard method to study brain waves is to compute correlations between the brain waves in different regions. As such, regions that have synchronized neural oscillations are believed to be functionally coupled. Correlations between brain rhythms

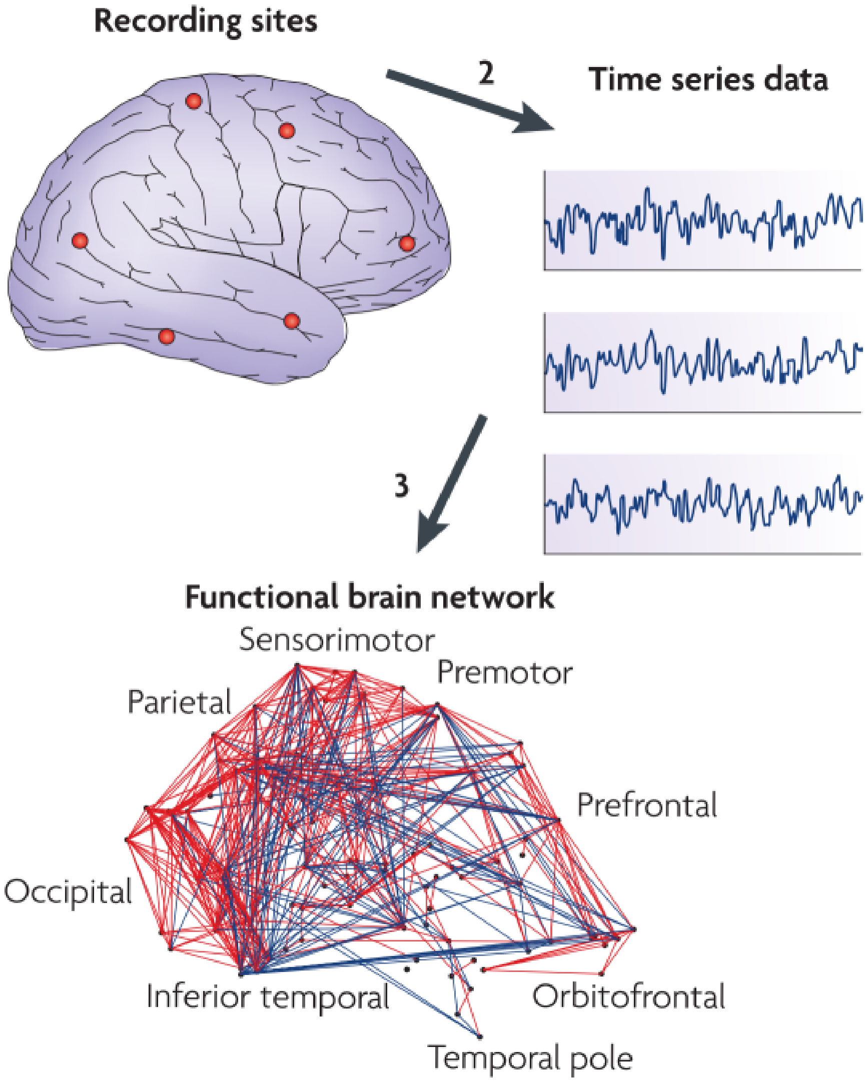

Figure 2.6: A pipeline for creating functional connectivity networks. Measurements are made at different recording sites on the brain using E/MEG or fMRI. These measurements are then transformed from sensor space to source (region) space. Correlations are then computed between the signals (neural oscillations) from different regions. The functional connectivity network consists of brain regions where the link weights are the correlation between these brain regions. Whether the network is directed or undirected depends on whether there is a sense of directionality in the correlation metric used. Figure taken from Bullmore & Sporns [62].

are referred to as *functional connectivity*. Changes in functional connectivity are abundant in neurological disorders, which are discussed in the next section.

2.6 Neurodegenerative diseases

Neurodegenerative disease is a class of brain diseases categorized by the accumulation of toxic proteins that spread progressively throughout the brain, deteriorating neural tissue as they go along. Another crucial characteristic of neurodegenerative disease is that the toxic proteins often spread from neuron to neuron via axonal connections [9]. Yet another characteristic is that the proteins found in neurodegenerative diseases are also present in healthy brains. During disease, these healthy proteins are turned into toxic variants of themselves. Neurodegenerative diseases can be classified into different types based on the proteins that accumulate during the disease [9]. These classes of neurodegenerative diseases with their respective proteins are amyloidosis (amyloid-β and prions), tauopathies (tau), synucleinopathies (α-synuclein), and TDP-43 proteinopathies (TDP-43). Diseases within these classes differ mostly in which regions are more vulnerable to neurodegeneration.

Amyloidoses are categorized by insoluble, fibrous proteins rich in β-sheets[2], such as amyloid-β and prion protein. Amyloidoses include Creutzfeldt-Jakobs disease and familial British dementia. The presence of hyperphosphorylated tau proteins categorizes tauopathies and includes diseases such as frontotemporal dementia[3]. Tau protein is known to be transported within axons and spread to other neurons at their synapses. Synucleinopathies include Parkinson's disease, where toxic α-synuclein spreads via axonal connections. Interestingly, neurons with higher neuronal firing rates have been shown to increase transport of tau and α-synuclein to their neighboring neurons [63–67]. TDP-43 proteinopathies include muscular atrophy and lateral sclerosis. Numerous other neurodegenerative diseases have been classified beyond those mentioned here.

Alzheimer's disease is unique as a neurodegenerative disease, as it has characteristics of amyloidosis and tauopathy. The presence of both amyloid-β and tau protein is a defining feature of Alzheimer's disease [68].

---

[2] β-sheets are a structural element of proteins consisting of interconnected strands that form a two-dimensional sheet.

[3] Phosphorylation is the process of adding a phosphate molecule to a protein and is one of the most common ways for a cell to regulate protein activity. When tau protein is excessively phosphorylated, it aggregates into bundles.

2.7 The neurobiology of Alzheimer's disease

Dementia is a syndrome categorized by memory dysfunction, language impairment, behavioral aberration, and many other symptoms [69, 70]. Severely diminishing the quality of life of those affected, the importance of dementia at an individual and societal level cannot be understated; as of 2018, an estimated 50 million people worldwide have dementia with an associated financial burden of 1 trillion USD [71].

AD is the most common cause of dementia. Initially, patients commonly exhibit only minor memory deficits before developing severe dementia over the span of 7–10 years [69, 72]. The underlying pathological hallmarks of AD can develop 10–20 years before dementia onset [72, 73]. As of date, there are no effective treatments for AD. However, recent—and somewhat controversial—FDA-approved antibody drugs may be a reason for cautious optimism [74–76].

Although AD is extensively studied, its pathological mechanism remains unknown. AD is characterized by the presence of amyloid-β (Aβ) proteins and hyperphosphorylated tau (τP)[4] protein filaments [72]. Amyloid-β aggregates are found outside the cell (intracellularly), whereas hyperphosphorylated tau (toxic tau) forms bundles inside the cell. AD is hypothesized to be a protein disorder mediated by the pathological self-aggregation of Aβ and tau. Neuronal loss and dysfunction follow as these proteins propagate throughout the brain, eventually causing the symptoms of dementia.

The prion-like hypothesis[5] of AD progression (see Figure 2.7) proposes that modified Aβ and tau aggregate into pathological oligomers[6] that spread throughout the brain [11, 77, 78]. The idea is that these modified (toxic) protein variants convert healthy variants upon contact and further bind to them, thus creating longer oligomers of the toxic protein variant. These oligomers are thought to (1) induce neurotoxic effects to their immediate surroundings, (2) spread either through axons or the extracellular space, and (3) further accelerate oligomerization at their new destinations. The oligomers eventually aggregate into insoluble fibrils called Aβ plaques and tau neurofibrillary tangles.

The prion-like mechanism is congruent with Aβ and τP spreading patterns during AD progression. The disease initiates with Aβ spreading diffusively in cortical regions [79] and later into the limbic system and cerebellum [80]. Later on, τP appears

---

[4] This notation for hyperphosphorylated tau protein is commonplace. The τ symbol stands for tau protein and the P symbolizes a phosphate molecule attached to it.

[5] Here, we use the term prion-like hypothesis for the propagation of both Aβ and tau, whereas other sources may use the term exclusively for one or the other. Recently, hypotheses involving spreading of both tau and Aβ has also been referred to as the dual-cascade hypothesis [77].

[6] Oligomers are larger molecules consisting of a few repeating, often identical, chemical species.

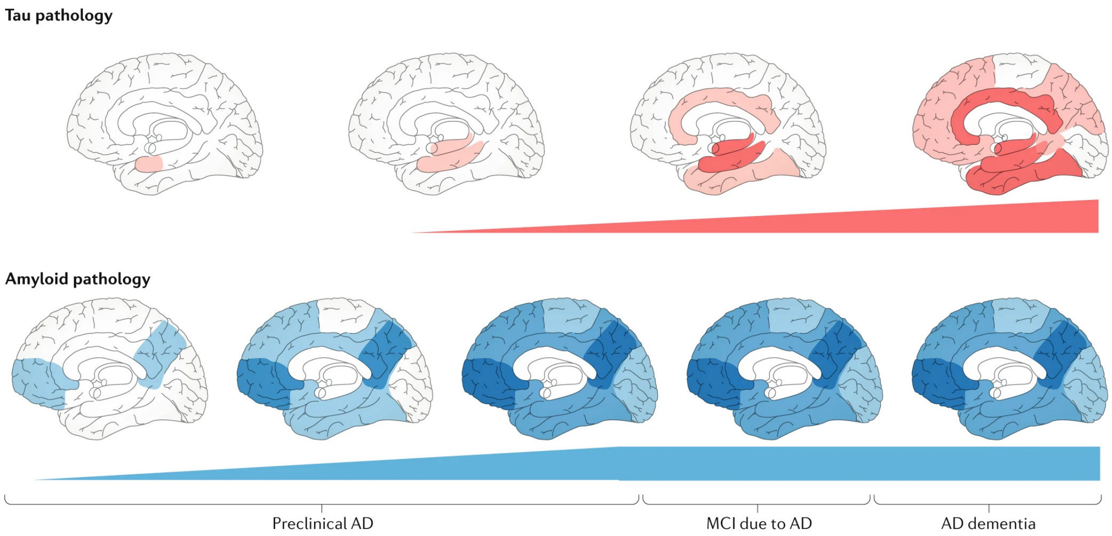

Figure 2.7: Illustrations of pathological tau and Aβ spreading during AD from the preclinical stages through MCI (mild cognitive impairment) to dementia. Figure cropped and reprinted from van der Kant *et al.* [77] .

first in the entorhinal cortex, located in the temporal lobe. Subsequently, τP spreads to the limbic system and later infiltrates other cortical regions [80]. In contrast to the diffusive spreading of Aβ, pathological tau spreads in a step-wise fashion following anatomical connections between brain regions [79, 81–83].

Studies also suggest that Aβ facilitates the propagation of τP during AD progression [83–86]. Although the presence of Aβ is the most reliable diagnostic criteria for AD [73], it is the spreading of pathological tau that shows the highest correlation with cognitive decline [79, 87] and neural loss [88]. Moreover, the propagation of toxic tau into cortical regions is believed to initiate the clinical phase of AD [89, 90].

There is intense, ongoing research into the mechanisms of τP and Aβ pathology at the cellular level. Recent findings highlight stark differences in how Aβ and τP affect neuronal circuits.

2.8 Mechanisms of Aβ and tau pathology

Aβ molecules are released into extracellular space by the cleavage of the transmembrane amyloid-precursor protein (APP). Genetic mutations in the APP processing apparatus correlate heavily with familial AD [91]. The normal functioning of APP and its cleavage product, Aβ, is largely unknown [92]. The APP cleavage site varies and produces Aβ molecules of varying length with varying propensities for aggregation [92]. Released Aβ can aggregate into soluble oligomers and larger, insoluble fibrils. Aggregations of such fibrils are referred to as Aβ plaques, from which oligomers can emanate. It has been increasingly clear that chiefly Aβ oligomers, not plaques, mediate neurotoxic effects [92].

Multiple studies have found that amyloid-β induces neuronal hyperactivity [93–98]. As such, Harris *et al.* [99] proposed a biphasic evolution of AD, where Aβ initially causes hyperactivation followed by τP-induced hypoactivation[7]. Early-stage hyperactivity has been suggested to be caused by Aβ-induced activation of excitatory neurons and deactivation of inhibitory neurons—shifting the excitatory-inhibitory (EI) balance towards excitation. This claim is supported by studies showing overexpression of voltage-gated sodium channels in excitatory neurons [100] and underexpression of voltage-gated sodium channels in inhibitory neurons [101] in mice models.

On the other hand, tau stabilizes axonal microtubules—proteins crucial to axon structure—in healthy cells [102]. However, in AD, hyperphosphorylated tau proteins unbind microtubules and aggregate into soluble oligomers and insoluble, larger fibrils [11, 102]. Hyperphosphorylated tau is redistributed to the neuron cell body and dendrites [102, 103]. It has been shown that neurotoxicity is mainly mediated by soluble τP oligomers, as opposed to insoluble τP fibrils [97, 104, 105]. Several mechanisms for τP-mediated neurotoxicity have been corroborated, such as the relocation of axonal initial segments [106], dendrite impairment [107], and disruption of glutamate receptor trafficking [108]. Notably, hyperphosphorylated tau predominantly affects excitatory neurons [109]. Additionally, τP is known to cause axonal degradation [110].

Moreover, a recent study showed APP-overexpressing mice exhibiting hyperactivity, tau-overexpressing mice exhibiting hypoactivity, and tau/APP-overexpressing mice exhibiting hypoactivity [97]. In conclusion, the hypoactivity induced by τP appears to dominate Aβ-mediated hyperactivation [97, 111].

Moreover, several studies suggest that Aβ worsens τP pathology. Aβ can also raise tau concentrations in the cerebral spinal fluid [112] and promote hyperphosphorylation of tau [113]. The presence of amyloid plaques in the cortex also correlates with τP spreading [114, 115]. Cortical degradation and hypometabolism have been linked to synergistic effects between Aβ and hyperphosphorylated tau as well [116, 117].

In summary, Aβ induces hyperactivity by activating excitatory neurons and deactivating inhibitory neurons, whereas τP induces hypoactivation by impairing excitatory neurons. When both Aβ and τP are present, the effects of τP dominate,

---

[7] Hypoactivation refers to neuronal activity levels below normal activity levels.

causing hypoactivity. The precise mechanisms for these effects are multifactorial, though most proposed mechanisms point to disruptions in synaptic transmission and action potential propagation (see Figure 2.8).

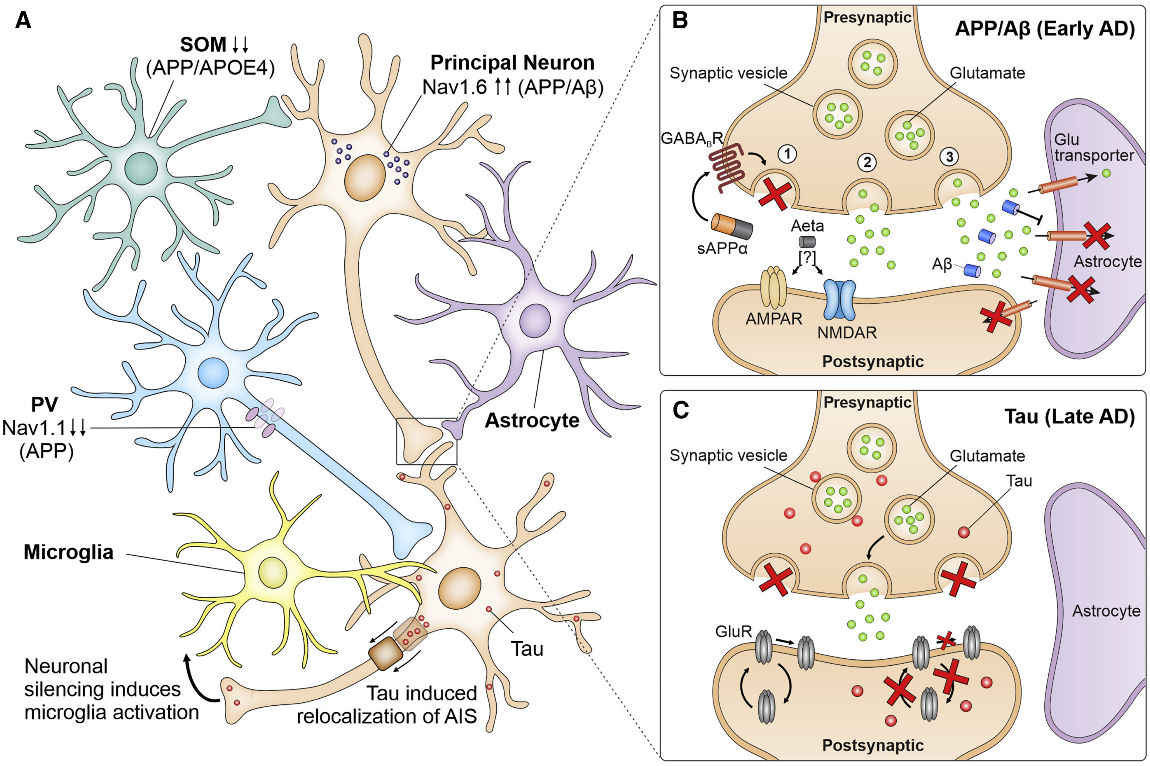

Figure 2.8: Summary of putative mechanisms for Aβ and τP pathology. *(A)* Increase in APP—and thus Aβ— leads to overexpression of Nav1.6 sodium channels in principal (excitatory) neurons and underexpression of Nav1.1 sodium channels in parvalbumin (inhibitory) neurons. τP induces relocalization of the axonal initial segment (AIS). *(B)* Aβ disrupts the reuptake of glutamate by astrocytes in the synaptic cleft. *(C)* τP disrupts neurotransmitter vesicle release and reduces postsynaptic glutamate receptor anchoring. Figure reprinted from Harris *et al.* [99].

2.9 Brain wave alterations in Alzheimer's disease

Brain waves have been studied extensively in the light of Alzheimer's disease. The detection of abnormal brain waves is expected to identify the onset of the disease earlier than current methods and offer insights into its detrimental symptoms. Furthermore, some clinics use E/MEG for diagnosing Alzheimer's disease [118]. As such, researchers are particularly interested in how brain waves differ between Alzheimer's patients and healthy subjects.

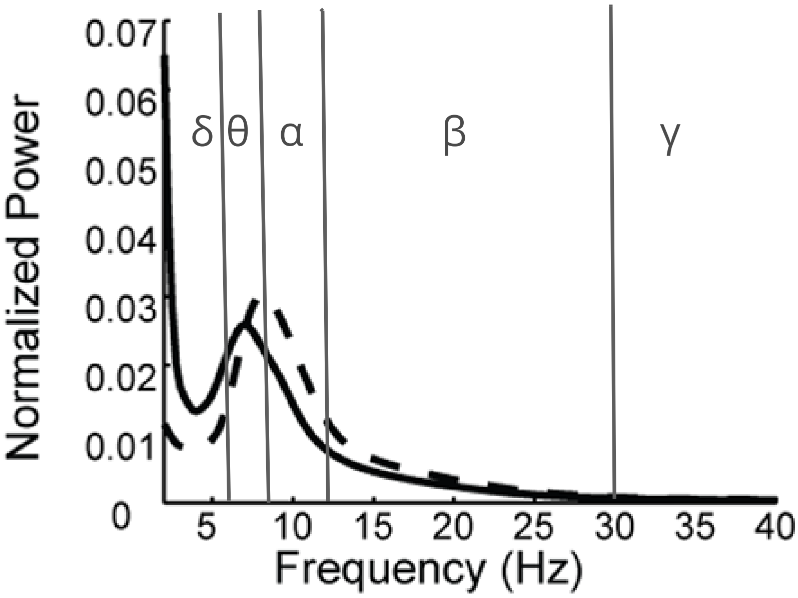

Figure 2.9: Comparison of EEG power spectra in the right inferior parietal area of AD (full line) and MCI (mild cognitive impairment, segmented line) patients. There is an increase (decrease) of power in the delta (alpha) range and frequency-slowing in the alpha range and above. Figure cropped and reprinted from Hsiao *et al.* [12].

In particular, researchers are looking for robust changes in the power spectra of brain waves and the amount of power distributed to each frequency band. Though E/MEG research on AD is riddled with contradictory and inconsistent results, a few characteristics of AD patients have been identified: (1) global frequency slowing [12–14], (2) power decrease in alpha frequences [12–14, 119–125], (3) increase in delta [12, 14, 119, 121] and theta power [13, 14, 119, 120, 122–124, 126] in certain brain regions, (4) decrease in gamma power [12, 119]. A representative spectrum from the literature is shown in Figure 2.9.

Gaubert *et al.* [119] found that early-stage AD patients have distinct EEG power-spectrum profiles compared to late-stage patients. Specifically, they found that delta power follows a U-shaped curve per Aβ concentration, whereas gamma and beta follow an inverted U-shaped curve. Moreover, momentary increases in alpha power have been observed for early-stage AD patients [119] and amnesic [127], Aβ-burdened healthy adults [128]. Aβ-induced hyperactivity could explain the differences in these power spectra profiles.

2.10 The neurobiology of brain cancer

Brain tumors originate either from other parts of the body, having spread (metastasized) into the central nervous system, or from the brain itself, in which case it is a *primary brain tumor*. The most common primary brain tumors are gliomas and meningiomas, and of these, gliomas are by far the most deadly. Like all cancers, glioma is caused by the excessive reproduction of genetically-mutated cells. In the case of glioma, the over-reproducing cells are glial cells, the non-neuronal cells in the brain that serve various supporting functions. As the glial tumors grow, they induce neuronal death in the surrounding tissue.

Gliomas are further classified into subtypes dependent on which glial type the tumors originate from [129]. A large variety of genetic mutations can lead to glioma. While the precise mechanisms of these mutations are not covered here, they typically affect enzymes participating in the cell reproduction cycle. Gliomas are also classified by their severity. Low-grade gliomas grow slowly and do not spread, whereas high-grade gliomas grow fast and spread quickly throughout neural tissue. Gliomas are, in general, incurable, as recurrence of tumors is frequent after surgical removal of tumors.

Glioma tumors interact with neurons and may cause significant changes in neural circuitry [130]. For example, as gliomas infiltrate healthy neural tissue, new connections between neurons may be formed to counteract the tumor damage. Gliomas can induce increases in cortical thickness and reorganize long-range axons between distant brain regions. Furthermore, neurons may form synapses with the mutated glial cells in the tumor. Excitatory neuronal cells may, as such, release glutamate into the cancer. Besides being an excitatory neurotransmitter, glutamate also induces cell growth, causing the tumor to grow faster. Additionally, the tumor cells excrete glutamate, which promotes cell growth of nearby tumor cells and increases neuronal activity [15, 16]. There is a positive feedback loop between neuronal activity and tumor growth; neuronal activity causes more tumor growth, and tumor growth causes more neuronal activity [130, 131].

2.11 Brain wave alterations in glioma

It is well established that glioma patients exhibit pathological differences in functional connectivity patterns across imaging modalities when compared to healthy controls [131, 133, 134]. In particular, overall functional connectivity is lower in the

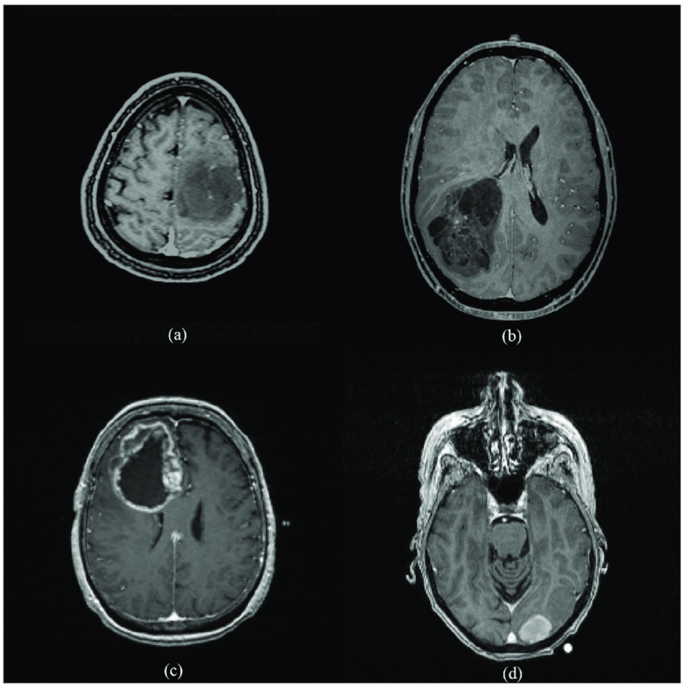

Figure 2.10: Examples of glioma tumors as captured by magnetic resonance imaging. *Upper row:* Low-grade gliomas. *Lower row:* High-grade glioblastomas. Figure taken from Hsieh *et al.* [132].

default-mode network as measured by fMRI [135–138]. Similarly, lower functional connectivity is observed in MEG for higher frequency bands (beta-gamma) [139–142], whereas lower frequency bands (delta-alpha) quite consistently display higher functional connectivity compared to controls [139, 142, 143]. Further differences in functional connectivity have been observed in network metrics of MEG functional connectivity such as clustering and path length [139, 143–145]. However, it remains unclear why and how such connectivity deviations occur in some patients, but not all [146].

Chapter 3

Mathematical modeling of neuronal activity and disease

To make quantitative predictions about brain diseases, it is useful to create mathematical models that combine neuronal activity models with disease progression models. In this chapter, we first introduce models of neuronal activity, starting with single-neuron dynamics, moving on to neuronal population dynamics, and finally building models of the entire brain. Then, we introduce disease progression models, focusing on reaction-diffusion processes across the brain. We will only consider models of neuronal dynamics and disease spreading on brain networks, skipping continuum-based approaches.

Later, in Chapter 4, we combine disease and neuronal activity modeling paradigms at the whole-brain scale to create a model of Alzheimer's disease. In particular, we focus on how toxic proteins impact neuronal activity dynamics, ignoring how neuronal activity may influence disease progression. We amend this in Chapter 5, where we formulate and analyze a mathematical model for how neuronal activity can affect disease spreading, this time on the single neuron scale. Nonetheless, we have yet to validate these models against clinical data. In Chapter 6, we fit a whole-brain model of neuronal activity to clinical data of brain cancer patients. All in all, the following chapters will draw extensively from the theory introduced in this chapter.

3.1 Mathematical modeling of neuronal activity

There is a wide range of mathematical models describing the activity of neurons. These models range in their spatial scale from the single neuron to the entire brain. Of particular interest are models of neuronal populations, which attempt to capture the average behavior of large networks of neurons. Some neuronal activity models are detailed and biophysical, whereas others may be purely phenomenological. We will briefly describe a small selection of single-neuron models and then move on to models of neuronal populations. We then use models of neuronal populations to build whole-brain models of neuronal activity. Sections 3.1.1–3.1.2 are largely based on Coombes & Wedgwood [147].

3.1.1 Single-neuron models

Single-neuron models vary significantly in their complexity. The Hodgkin-Huxley model [17], for example, is a highly detailed neuron model in which the neuron is imagined as an electrical circuit. In this metaphor, the cell membrane is a capacitor, the ion channels are voltage-varying resistors, and the electrochemical gradient is a battery. The Hodgkin-Huxley model provides an excellent experimental fit and was instrumental in building an understanding of action potentials. However, the Hodgkin-Huxley model is fairly high-dimensional and nonlinear. As such, numerical bifurcation analysis is the most viable option to study its dynamics. Furthermore, the high dimensionality makes the Hodgkin-Huxley model particularly undesirable when studying the dynamical properties of networks of neurons. For these reasons, there has been great interest in phenomenological single-neuron models that are easier to analyze individually and in larger networks.

One class of phenomenological neuron models is the *integrate-and-fire* neurons. These are nonsmooth one-dimensional models based on the assertion that neurons have a constant threshold for action potential initiation. This constant (hard) threshold is contrary to the *soft* thresholds found in the Hodgkin-Huxley and Fitzhugh-Nagumo neurons. In soft-threshold models, the voltage alone does not decide whether an action potential is elicited, as the voltage threshold is state-dependent.

The assumption of a hard voltage threshold is biologically unrealistic but provides simplified neuronal models that are easier to handle. One of the most commonly used integrate-and-fire neurons is the quadratic integrate-and-fire model,

$$\frac{dv}{dt} = v^2 + I, \quad \text{where} \lim_{\epsilon \to 0} v(t+\epsilon) = v_{\mathrm{r}} \text{ for } v(t) = v_{\mathrm{tr}}, \tag{3.1}$$

where $I \in \mathbb{R}$ is the input to the neuron, $v_{\mathrm{r}} \in \mathbb{R}$ is the resting membrane potential, and $v_{\mathrm{tr}} \in \mathbb{R}$ is the voltage threshold. When the voltage v reaches the threshold v_{tr}, it is reset to v_{r}. For $I < 0$, there are two fixed points $v = \pm\sqrt{|I|}$. These collide at $I = 0$ in saddle-node bifurcation (see Fig. 3.1a), after which no fixed points exist. For $I > 0$, $v(t)$ approaches infinity in finite time. For $I > 0$, we have periodic solutions

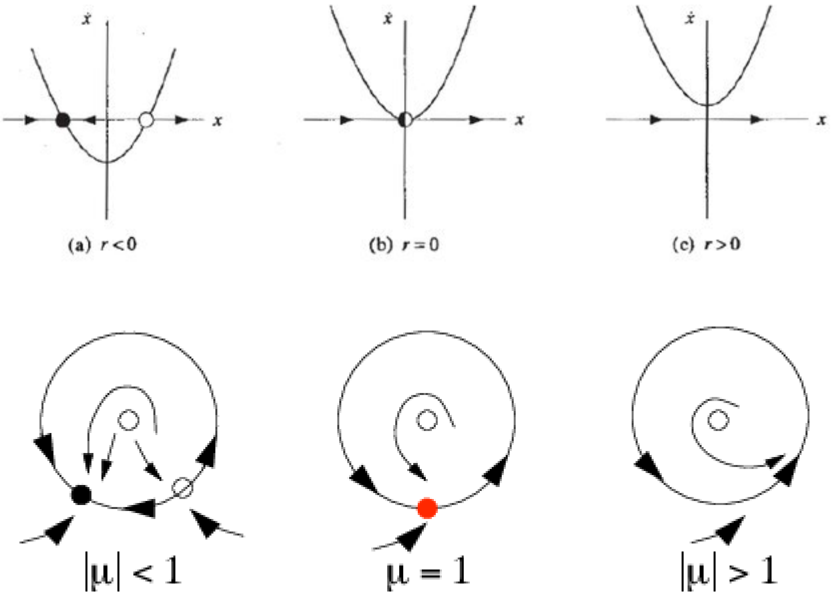

(a) $r<0$ (b) $r=0$ (c) $r>0$

$|\mu| < 1$ $\mu = 1$ $|\mu| > 1$

Figure 3.1: *Upper row:* An illustrative example of a saddle-node bifurcation. When varying the bifurcation parameter r, two fixed points (a stable node and a saddle node) collide and disappear. *Lower row:* An illustrative example of a saddle-node-on-invariant-circle (SNIC) bifurcation. Two fixed points (a stable node and a saddle node) exist on an invariant circle. These collide and disappear upon varying the bifurcation parameter μ.

(see Fig. 3.2a). The quadratic integrate-and-fire neuron can be solved analytically, and the period of the periodic solutions are $\pi/\sqrt{I}$ for $I > 0$.

When dealing with periodic behavior in dynamical systems, it is natural to think in terms of phases. Using the transformation $v = \tan(\theta/2)$ where $\theta \in \mathbb{S} := [0, 2\pi)$, the quadratic integrate-and-fire neuron can be transformed into the *theta neuron*

$$\frac{d\theta}{dt} = 1 - \cos\theta + (1 + \cos\theta)I, \tag{3.2}$$

where $I \in \mathbb{R}$ is the input, and we interpret a spike to occur when θ passes through π. For $I < 0$, there are two fixed points on the circle $\mathbb{S}$. These fixed points collide and disappear at $I = 0$ in a saddle-node-on-invariant-circle (SNIC) bifurcation (see Fig. 3.1b). For $I > 0$, the phase revolves around the circle.

Phase oscillators may be employed as phenomenological models of neuronal activity. Although not neuron models per se, a considerable amount of theory has been developed for networks of coupled phase oscillators, making them a popular choice for studying the synchrony properties of neurons. A generic phase oscillator evolves

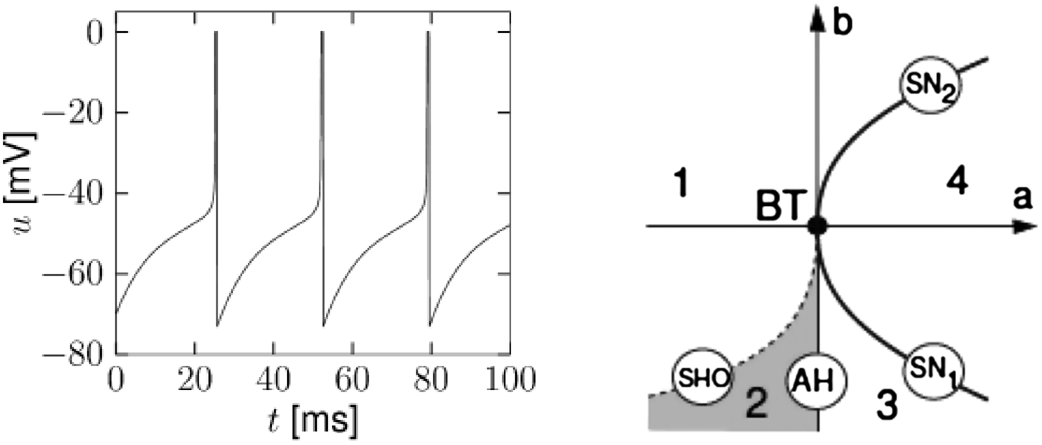

(a) (b)

Figure 3.2: *(a)* Simulation of a quadratic integrate-and-fire neuron (3.2) with $I > 0$. No fixed points exist, and v increases indefinitely before being reset to its threshold value v_{r} upon reaching v_{tr}, resulting in periodic firing. The figure is taken from Gerstner *et al.* [148]. *(b)* An overview of bifurcation found for the Wilcon-Cowan model (3.11)-(3.12) in terms of $a = c_1c_4$ and $b = c_2c_3$. SN–saddle-node bifurcation, AH–Andronov-Hopf bifurcation, BT–Bogdanov-Takens bifurcation, and SHO–saddle homoclinic-orbit bifurcation. The figure is taken from Cowan *et al.* [149].

according to

$$\frac{d\theta}{dt} = \omega + I, \tag{3.3}$$

where $\omega \in \mathbb{R}$ is the intrinsic frequency of the oscillator and $I \in \mathbb{R}$ is the input into the oscillator (neuron). Under assumptions of weak coupling, any network of oscillators with strongly attracting limit cycles can be approximated as a system of phase oscillators (see Ashwin *et al.* [150] for more on this topic in the context of neuroscience). For a network with adjacency matrix $\mathbf{W} = (W_{ij})$, the most common coupling is the Kuramoto coupling where $I = \sum_j W_{ij} \sin(\theta_j - \theta_i)$. Such sinusoidal coupling can be seen as a first-order approximation to a generic, periodic input function. In Chapter 5, we will use networks of phase oscillators as a model for neural networks. The instantaneous frequency $d\theta/dt$ is then interpreted as the neuron's firing rate, and we look deeper into the dynamics of a pair of phase oscillators connected with Kuramoto coupling.

We will now zoom out spatially and introduce some mathematical models of neuronal *populations*, which approximate the behavior of networks of connected neurons.

3.1.2 Neuronal population models

When studying populations of neurons, we may either (1) pick a single neuron model and connect them into a network or (2) formulate a mathematical model that describes the average behavior of a network of neurons. The first approach would be ideal but has some disadvantages. The dimensionality of such a dynamical system grows with the size of the neural network, which in realistic scenarios will include thousands, if not billions, of neurons. As such, the numerical simulations of these models will be challenging, and their fitting to experimental data will be difficult. The understanding of the dynamics that typically come from analytic and numerical approaches would also be out of reach.

As such, many researchers favor the second approach. Here, models for the average behavior of the network are formulated. In general, these *mean-field* models can be placed in two broad categories: neural fields and neural masses. Neural fields are formulated as partial differential equations and model each point in space as a neuron interacting with its surrounding neighbors through a connectivity kernel. Neural masses are instead formulated as ordinary differential equations, ignoring the spatial dimensions of neuronal populations and describing the average behavior of the neurons in the network. We will omit the discussion of neural fields and instead focus on neural masses. In Chapters 4 and 6, we will formulate models for brain-wide neuronal activity by coupling neural mass models together on a connectome (brain network). These *whole-brain* models of neuronal dynamics are discussed in more detail in Section 3.1.3. In Chapter 7, we will briefly discuss *next-generation neural masses* [151] in the context of future research directions. These are exact mean-field reductions of (infinitely) large networks of neurons, which are feasible for quadratic integrate-and-fire neurons and phase oscillators. However, for now, we will restrict ourselves to traditional neural mass models, which approximate the dynamics of neural populations.

One of the first formulations of a neural mass was the *Wilson-Cowan* model [152]. Although we do not make use of the Wilson-Cowan model in the upcoming chapters, it is the canonical neural mass model and is worth introducing briefly. The Wilson-Cowan model is often parameterized close to a Hopf bifurcation, and, therefore, we instead make use of the Hopf normal form as an approximation to neural mass dynamics, as discussed in after the following section.

3.1.2.1 Wilson-Cowan model

Consider a neural network in which we have both excitatory and inhibitory neurons. All neurons are connected to each other and are of an integrate-and-fire type with hard spiking thresholds sampled from some probability distribution.

The Wilson-Cowan model describes the evolution of the network activity by considering the proportion of cells firing. More precisely, let $E(t)$ be the proportion of the excitatory cells firing per unit time at time point t and let $I(t)$ represent the same quantity, but for the inhibitory cells. We call these quantities the *activity* of the excitatory and inhibitory subpopulations.

$E(t+\tau)$ will depend on the proportion of cells able to fire at time t and the proportion of cells receiving excitation at or beyond their threshold level at time t.

If a cell has fired, it cannot fire again for some refractory time period r, which is assumed to be the same for all neurons. Hence, the proportion of cells able to fire at time t is

$$q(t) = 1 - \int_{t-r}^{t} E(t)dt. \tag{3.4}$$

Remember that the neurons have hard firing thresholds sampled from some probability distribution $D(\theta)$. As the network is fully coupled, each neuron receives, on average, the same excitation input $x(t)$. Then the proportion of cells receiving input at or beyond their firing threshold is

$$f(x) = \int_{0}^{x(t)} D(\theta)d\theta. \tag{3.5}$$

Hence, f is the cumulative distribution of $D(\theta)$ and ranges from 0 to 1. Furthermore, f is sigmoidal if we assume that $D(\theta)$ is unimodal. This is the crucial characteristic of the Wilson-Cowan model: the proportion of active neurons depends sigmoidally on the population input.

We are still missing an essential ingredient: we need an expression for the average input of the network $x(t)$ in terms of the state variables E and I. Assuming that the effect of excitation decays according to function $\alpha(t)$, we have that

$$x(t) = \int_{-\infty}^{t} \alpha(t-t')\left[c_1 E(t') - c_2 I(t') + P(t')\right] dt' \tag{3.6}$$

where $c_1, c_2 > 0$ and $P(t)$ is an external input. We also implicitly assumed that each neuron sums up the input from all its neighbors linearly.

We can now write down a difference equation for $E(t)$ and analogously for $I(t)$ as

$$E(t+\tau) = \left(1 - \int_{t-r}^{t} E(t)\right) f\left(\int_{-\infty}^{t} \alpha(t-t')\left[c_1 E(t') - c_2 I(t') + P(t')\right] dt'\right), \quad (3.7)$$

$$I(t+\tau') = \left(1 - \int_{t-r}^{t} I(t)\right) f\left(\int_{-\infty}^{t} \alpha(t-t')\left[c_3 E(t') - c_4 I(t') + Q(t')\right] dt'\right), \quad (3.8)$$

where $c_3, c_4 > 0$, $Q(t)$ is the external input to the inhibitory subpopulation, and τ' may be different from τ. Next, we introduce the time-coarsening variable

$$\bar{E} = \frac{1}{r} \int_{t-r}^{t} E(t')dt', \quad (3.9)$$

with a similar time-coarsening variable $\bar{I}$. Assuming that $\alpha(t)$ is roughly constant for $0 \leq t \leq r$ and decays rapidly for $t \geq r$, we can estimate that

$$\int_{-\infty}^{t} \alpha(t-t')E(t')dt' = k\bar{E}, \quad (3.10)$$

for some constant k. Expanding the left-hand sides of (3.7)-(3.8) to first-order, we arrive at the Wilson-Cowan neural mass model:

$$\tau \frac{dE}{dt} = -E + (1 - rE) f\left(c_1 E - c_2 I + P(t)\right), \quad (3.11)$$

$$\tau' \frac{dI}{dt} = -I + (1 - rI) f\left(c_3 E - c_4 I + Q(t)\right), \quad (3.12)$$

where we have relabeled the state variables and constants for simplicity's sake. The time-coarsening is reasonable, as the refractory period r is typically 1ms and the membrane time constant τ is typically 21ms.

The dynamical repertoire of the Wilson-Cowan equations (3.11)-(3.12) has been studied extensively both analytically and numerically [149]. An overview of bifurcations in terms of $a = c_1 c_4$ and $b = c_2 c_3$ is shown in Figure 3.2b. In particular, the Wilson-Cowan model exhibits bistability, hysteresis, and periodic solutions. The latter is commonly interpreted as brain waves. Hence, neural networks of excitatory and inhibitory neurons provide a mechanistic explanation for the neural oscillations observed in EEG and MEG. For this reason, the Wilcon-Cowan model has been used broadly to study neural oscillations and is, in these applications, parameterized near a Hopf bifurcation (see region 2 and 3 in Figure 3.2b).

3.1.2.2 Hopf normal form as a neural mass model

As the Wilson-Cowan model is commonly parameterized close to a Hopf bifurcation, it is reasonable to use the Hopf normal form when studying brain wave dynamics.

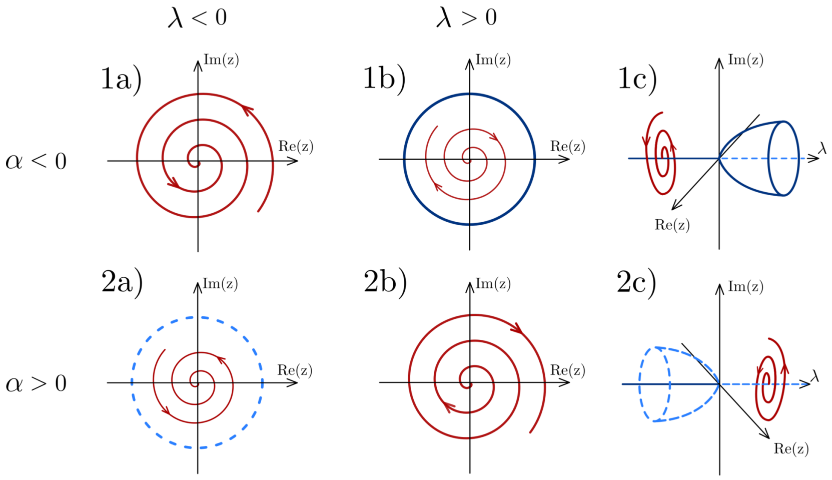

Figure 3.3: Supercritical and subcritical hopf bifurcations. *Upper row:* A supercritical Hopf bifurcation occurs for negative first Lyupanov coefficient $\alpha < 0$. The origin is stable for $\lambda < 0$ and unstable for $\lambda > 0$. A stable limit cycle exists for $\lambda > 0$ with radius $\sqrt{\lambda}$. *Lower Row:* A subcritical Hopf bifurcation occurs for positive first Lyupanov coefficient $\alpha > 0$. The origin is stable for $\lambda < 0$ and unstable for $\lambda > 0$. An unstable limit cycle exists for $\lambda < 0$ with radius $\sqrt{-\lambda}$.

Any sufficiently smooth dynamical system undergoing a Hopf bifurcation is locally topologically equivalent to the Hopf normal form [153],

$$\frac{dz}{dt} = z\left(\lambda + \omega i + (\alpha + i\beta)|z^2|\right), \tag{3.13}$$

where $i = \sqrt{-1}$, $z \in \mathbb{C}$, and $\lambda, \omega, \alpha, \beta \in \mathbb{R}$. The system (3.13) undergoes a Hopf bifurcation at $\lambda = 0$, which is supercritical for $\alpha < 0$ and subcritical for $\alpha > 0$. We will be focusing on supercritical Hopf bifurcations, in which a fixed point loses stability for $\lambda \geq 0$ giving rise to a stable limit cycle with radius $\sqrt{\lambda}$ and frequency ω (see Fig. 3.3).

In Chapter 4, we use a modified description of the Hopf normal form to study the progression of Alzheimer's disease. Meanwhile, in Chapter 6, we fit Hopf normal form oscillators to clinical MEG data. In both of these applications, we couple the Hopf normal form on a connectome, creating a whole-brain model for neuronal dynamics, the topic of the next section.

3.1.3 Whole-brain models of neuronal activity

Neural mass models describe the dynamics of large populations of neurons. These models support periodic solutions reminiscent of the brain waves recorded using EEG and MEG. As such, these neural masses are often used as models for brain waves.

However, neuroscientists are primarily interested in the correlations of brain waves between different brain regions. As such, researchers couple neural masses together using connectomes, which are anatomical reconstructions of the brain. These networks of coupled neural masses are called *whole-brain models*, allowing the modeling of correlations in neural activity across the entire brain.

Using an anatomical reconstruction of the brain, we can—as explained in Section 2.3—construct a weighted adjacency matrix $\mathbf{W} \in \mathbb{R}^{N\times N}$ with entries W_{ij}. The entries of $\mathbf{W}$ represent the strength of axonal connections between brain regions. We then can formulate a generic whole-brain model as

$$\frac{dx_i}{dt} = \mathcal{F}(x_i) + \mathcal{G}(\boldsymbol{x};\mathbf{W}), \quad i = 1, \ldots, N, \tag{3.14}$$

where $\boldsymbol{x} = [x_1, \ldots, x_N]$ with x_i as a measure of activity in brain region i, $\mathcal{F}$ represents the local dynamics, and $\mathcal{G}$ represents the network interactions, which depend on the adjacency matrix $\mathbf{W}$. Bear in mind the above formulation is not a strict definition but is designed to give the reader an idea of what is typically meant by a whole-brain model.

There is a great deal of variety in whole-brain model formulations. Typically, the local dynamics is chosen from the repertoire of neural mass models (Wilson-Cowan, Jansen-Rit, Stuart-Landau) and are then connected via a coupling function (typically sigmoidal). An example of a Wilson-Cowan whole-brain model is

$$\frac{dE_i}{dt} = -E_i + (1 - rE_i)S\left(c_1E_i - c_2I_i + \sum_{j=1}^{N} W_{ij}E_j\right), \quad i = 1, \ldots, N \tag{3.15}$$

$$\frac{dI_i}{dt} = -I_i + (1 - rI_i)S\left(c_3E_i - c_4I_i\right), \quad i = 1, \ldots, N \tag{3.16}$$

where $S(x) = [1 + e^{-x}]^{-1}$. This example highlights a common assumption in whole-brain models: only excitatory neurons form long-range connections, and these are only made to other excitatory neurons. Whole-brain models may also include delays in transmission between regions [154]. As we will see in Chapter 4, these transmission delays can be tailored to each brain region pair if the average axonal length is provided.

Whole-brain models have been used to replicate resting-state functional connectivity measured by fMRI, EEG, and MEG [155–157]. Additionally, whole-brain models have been used to investigate brain diseases and neuropsychiatric disorders, such as epilepsy [158, 159], Alzheimer's disease [24, 40, 160, 161], schizophrenia [162–164], and glioma [165–168].

As mentioned, a whole-brain model is a network of coupled neural masses in which each neural mass produces a time series mimicking the oscillatory signals of a region measured by EEG, MEG, fMRI, etc. These simulated signals can then be used to compute simulated functional connectivity, which is then used to fit the model to experimental functional connectivity. Typically, the Pearson correlation between the elements of the simulated and empirical functional connectivity matrices is used as a goodness-of-fit function [155–157, 169]. This is exactly the procedure we use in Chapter 6 to fit a Hopf whole-brain model to MEG data, using the phase-lag index (see Section 2.4.3) as our correlation metric.

3.2 The modeling of neurodegenerative diseases

The pathological spreading of proteins is the defining feature of neurodegenerative diseases. Mathematical modeling of these spreading mechanisms can help us understand how these diseases propagate and how to treat them. In Chapters 4 and 5, we will couple models of neuronal activity with disease progression models to understand how these processes interact to shape disease trajectories.

In this section, we will describe the modeling of prion-like spreading. As discussed in Sections 2.6–2.7, many neurodegenerative diseases, such as Alzheimer's disease and Parkinson's disease, spread in the following manner: A protein has a healthy and toxic variant. The toxic variants can bind to healthy variants, turning them into toxic ones. Toxic proteins then spread from region to region, causing neuronal dysfunction.

Pathological protein spreading in many of these diseases has a curious property. The spreading occurs mostly along axons. This is because some toxic proteins spread from neuron to neuron via axonal connections, and diffusion in neural tissue is strongest along axons.

As such, two properties are central to protein propagation. Proteins spread (mostly) along axonal connections, and healthy proteins are converted into toxic proteins. Hence, there is a diffusion process and a reaction process. Protein propagation models may be formulated as spatially extended PDEs on the brain or as ODEs on brain networks; we will only use and describe the latter. The simplest models of protein propagation ignore reaction processes and are pure diffusion models.

3.2.1 Network diffusion models of protein propagation

Suppose a brain network with N regions is represented by the weighted adjacency matrix $\mathbf{W} \in \mathbb{R}^{N \times N}$. The entries of the adjacency matrix W_{ij} typically denote the number of axonal connections or some other measure of physical connectivity. Spreading processes on networks typically incorporate the Laplacian matrix, defined as

$$\mathbf{L} = \mathbf{D} - \mathbf{W} \tag{3.17}$$

where $\mathbf{D}$ is a diagonal matrix containing the weighted degrees $D_{ii} = \sum_j W_{ij}$ for $i = 1, \dots, N$.

Let $\boldsymbol{x}(t) = [x_1(t), \dots, x_N(t)]^T$ denote the state of the disease; for example, toxic protein concentration in each node. The network diffusion model [170] evolves by

$$\frac{d\boldsymbol{x}}{dt} = -\rho \mathbf{L} \boldsymbol{x}, \tag{3.18}$$

where $\rho > 0$ is the diffusion constant. Some researchers prefer the *row-normalized Laplacian* instead of the regular Laplacian in the equation above. The row-normalized Laplacian is given by $\mathbf{L}_\mathrm{r} = \mathbf{L}\mathbf{D}^{-1}$ where $D_{ii}^{-1} = (\sum_j W_{ij})^{-1}$. The links between nodes can then be interpreted as transition probabilities of a random-walker process.

However, if the state variables are to denote protein concentrations, the regular Laplacian should be used, as it will enforce conservation of mass, which the row-normalized Laplacian does not.

On biophysical grounds, the diffusion model is incomplete, as it does not account for the dynamics of local conversion of healthy into toxic protein. Subsequent research has shown that including the conversion process improves modeling predictions and that the conversion process is much more prominent than the diffusion process [171].

3.2.2 Reaction-diffusion models on networks

The conversion (reaction) process transforming healthy proteins into toxic proteins may be described in varying levels of detail. As described in Sections 2.6–2.7, toxic proteins form aggregates and may be aptly modeled by the Smoluchowski equations [172]. These equations model the evolution of the concentration of each aggregate size. The Smoluchowski model is, as such, infinite-dimensional and has a large number of parameters, leaving numerical simulations and data fitting difficult.

The heterodimer model describes a simplification of prion-like aggregations. The heterodimer model has two protein species: the healthy variant u and the toxic variant v. These species interact in the following chemical reaction

$$u + v \xrightarrow{k_2} 2v, \tag{3.19}$$

with rate constant $k_2 > 0$. That is, toxic proteins convert healthy into toxic proteins. Adding this reaction to the network diffusion model gives the heterodimer model

$$\frac{du_i}{dt} = -\rho \sum_{j=1}^{N} L_{ij} u_j + k_0 - k_1 u_i - k_2 u_i v_i, \tag{3.20}$$

$$\frac{dv_i}{dt} = -\rho \sum_{j=1}^{N} L_{ij} v_j - \tilde{k}_1 v_i + k_2 u_i v_i, \tag{3.21}$$

for $i = 1, \ldots, N$, where $k_0 \geq 0$ is the production rate of healthy protein and $k_1, \tilde{k}_1 \geq 0$ are degradation rates of healthy and toxic protein, respectively. The toxic protein variant does not have a production term, as these are not naturally produced by the cell. The heterodimer model can be reduced to the Fisher-Kolmogorov model by assuming $du/dt \approx 0$.

In the case of Alzheimer's disease, where there are two types of protein propagating throughout the brain, amyloid-β and tau, the heterodimer model has been extended to include several protein species by Thompson *et al.* [173] in the following way

$$\frac{du_i}{dt} = -\rho \sum_{j=1}^{N} L_{ij} u_j + k_0 - k_1 u_i - k_2 u_i v_i, \tag{3.22}$$

$$\frac{d\tilde{u}_i}{dt} = -\rho \sum_{j=1}^{N} L_{ij} \tilde{u}_j - \tilde{k}_1 \tilde{u}_i + k_2 u_i \tilde{u}_i, \tag{3.23}$$

$$\frac{dv_i}{dt} = -\rho \sum_{j=1}^{N} L_{ij} v_j + k_3 - k_4 v_i - (k_5 + k_6 \tilde{u}_i) v_i \tilde{v}_i, \tag{3.24}$$

$$\frac{d\tilde{v}_i}{dt} = -\rho \sum_{j=1}^{N} L_{ij} \tilde{v}_j - \tilde{k}_4 \tilde{v}_i + (k_5 + k_6 \tilde{u}_i) v_i \tilde{v}_i, \tag{3.25}$$

for $i = 1, \ldots, N$, where $u_i, \tilde{u}_i$ denote the concentration of healthy and toxic Aβ, and where $v_i, \tilde{v}_i$ denote the concentration of healthy and toxic tau. Moreover, $k_0, k_3 \geq 0$ are production rates, $k_1, k_4, \tilde{k}_1, \tilde{k}_4 \geq 0$ are degradation rates, $k_2, k_5 \geq 0$ are reaction rates, and $k_6 \geq 0$ is an interaction term between the species. As motivated by the clinical literature, the presence of Aβ accelerates τP pathology [174]. The Thompson heterodimer model has, in particular, two dynamical regimes that are interesting to neurodegenerative disease applications; the model can support both primary and secondary tauopathy. In primary tauopathy, τP propagation can occur with or without the presence of Aβ. In secondary tauopathy, τP will only propagate into regions already infected with Aβ. It is well-established that Alzheimer's disease is a secondary tauopathy [175].

In the next two chapters, we formulate models of neurodegenerative disease by coupling disease spreading models with neuronal activity models. More precisely, in Chapter 4, we investigate whether toxic protein spreading gives rise to changes in neuronal dynamics as observed in Alzheimer's patients. We do this by coupling the Thompson heterodimer model with a whole-brain model of Hopf oscillators, simulating the course of the disease across the entire brain. In Chapter 5, we investigate how neuronal activity can impact disease spreading, primarily by analyzing a two-node graph of phase oscillators on which a heterodimer spreading process takes place.

Chapter 4

A multiscale model of Alzheimer's disease

4.1 Overview

Alzheimer's disease is a neurodegenerative disease in which two toxic protein species spread throughout the brain: Aβ and τP. It is widely believed that these toxic proteins give rise to the decline in cognition seen in Alzheimer's patients. Moreover, clinicians observe abnormalities in neuronal activity as the disease progresses. Early-stage patients show hyperactivity, whereas late-stage patients show hypoactivity and slowing of brain wave frequencies. It is unknown whether the toxic proteins are the culprits causing these changes in neuronal activity. Although the toxicity of Aβ and τP is heavily contested, some research indicates that Aβ induces hyperactivity and that τP induces hypoactivity.

In this chapter, we formulate a model of Alzheimer's disease that couples protein spreading and neuronal activity. We build into our model the hypothesis that Aβ and τP cause hyper- and hypoactivity, respectively. Our multiscale model correctly predicts early-stage hyperactivity, late-stage hypoactivity, and frequency slowing. As such, the theoretical work presented in this chapter suggests that Aβ and τP are the causative agents of the abnormalities in neuronal activity observed in Alzheimer's disease.

As discussed in Section 2.7, toxic variants of Aβ and tau protein spread throughout the brain. This process is best described by a reaction-diffusion system, where healthy protein is transformed into toxic protein while spreading across the brain. As such, we will adopt Thompson's two-species heterodimer model (see Section 3.2.2) for Aβ and τP spreading [173]. As for neuronal activity, we will use a whole-brain model consisting of Hopf normal form oscillators (see Section 3.1.2.2) modified to our purposes. To connect these two processes, we must introduce a model for the damage done by toxic proteins. Finally, we combine the protein spreading, neural damage, and neuronal activity to form a multiscale model of Alzheimer's disease. Simulations confirm the model correctly exhibits early-stage hyperactivity, late-stage hypoactivity, and frequency slowing. Upon further inspection, we find that the frequency slowing is induced locally, independently of network effects. Phase-reduction methods of the modified Hopf normal form oscillator further reveal that it is τP that causes the frequency slowing. This chapter is based on the paper by Alexandersen *et al.* [24].

4.2 Formulating a mathematical model of Alzheimer's disease

Three biophysical processes need to be modeled to elucidate the role of neurodegeneration on neuronal dynamics. First, toxic proteins systematically invade the brain over a typical time scale of 30 years. Second, these proteins cause damage at the regional level and in the connections between regions. Third, the oscillatory brain activity becomes abnormal as the neurons and their connections deteriorate. Here, we simulate these coupled processes on a connectome, where each node is associated with a brain region. The dynamics can be summarized as follows:

1. Given an initial connectome $\{\mathcal{G}_0\}$, we simulate the spreading of toxic Aβ and τP and compute the damage done by the local concentration of toxic proteins to the connectome $\{\mathcal{G}_t \mid t \in [0, 30]\}$;
2. At given intervals in the sequence $T = \{0, \Delta T, 2\Delta T, \ldots\}$, we simulate large-scale brain dynamics using neural mass models on $\{\mathcal{G}_t \mid t \in T\}$ for small time intervals.

We now formulate models for these three distinct processes: Aβ and τP propagation, toxic Aβ and τP pathology, and oscillatory brain dynamics.

4.2.1 Aβ and τP propagation

We build on the heterodimer model for the prion-like spreading of Aβ and τP on a connectome $\mathcal{G}_t$ with N nodes [176]. Though the Thompson heterodimer system was introduced in Section 3.2.2, we cover it here once more for ease of reading. Initially, the undirected connected connectome $\mathcal{G}_0$ is characterized by its weighted adjacency

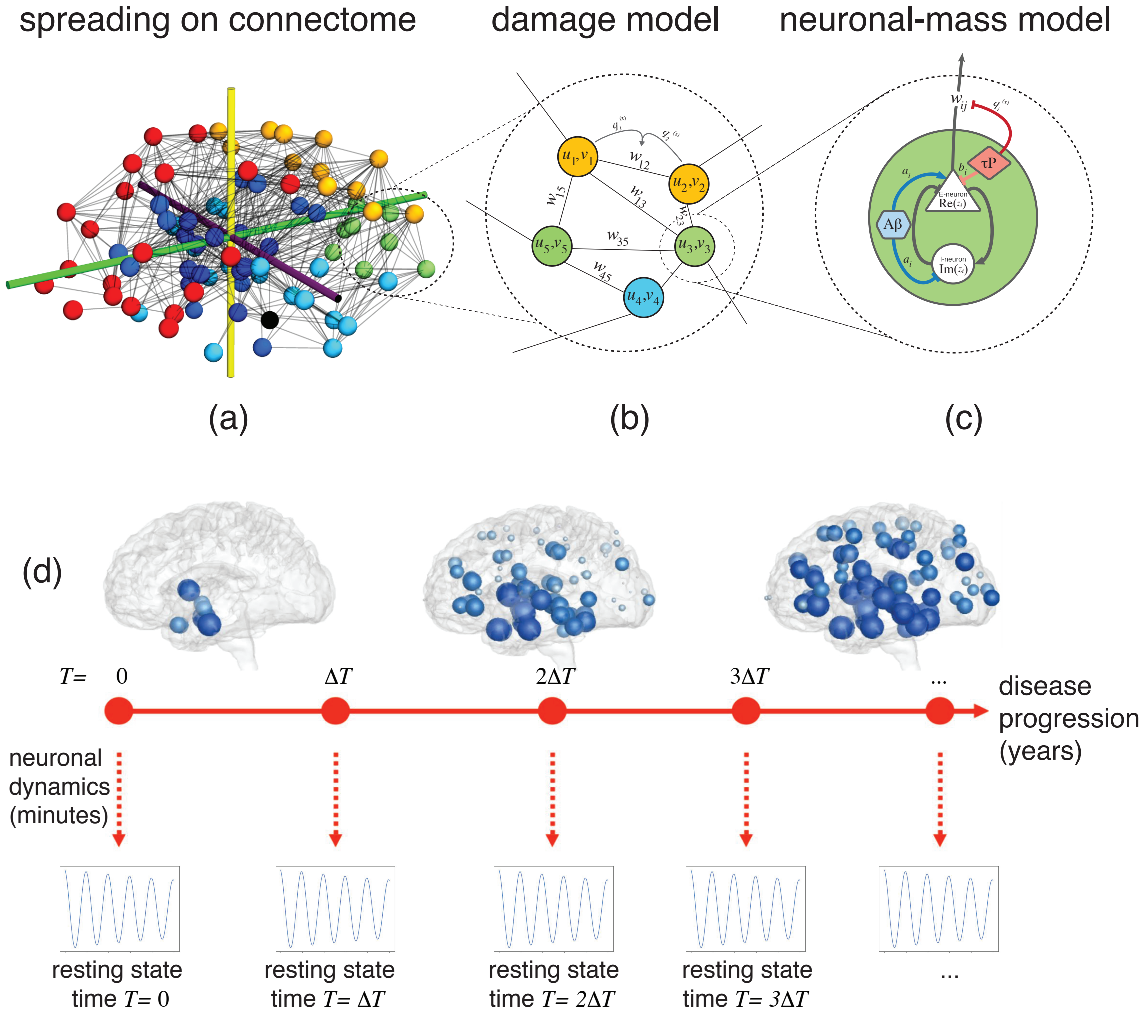

Figure 4.1: (a) Consider a connectome with N nodes representing brain regions and edges representing axonal connections. (b) On a given node i, we define the local concentrations u_i of toxic $A\beta$ and v_i of τP. An edge connects nodes i and j with weight $W_{ij}(t)$. (c) Each node consists of reciprocally connected subpopulations of excitatory and inhibitory neurons with their activity parameters a_i and b_i. Pathological Aβ disrupts the EI balance (increases a_i, decreases b_i), whereas toxic tau damage excitatory neurons (decreases a_i) and degrades axonal links (decreases W_{ij}). (d) The dynamics has two different time scales. First, we integrate the spreading and damage model over a period of 30 years. Then, every year, we probe the resting-state dynamics for < 1 minute using a neural mass model with fixed parameters given by the spreading model.

matrix $\mathbf{W}(0)$ with entries $W_{ij}(0) = n_{ij}/l_{ij}$ where n_{ij} is the mean number of axonal fibers connecting nodes i and j, and l_{ij} is the mean length of these fibers [177]. The spreading dynamics follows four species $u, \tilde{u}$ representing healthy/toxic Aβ and $v, \tilde{v}$ representing healthy/toxic τP [176]. The spreading dynamics at node i are governed by

$$\dot{u}_i = -\rho \sum_{j=1}^{N} L_{ij} u_j + k_0 - k_1 u_i - k_2 u_i \tilde{u}_i, \tag{4.1a}$$

$$\dot{\tilde{u}}_i = -\rho \sum_{j=1}^{N} L_{ij} \tilde{u}_j - \tilde{k}_1 \tilde{u}_i + k_2 u_i \tilde{u}_i, \tag{4.1b}$$

$$\dot{v}_i = -\rho \sum_{j=1}^{N} L_{ij} v_j + k_3 - k_4 v_i - (k_5 + k_6 \tilde{u}_i) v_i \tilde{v}_i, \tag{4.1c}$$

$$\dot{\tilde{v}}_i = -\rho \sum_{j=1}^{N} L_{ij} \tilde{v}_j - \tilde{k}_4 \tilde{v}_i + (k_5 + k_6 \tilde{u}_i) v_i \tilde{v}_i, \tag{4.1d}$$

for $i = 1, \ldots, N$. Here, $\rho > 0$ is a diffusion constant, the parameters $k_0, k_3 \geq 0$ are production rates, $k_1, \tilde{k}_1, k_4, \tilde{k}_4 \geq 0$ are clearance rates, $k_2, k_5 \geq 0$ denote transformations from healthy to pathological proteins, and $k_6 \geq 0$ describes a synergistic effect between toxic Aβ and toxic τP production. The latter synergistic effect induces a linear increase in τP production rate with respect to toxic Aβ, as motivated by observations of Aβ-facilitated τP progression [178–181]. The transport between different nodes is characterized by the graph Laplacian

$$L_{ij}(t) = -W_{ij}(t) + \delta_{ij} \sum_{j=1}^{N} W_{ij}(t), \tag{4.2}$$

where δ_{ij} is the Kronecker symbol. This model contains the conversion from healthy to toxic protein, the spreading of healthy and toxic protein, and the catalytic effect of τP on Aβ.

4.2.2 Toxic Aβ and tau pathology

In the next step, we proxy the neuronal damage caused by toxic proteins at each node and probe the effect of Aβ and τP separately. To this end, we introduce two damage variables $q_i^{(\beta)}, q_i^{(\tau)} \in [0, 1]$ at each node for each toxic protein; here 0 corresponds to no damage and 1 to maximum damage. The damage variables are assumed to follow first-order rate dynamics

$$\dot{q}_i^{(\beta)} = k_\beta \tilde{u}_i (1 - q_i^{(\beta)}), \tag{4.3a}$$

$$\dot{q}_i^{(\tau)} = k_\tau \tilde{v}_i (1 - q_i^{(\tau)}), \tag{4.3b}$$

for $i = 1, \ldots, N$. Here the parameters $k_\beta, k_\tau \geq 0$ denote the rates at which Aβ and τP cause neuronal damage, respectively.

Damage affects both the nodes and edges of the brain network. Whereas both Aβ and τP damage neurons, only τP affects long-range neural connections (the edges in the connectome). More specifically, if nodes i and j are initially connected, then the weight of their connection evolves according to

$$\dot{W}_{ij} = -\gamma (q_i^{(\tau)} + q_j^{(\tau)}), \tag{4.4}$$

where $\gamma \geq 0$. At the level of each individual node, Aβ and τP affect the excitatory and inhibitory populations differently. Let $a_i(t)$ and $b_i(t)$ denote the activity parameter of the excitatory and inhibitory population at node i, respectively. The pathology of Aβ and τP is modeled to follow the general trends that: (1) the presence of Aβ increases a_i and decreases b_i (Aβ-induced hyperactivity affecting both excitatory and inhibitory cells); (2) the presence of τP decreases a_i (τP-induced neurodegeneration of excitatory cells exclusively); (3) the presence of both Aβ and τP decreases a_i in the long-term (τP dominates Aβ effects). A minimal model that expresses these effects is given by

$$\dot{a}_i = \left[c_\beta q_i^{(\beta)} (a_{\max} - a_i) - c_\tau q_i^{(\tau)} \right] (a_i - a_{\min}), \tag{4.5a}$$

$$\dot{b}_i = -c_{\beta_2} q_i^{(\beta)} (b_i - b_{\min}), \tag{4.5b}$$

with rate constants $c_\beta, c_\tau, c_{\beta_2} \geq 0$ and parameters $a_{\max}, a_{\min}, b_{\min} > 0$. Here, a_i increases (decreases) when the damage ratio is tilted towards Aβ (τP) pathology, and b_i decreases with Aβ pathology.

Depending on the damage levels, there are typically two stationary points for a_i

$$a_1^* = a_{\min}, \tag{4.6}$$

$$a_2^* = a_{\max} - \frac{c_\tau q_\tau}{c_\beta q_\beta}, \quad \text{if } q_\beta \neq 0. \tag{4.7}$$

The stability of the two stationary points is interchanged at a transcritical bifurcation (shown schematically in Fig. 4.2) with respect to the ratio of τP to Aβ damage. Letting $R = q_\tau / q_\beta$, the transcritical bifurcation occurs when R crosses $R_{\text{crit}} = (a_{\max} -$

$a_{\min})c_\beta/c_\tau$. We have that a_1^* is stable for $R > R_{\text{crit}}$ and a_2^* is stable for $R < R_{\text{crit}}$. Note that with toxic Aβ and τP present, we have $\lim_{t\to\infty} R_{\text{crit}} = 1$. Therefore, we pick $R_{\text{crit}} \leq 1$ so that our model is commensurate with experimental findings that τP neuronal effects dominate Aβ effects in the long term [182]. By contrast, (4.5b) which determines the activity parameter b of the inhibitory population has only one stable stationary point $b^* = b_{\min}$ for $q_\beta > 0$.

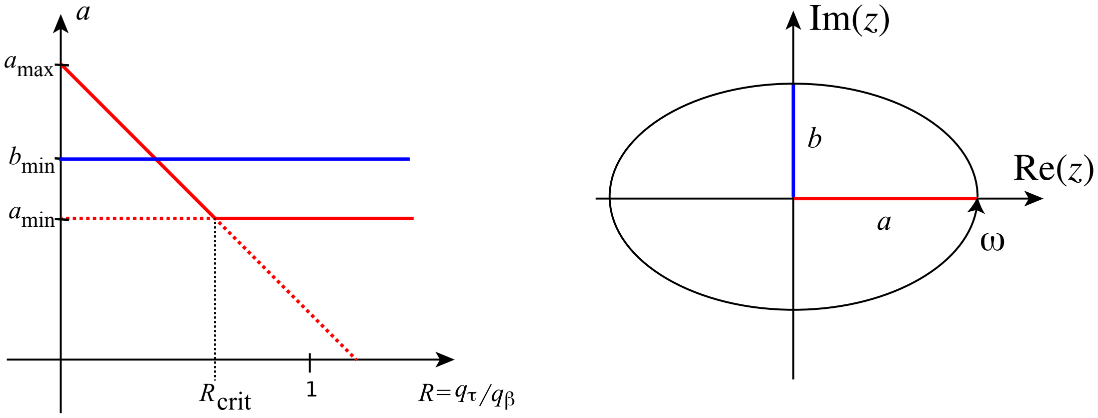

Figure 4.2: *Left:* An illustration of the transcritical bifurcation observed for the evolution of a (red lines). Bold (dashed) lines represent stable (unstable) fixed points, where we have included the unique stable fixed point of b (blue line). When the damage ratio is tilted towards Aβ-damage ($R < R_{\text{crit}}$), a_2^* is stable. In contrast, when the damage is tilted towards tau-damage ($R > R_{\text{crit}}$), a_1^* is stable. Note that in the simulations of the model presented herein, $a_{\min} = b_{\min}$ as opposed to the illustration. *Right:* The stable limit cycle of the (complex) variable $z = x + \mathrm{i}\, y$ in the minimal (without input, $\kappa = 0$) neural-mass model for $\lambda > 0$. The trajectory of the limit cycle follows an origin-centered ellipse with semiaxes (colored red and blue) of length, $|a|\sqrt{\lambda}$, $|b|\sqrt{\lambda}$, aligned with the real and imaginary axes. The trajectory travels with a constant angular frequency of ω with respect to the origin. In the case $\lambda < 0$, the solutions spiral towards the origin also with a constant angular frequency of ω.

Together, (4.1)–(4.5) form a system of nine ordinary differential equations that can be solved for given initial conditions. It describes the evolutions of the toxic protein concentration as well as the local and global damage. We integrate these equations over a period of 30 years and probe at regular intervals, every three years, the brain neuronal activity for given fixed parameters at that time $a_i(T), b_i(T)$, and $W_{ij}(T)$ by a neural mass model as shown in Fig. 4.1d.

4.2.3 Oscillatory brain dynamics

To assess the effect of degeneration on oscillatory brain dynamics, we employ a neural mass model on the evolving connectome. The neural mass introduced below is based on previous work [177] and approximates biophysical neural masses using a simplified Hopf normal form [183] (Section 3.1.2.2) subject to transmission delays [154]. For each node $i \in \{1, \dots, N\}$, let x_i denote the activity of the excitatory population and y_i the activity of the inhibitory populations at the node. Writing the state as a single complex variable $z_i = x_i + \mathrm{i}\, y_i$ (where $\mathrm{i} = \sqrt{-1}$), we consider the dynamics

$$\dot{z}_i = \mathcal{F}(z_i) + \kappa \tanh\left(\sum_{j=1}^{N} W_{ij} x_j(t - \tau_{ij})\right), \tag{4.8}$$

where

$$\mathcal{F}(z_i) = z_i\left(\lambda - \frac{x_i^2}{a_i^2} - \frac{y_i^2}{b_i^2}\right) - \omega_i y_i \left(\frac{a_i}{b_i}\right) + \mathrm{i}\, \omega_i x_i \left(\frac{b_i}{a_i}\right),$$

with Hopf bifurcation parameter $\lambda \in \mathbb{R}$, intrinsic frequency $\omega_i > 0$, coupling strength $\kappa \geq 0$, transmission delays $\tau_{ij} \geq 0$ between regions i and j, excitatory semiaxis $a_i > 0$, and inhibitory semiaxis $b_i > 0$.

The local dynamics—given by $\mathcal{F}$—above is a modified Hopf normal form, where the x_i- and y_i-axes have been scaled by parameters a_i and b_i respectively. As such, parameters a_i and b_i control the amplitudes of excitatory and inhibitory activity and are referred to as the excitatory and inhibitory semiaxes. These parameters are included to account for the dissimilar effects that AD progression exerts on excitatory and inhibitory neurons and will both change as the disease progresses throughout the connectome.

Scaling the variables of the Hopf normal form (4.8) changes the trajectory of the limit cycle in the complex plane from circular to elliptical. The origin-centered elliptical limit cycle arises from a Hopf bifurcation, having semiaxes with radii $a\sqrt{\lambda}$ and $b\sqrt{\lambda}$ aligned with the x-axis (activity of the excitatory population) and y-axis (activity level of the inhibitory population), respectively; cf. Figure 4.2. The Hopf bifurcation occurs at $\lambda = 0$, where the origin is a stable spiral for $\lambda < 0$, and the limit cycle becomes attracting for $\lambda > 0$. Importantly, the scaling of the variables does not change the intrinsic dynamical properties of the original simplified Hopf normal form. Hence, the inclusion of excitatory and inhibitory semiaxes does not affect the intrinsic frequency or the location of the Hopf bifurcation in parameter space respective to the original Hopf normal form. The effect these parameters have on the dynamics occurs through the sigmoidal coupling function.

The coupling between nodes is mediated by the excitatory subpopulations through the sigmoidal function tanh. As such, the response saturates for large amplitude input. The long-range communication thus only occurs between excitatory subpopulations. This is motivated by the fact that most long-range axons originate from and connect to excitatory neurons [34]. The coupling is subject to a time delay of τ_{ij} between nodes i and j. The neural mass dynamics are much faster than the disease evolution (seconds vs years), which justifies our assumption of taking the parameters constant over that time interval.

4.3 Aβ and τP are responsible for brain activity abnormalities in Alzheimer's disease

As we will see, simulating the Alzheimer's disease model introduced above demonstrates that Aβ and τP can cause the E/MEG symptoms observed in Alzheimer's patients. We find that early-stage hyperactivity, late-stage hypoactivity, and frequency slowing are all predicted by our model. Furthermore, axonal damage is unnecessary to produce these symptoms, and local τP damage alone is sufficient to produce frequency slowing.

4.3.1 Protein spreading and neural damage parameters

The brain network, or connectome, used in our simulations consists of 83 nodes with 579 links. It is constructed from tractography of diffusion tensor magnetic resonance images of 418 healthy subjects of the Budapest Reference Connectome v3.0 [184]. Table 4.1 summarizes the parameters chosen for the simulations. The parameters are composites of units in years and an arbitrary unit of concentration denoted by M. The parameters were chosen close to the exemplary set of parameters for secondary tauopathy as described by Thompson *et al.* [173]. The parameters k_β and k_τ are chosen so that the evolution of the Aβ and τP damage variables closely follow the evolution of toxic Aβ and τP concentrations. All nodes were initialized identically with respect to

Table 4.1: **Parameters for the spreading and network pathology simulations [173].**

$k_0 = 2$ M years^{-1}	$k_3 = 2$ M years^{-1}	$\gamma = 0.2$ cm years^{-1}
$k_1 = 2$ years^{-1}	$k_4 = 2$ years^{-1}	$c_\tau = 1.8$ years^{-1}
$k_2 = 2$ M^{-1} years^{-1}	$k_5 = 2$ M^{-1} years^{-1}	$c_\beta = 0.8$ years^{-1}
$\tilde{k}_1 = 1.5$ years^{-1}	$\tilde{k}_4 = 2.66$ years^{-1}	$c_{\beta_2} = 0.4$ years^{-1}
$\rho = 1 \cdot 10^{-3}$ cm years^{-1}	$k_6 = 12$ M^{-2} years^{-1}	$\delta = 0.95$ M
$k_\beta = 1$ M^{-1} years^{-1}	$k_\tau = 1$ M^{-1} years^{-1}	

healthy protein concentrations, local damage, and excitatory/inhibitory parameters as follows $u_i(0) = v_i(0) = 1$ M, $q_i^{(\beta)}(0) = q_i^{(\tau)}(0) = 0$ M, and $a_i(0) = b_i(0) = 1$. The initial amount of toxic Aβ in the entire connectome was 10^{-2} M and was distributed equally among the twelve amyloid-seeded nodes in both hemispheres: precuneus, isthmus cingulate, insula, medial orbitofrontal, and lateral orbitofrontal cortex. Likewise, the initial amount of τP was also 10^{-2} M distributed between the two tau-seeded nodes: left and right entorhinal cortex. The nonseeded nodes were initialized with zero toxic Aβ and τP. The maximum and minimum values of a_i and the minimum value of b_i were set as $a_{\max} = 1 + \delta$, $a_{\min} = 1 - \delta$, and $b_{\min} = 1 - \delta$.

4.3.2 Neuronal activity parameters

The neural mass parameters chosen for the simulations are summarized in Table 4.2. We have picked the Hopf bifurcation parameter λ close to the point of self-sustained oscillations so that the oscillations observed in the connectome simulations arise from the input between neighboring nodes. We compute the delay parameters using an average axonal speed v_{ax} gathered from the literature [185] by setting $\tau_{ij} = l_{ij}/v_{ax}$. The delay parameters are further discretized into 40 distinct values to ease computations of the system of delay differential equations. The intrinsic frequencies of the oscillators ω_i are drawn from a normal distribution with mean 10 Hz and standard deviation 1 Hz. Due to the stochasticity invoked by the randomly drawn frequencies, we repeat the neuronal dynamical simulations 10 times at each time point. The simulation plots below show averages and standard deviations over these trials. For each trial, every node variable z_i was initialized at a uniformly random point inside the complex unit circle. The global coupling strength κ was chosen so that sustained oscillations were seen for at least 20 seconds across all nodes in the initial connectome $\mathcal{G}_0$. To account for initial transient dynamics, the oscillatory dynamics were run for 20 seconds, of which the first 10 seconds were discarded. The remaining 10 seconds of the excitatory time series $x_i = \mathrm{Re}(z_i)$ are used in the spectral analysis with a sampling frequency of 500 Hz, resulting in a frequency resolution of 0.1 Hz. The power spectral density is computed for each node using the *periodogram* function from Scipy's signal processing module. The absolute alpha power is computed by integrating the power spectral density from 8 to 12 Hz. The peak frequencies were then taken to be the frequency between 8 and 12 Hz with the largest power spectral density.

Table 4.2: **Parameters for the neural mass simulations.**

$\lambda = -0.01$	$E(\omega) = 10$ Hz	$v_{ax} = 130$ cm/s
$\kappa = 5$	$\text{std}(\omega) = 1$ Hz	

4.3.3 Simulations predict early-stage hyperactivity and late-stage hypoactivity

To initialize the disease evolution, we seed toxic τP in the entorhinal cortex, which is widely accepted to be the first region affected by τP pathology [186]. Moreover, we seed toxic Aβ in the precuneus, isthmus cingulate, insula, medial orbitofrontal, and lateral orbitofrontal cortex, as has been suggested to be the first regions affected by Aβ pathology [187]. The spreading of Aβ and τP across different lobes of the connectome is shown in Fig. 4.3, in which we see a diffusive Aβ spreading followed at a later stage by pathological τP spreading from the entorhinal cortices progressively throughout the cortex. As the toxic proteins propagate through the brain, we simulate the damage done to the excitatory and inhibitory neuronal populations as well as the deterioration of axonal connections.

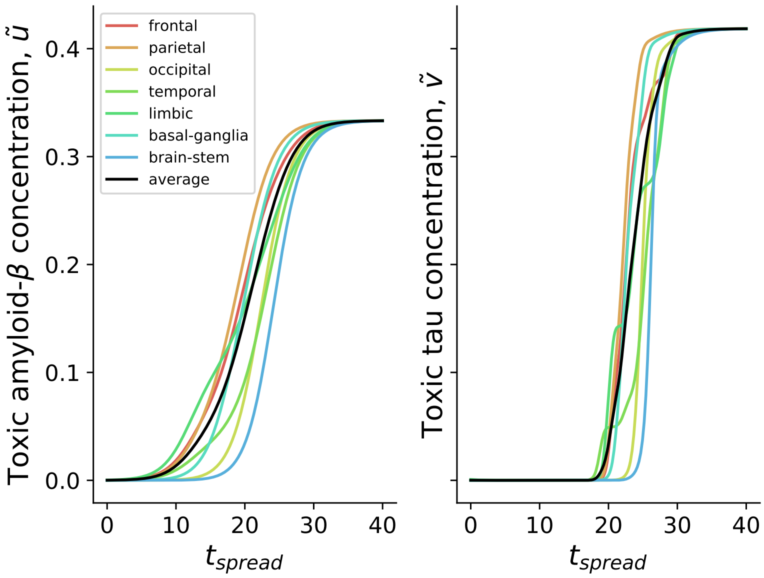

Figure 4.3: The evolution of toxic Aβ and τP concentrations against spreading time. The colored lines correspond to concentration averages over different brain lobes, whereas the black line is the global average.

Aβ and τP exhibit distinct pathological characteristics at the neuronal level. Crucially, Aβ and τP appear to discriminate between excitatory and inhibitory neurons;

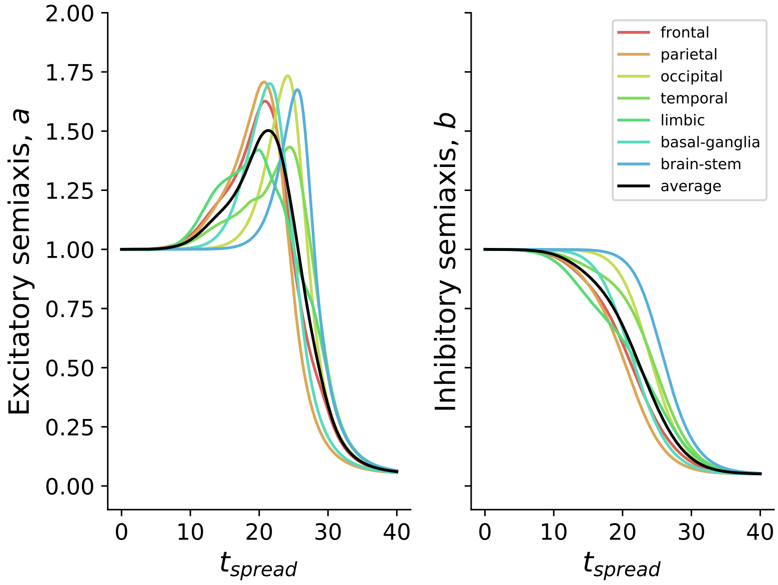

Figure 4.4: The evolution of neural mass activity parameters a_i, b_i. The colored lines correspond to averages of a_i and b_i over different brain lobes, and the black line is the global average over the entire brain network.

this is captured by our primary modeling assumptions that Aβ and τP assert distinctive pathological effects on excitatory and inhibitory nodes. Aβ upsets the EI balance (increasing excitation, decreasing inhibition), and τP damages axonal connections and excitatory neurons (see (4.5)).

Running simulations of Aβ and τP spreading across the connectome, we find that the excitatory strength parameter, across all brain regions, decreases after a period of initial hyperexcitability, as can be seen in Fig. 4.4. Additionally, inhibitory neuronal strength is reduced as excitatory strength peaks. Our simulations predict an initial early-stage EI imbalance favoring excitation followed by hypoactivation, a biphasic disease progression. However, it still remains to see how the disrupted neuronal parameters affect the large-scale neuronal dynamics themselves. To assess how the disease changes brain dynamics, we simulate neural oscillators on the decaying brain network and compute at regular intervals of $\Delta T = 3$ years. Specifically, we calculate the average spectral density across the alpha range (8–12 Hz) over a period of 10 seconds. The evolution of E/MEG alpha spectral density throughout disease progression is shown in Fig. 4.5. We observe a biphasic disease progression where a period of initial hyperactivity precedes hypoactivity. Regional differences can also be found. While all regions experience hyperactivity, the occipital lobe does so later than other lobes. There is a period in which the occipital lobe is hyperactivated, whereas other brain regions are hypoactivated. The parietal lobe exhibits particularly early hyperactivation, whereas the frontal lobe and limbic system are hypoactivated earlier than other brain regions.

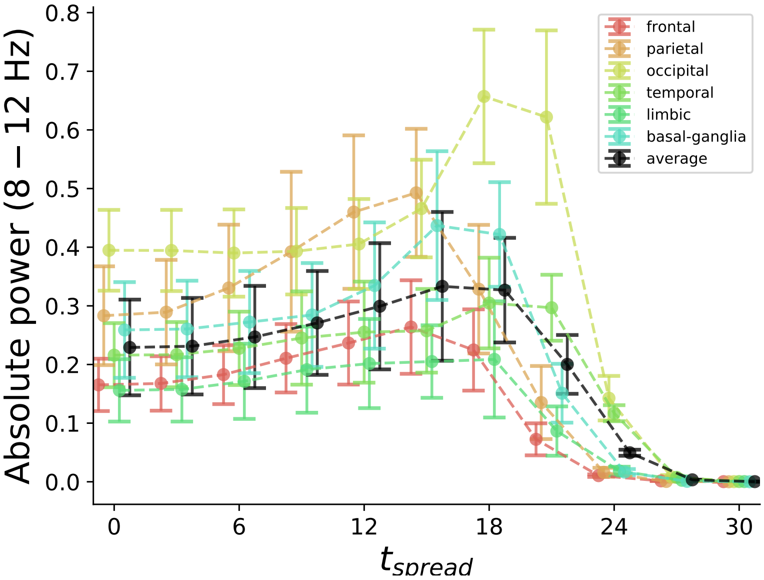

Figure 4.5: The average spectral density across the alpha range (8-12 Hz) throughout disease progression. The colored lines correspond to averages of the spectral density integral over different brain lobes, where the black line is the global average. The points and error bars are the mean and standard deviation over 10 realizations of normally distributed intrinsic frequencies.

4.3.4 Frequency-slowing is induced by local neurodegeneration

One of the most reproducible E/MEG characteristics in Alzheimer's disease is the slowing of the alpha brain wave. We now show that it is an emerging feature of our model and test whether it is due to local neurodegeneration, axonal degeneration, or both. To this end, we compute the peak frequency (the frequency at which the spectral power reaches its maximum in the 8–12 Hz range) throughout disease progression and vary the effect of axonal degradation induced by τP (achieved by changing parameter γ). The alpha peaks throughout disease progression are shown in Fig. 4.6 for three different values of the axonal degradation parameter. For axonal degradation ($\gamma = 0.2$), we observe a near-monotonic frequency increase, which can

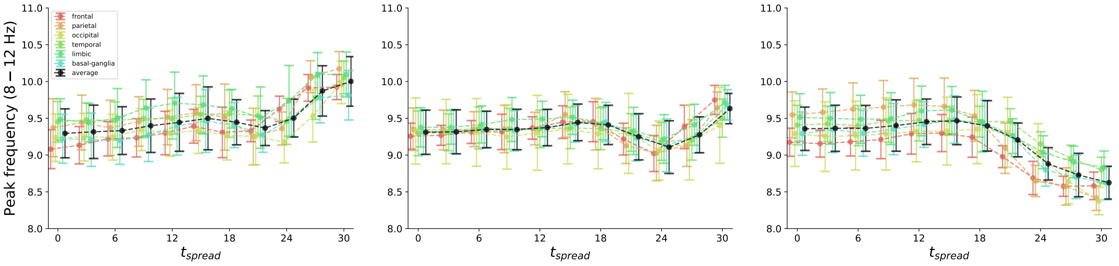

(a) $\gamma = 0.2$

(b) $\gamma = 0.1$

(c) $\gamma = 0$

Figure 4.6: The peak frequency in the alpha band $(8 - 12$ Hz) throughout spreading time for three different values of γ dictating the rate of axonal decay due to τP pathology. The colored lines correspond to averages of the peak frequency over different brain lobes, where the black line is the global average. The points and error bars are the mean and standard deviation over 10 realizations of normally distributed intrinsic frequencies.

be easily explained by the gradual decoupling of the neural mass oscillators. Further, oscillatory slowing is only apparent when the axonal degradation caused by τP is kept so low that its effect is negligible. We conclude that frequency slowing can be explained by local neurodegeneration alone rather than a change in connectivity. Overall, the different brain regions all follow the same trajectory. However, the parietal and frontal lobes show the most prominent oscillatory slowing. Unlike the frequency peaks, power density curves are mostly unaffected by axonal degradation during disease progression (not shown).

4.4 A mechanism for the alpha wave frequency slowing

The results of the previous section present an interesting phenomenon where frequency slowing is independent of changes in connectivity and is caused by a decrease in excitatory activity. As such, we examine a single self-coupled node with delay as a minimal system exhibiting key features of neural mass models. To understand the frequency-slowing effect, we use phase-reduction methods to approximate the dynamics of the minimal system under assumptions of weak coupling [188].

First, we find a phase description of the uncoupled, single neural mass. A phase description is a representation of the system's trajectory through a limit cycle by a variable $\theta \in \mathbb{S}$ with constant derivative. Second, we approximate the coupling as a function of θ by assuming the coupling is weak enough so that the coupled system does not deviate significantly from the uncoupled limit-cycle trajectory. Lastly, we use the phase-reduced system to approximate the period of oscillation.

In real vector notation, the state $X = (x, y)$ of a single, self-coupled neural mass evolves according to

$$\dot{X} = \mathcal{F}(X) + \kappa \mathbf{T}(cX(t-\tau)), \tag{4.9}$$

where $\mathcal{F}(X) = (\lambda x - \omega \frac{a}{b} y - x(\frac{x^2}{a^2} + \frac{y^2}{b^2}), \lambda y + \omega \frac{b}{a} x - y(\frac{x^2}{a^2} + \frac{y^2}{b^2}))$, $\mathbf{T}(X) = (\tanh x, 0)$, and $c > 0$. First, we want to find a phase description of the uncoupled system. Writing the self-coupled system (4.9) with $\kappa = 0$ in scaled polar coordinates ($x = ar\cos\phi, y = br\sin\phi$), we obtain

$$\begin{aligned} \dot{r} &= r(\lambda - r^2), && \text{(4.10a)} \\ \dot{\phi} &= \omega. && \text{(4.10b)} \end{aligned}$$

By construction, this system exhibits a Hopf bifurcation at $\lambda = 0$ with an attractive limit cycle for positive λ and an attractive spiral into the origin for nonpositive λ. Having scaled the x, y variables by a and b, the limit cycle description is now circular in the complex plane, even though our system has elliptical limit cycles in its original Cartesian coordinates. As we are interested in the oscillatory solutions of the system, we assume that λ is strictly positive. The choice of phase $\theta(t) = \phi(t)$ has a constant derivative and is thus a valid phase description for the uncoupled system. As $\theta(t) = \omega t$, the limit cycle trajectory is described by

$$X_0(\theta) = \begin{bmatrix} a\sqrt{\lambda}\cos\theta \\ b\sqrt{\lambda}\sin\theta \end{bmatrix}. \tag{4.11}$$

Now note that

$$\begin{aligned} \frac{\mathrm{d}}{\mathrm{d}t}\theta(t) = \frac{\mathrm{d}}{\mathrm{d}t}\theta(X(t)) &= \operatorname{grad}_X \theta(X)|_{X=X(t)} \cdot \frac{\mathrm{d}}{\mathrm{d}t}X(t) \\ &= \operatorname{grad}_X \theta(X)|_{X=X(t)} \cdot (\mathcal{F}(X(t)) + \kappa\mathbf{T}(cX(t-\tau))) \\ &= \omega + \kappa \operatorname{grad}_X \theta(X)|_{X=X(t)} \cdot \mathbf{T}(cX(t-\tau))), \end{aligned} \tag{4.12}$$

where grad denotes the gradient. To write down the phase reduction, we approximate $\operatorname{grad}_X \theta(X)|_{X=X(t)}$ above by the phase-sensitivity function

$$\begin{aligned} Z(\theta) &= \operatorname{grad}_X \theta(X)|_{X=X_0(\theta)} \\ &= \frac{1}{\sqrt{\lambda}} \begin{bmatrix} -\sin\theta/a \\ \cos\theta/b \end{bmatrix} \end{aligned} \tag{4.13}$$

and $\mathbf{T}(cX(t-\tau))$ by $\mathbf{T}(cX_0(\theta(t-\tau)))$. Hence, the approximate phase evolution of our self-coupled system is

$$\begin{aligned}\dot{\theta} &= \omega + \kappa Z(\theta) \cdot [\tanh(-ca\sqrt{\lambda}\cos\theta(t-\tau)), 0]^T \\ &= \omega + \kappa f(\theta(t), \theta(t-\tau)), \end{aligned} \tag{4.14}$$

where

$$f(\theta(t), \theta(t-\tau)) = -\frac{\sin\theta}{a\sqrt{\lambda}} \tanh(ca\sqrt{\lambda}\cos\theta(t-\tau)). \tag{4.15}$$

We may now use the phase-reduced system to obtain an approximate expression for the period of the system. More precisely, let $\theta(t)$ be a solution to an ODE with at least one stable limit cycle and assume that $\theta(0) = \theta_0$ is on a stable limit cycle. The *period* T *of* $\theta(t)$ is the smallest positive real number such that $\theta(T) - \theta(0) = 2\pi$. We will now derive an expression for T of the above phase-reduced system (4.14). Starting from the definition of the period, we have

$$\begin{aligned} 2\pi &= \theta(T) - \theta(0) \\ &= \int_0^T \dot{\theta}(t)\,\mathrm{d}t \\ &= T\omega + \kappa \int_0^T f(\theta(t), \theta(t-\tau))\,\mathrm{d}t. \end{aligned} \tag{4.16}$$

As κ is small, we may assume $\dot{\theta}(t) > 0$ for all t. This assumption implies that $\theta(t)$ is a one-to-one function on $0 \leq t < T$ and thereby allows us to use $\theta(t)$ to make an integral substitution above from t to θ. Hence,

$$\begin{aligned} T\omega + \kappa \int_0^T f(\theta(t), \theta(t-\tau))\,\mathrm{d}t &= T\omega + \kappa \int_{\theta(0)}^{\theta(T)} f(\theta(t), \theta(t-\tau)) \frac{1}{\mathrm{d}\theta/\mathrm{d}t}\,\mathrm{d}\theta \\ &= T\omega + \kappa \int_{\theta_0}^{2\pi+\theta_0} \frac{f(\theta(t), \theta(t-\tau))}{\omega + \kappa f(\theta(t), \theta(t-\tau))}\,\mathrm{d}\theta. \end{aligned} \tag{4.17}$$

Rearranging in terms of T and approximating the delayed phase as if it was free-running, $\theta(t-\tau) \approx \theta(t) - \omega\tau$, we obtain

$$T \approx \frac{1}{\omega}\left(2\pi - \kappa \int_{\theta_0}^{2\pi+\theta_0} \frac{f(\theta, \theta-\omega\tau)}{\omega + \kappa f(\theta, \theta-\omega\tau)} d\theta\right). \tag{4.18}$$

Although we are not able to solve the integral in the above expression analytically, we may solve the integral resulting from a fourth-order Taylor expansion of the integrand around $c = 0$. Inserting the result of the integral into the above equation leaves us with

$$T \approx \frac{2\pi}{\omega} - \frac{\pi c\left(a^2c^2\lambda - 4\right)\sin(\tau\omega)}{4\omega^2}\kappa \\ + \frac{\pi c^2\left(\left(2a^2c^2\lambda - 3\right)\cos(2\tau\omega) - 3a^2c^2\lambda + 6\right)}{12\omega^3}\kappa^2 + O\left(\kappa^3, c^5\right). \tag{4.19}$$

Further, assuming τ is small (which is biologically reasonable as axonal communication is fast) gives us

$$T \approx \frac{2\pi}{\omega} + \tau\frac{c\pi\kappa(4 + \frac{3}{2}\omega^2c^2\kappa^2 - a^2c^2\lambda)}{4\omega} + \frac{c^2\pi\kappa^2(3 - a^2c^2\lambda)}{12\omega^3} + \mathcal{O}(\kappa^3, c^5, \tau^2), \tag{4.20}$$

where we see that decreases in the excitatory activity parameter a and increases in coupling strength κ cause frequency slowing. Crucially, the decrease in excitatory activity by a is sufficient to cause frequency slowing even in a nondelayed, isolated self-coupled node. Hence, local neurodegeneration alone can explain oscillatory slowing. Finally, rearranging (4.19) we obtain

$$T \approx \frac{2\pi}{\omega} + \frac{c\pi\sin\omega\tau}{4\omega^2}\kappa + \mathcal{O}(\kappa^2, c^2). \tag{4.21}$$

Hence, the product of the intrinsic frequency and the delay decides the magnitude and sign of the initial slope of the period T against coupling strength κ. The effect of the delay on the period is shown in Fig. 4.7 with a comparison of the original system, the phase-reduced system, and the frequency approximation, showing good agreement. From (4.21), it is clear that there are parameter regimes where we have frequency slowing or acceleration, as shown in Fig. 4.7.

We conclude that the role of excitatory activity and coupling strength on oscillator frequency depends on both the delay and the intrinsic frequency of the oscillator. This phenomenon can only be captured by introducing delay into the system.

4.5 Conclusion

By accounting for the disparate spreading patterns and differential pathology of Aβ and τP, we have developed a modeling approach that captures the main characteristics of AD-related brain rhythm alterations. Our approach links the spreading of pathological proteins, their neurotoxic effects, and the temporal evolution of neural dynamics. In doing so, we observe early-stage hyperactivation followed by a decrease and slowing of the dominant alpha rhythm. Moreover, we find that the oscillatory

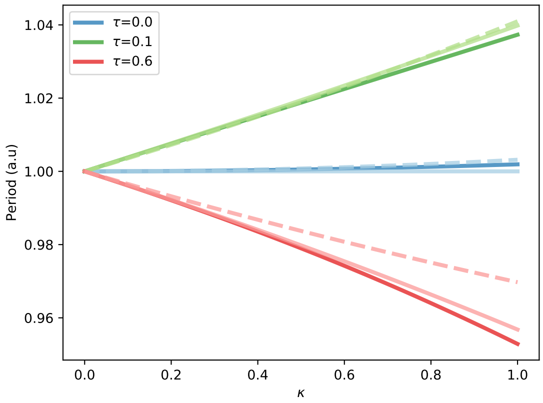

Figure 4.7: The dependency between period and coupling strength for the self-coupled neural mass model (solid, bold line), its phase-reduced counterpart (solid, light line), and the analytical approximation of the frequency (dashed line). Different colors correspond to different values of the delay τ. Other parameters are set as $\omega = 1$, $a = 1, b = 1, c = 1$, and $\lambda = 1$.

slowing is induced by local neurodegeneration and is independent of damage to interregional connectivity.

The modeling assumption that protein spreading occurs primarily through structural connectivity is reasonable for τP but less so for Aβ. The more diffusive nature of Aβ spreading, compared to the prion-like spreading of τP, is imposed in our simulations by initializing toxic Aβ in multiple cortical regions. In future studies, reworkings of spreading mechanisms and parametrizations can be implemented to differentiate further the spreading patterns of Aβ and τP.

In the simulated E/MEG power spectrum, we observe decreases in alpha power following an initial increase in power. It is presently challenging to make comparisons with clinical data, as early-stage hyperactivation in human AD and its effect on E/MEG spectra are yet to be fully explored. Recent studies, however, have found increases in alpha power in healthy Aβ-burdened and amnesic older adults, specifically in the parietal region [127, 128], the region which our simulations predict to show the greatest early alpha power increase.

While the simplicity of our neural mass model allows for mathematical analysis and a clear interpretation of simulation results, its phenomenological approach has some limitations. In our approach, the intrinsic frequency of each node across the connectome is fixed in the alpha band throughout the brain. As a phenomenological model, the parameters have limited direct biological interpretation. Thus, in contrast to previous mesoscale computational studies [189], our model lacks a detailed mechanism for the generation of the dominant resting-state alpha rhythm. Moreover, some spatial differentiation of intrinsic frequency may be more realistic, such as limiting the generation of alpha-band oscillations to the posterior part of the brain, where they are more typically observed in resting-state E/MEG. Another important consideration is cross-frequency coupling, which has lately been studied in smaller network motifs [190–192] though largely ignored in large-scale connectome models. There is no standard way to incorporate multi-frequency dynamics into brain-wide oscillator networks. One approach is to consider networks of neural masses with multiple dynamical regimes operating at different frequencies [193]. Such a multi-frequency approach would facilitate the validation against experimental data, as clinical studies primarily report relative, not absolute, spectral power changes.

Herein, we have demonstrated that a simple computational approach, testing a recently proposed hypothesis for Aβ and τP pathology [194], reproduces hallmark features of AD neuronal dynamics. The spreading patterns and presumed cellular pathology produce a biphasic disease progression, where neuronal hyperactivity is observed before oscillatory slowing and hypoactivity. Furthermore, thanks to the simplicity of our neural mass model, we are able to show that decreases in excitatory neuronal activity induce oscillatory slowing independently of structural changes due to axonal damage. Conclusively, our study suggests that the disparate spreading patterns and neuronal pathology of Aβ and τP, together with their distinctive effects on excitatory and inhibitory neurons, may constitute important facets of Alzheimer's disease and should not be ignored in the computational modeling of the disease.

In this chapter, we implicitly assumed that neuronal activity has no impact on the disease progression. Interestingly, recent evidence has surfaced that neuronal activity can influence protein spreading [63–65]. This is not only the case for Alzheimer's disease but also for other tauopathies and synucleinopathies, such as Parkinson's disease. This relationship between neuronal activity and spreading is yet to be investigated mathematically and may have massive implications for our understanding of neurodegenerative diseases.

Chapter 5

Neuronal activity induces symmetry breaking in neurodegenerative disease

5.1 Overview

Neurodegenerative diseases are characterized by the spreading of toxic proteins across the brain. Certain classes of neurodegenerative disease—namely tauopathies and synucleinopathies—spread from neuron to neuron via synapses. Recent research has shown that higher neuronal activity increases protein transfer between synapses. In particular, studies suggest that neurons with higher firing rates transfer protein to their neighboring neurons at a faster rate [63, 65–67, 195]. As such, neuronal activity may affect the spreading patterns in diseases such as Alzheimer's and Parkinson's.

It is then natural to consider neuronal activity and protein spreading as interacting dynamical processes occurring on the same neuronal network. As noted in the previous chapter, these two processes occur on vastly different timescales: neuronal activity operates on the timescale of seconds, whereas protein spreading occurs on the timescale of years. In contrast to the previous chapter, it is now more natural to consider networks of neurons rather than brain regions. We are still modeling the spread of proteins by the heterodimer model, though we will now use phase oscillators as a phenomenological model for single neurons.

In this chapter, we study the multiple-timescale dynamics of a heterodimer spreading process on a network of phase oscillators. In our model, higher frequencies induce higher protein transport rates, whereas higher concentrations of protein decrease oscillator frequencies. Using a minimal two-node model, we establish that heterogeneous oscillatory activity facilitates toxic outbreaks and induces symmetry breaking in the spreading patterns. We then extend the model formulation to larger networks and perform numerical simulations of the slow-fast dynamics on common network motifs and the brain connectome. The simulations corroborate the findings from the minimal model, underscoring the significance of multiple-timescale dynamics in modeling neurodegenerative diseases.

This chapter is organized as follows: First, we consider the heterodimer model on a minimal network of two nodes with asymmetric link weights, reflecting the effect of fixed activity on the spreading dynamics. Second, we consider a multiple timescale two-node system, now equipped with both heterodimer and neuronal dynamics, which we call the *heterodimer-oscillator* model. Third, we support the findings from the minimal heterodimer-oscillator system by performing numerical simulations on common motifs found in complex networks and by investigating the effect neuronal activity can have on tau spreading in the human brain during Alzheimer's disease. This chapter is based on the preprint by Alexandersen *et al.* [25].

5.2 Heterodimer dynamics

In this section, we build on the classical heterodimer model for a simple 2-node graph and introduce asymmetry in the coupling between the nodes to understand its impact on the system dynamics. Specifically, we identify a pair of fixed points exchanging stability at a transcritical bifurcation and observe that the asymmetrical coupling not only shifts the location of this bifurcation in parameter space but also disrupts symmetries between the fixed points. The dynamical behavior of the asymmetrically-coupled heterodimer model will be instrumental in our analysis of the full system with coevolutionary spreading and oscillator dynamics performed in Section 5.3.

5.2.1 The heterodimer model

The heterodimer model describes a process of healthy proteins being converted into toxic proteins by a second-order rate equation. As in previous chapters, we assume that the process takes place on a network with N nodes defined by a weighted adjacency matrix $\mathbf{W} = (W_{ij})$. For $\mathbf{W}$ we define the standard graph Laplacian $\mathbf{L} = (L_{ij})$ with components

$$L_{ij} = -W_{ij} + \delta_{ij} \sum_{j=1}^{N} W_{ij}, \tag{5.1}$$

where δ_{ij} is the Kronecker symbol. According to the heterodimer model, the evolution of the concentration of healthy proteins $u_i \geq 0$ and of toxic proteins $v_i \geq 0$ at node i

is given by

$$\dot{u}_i = -\sum_{j=1}^{N} L_{ij} u_j + k_0 - k_1 u_i - k_2 u_i v_i, \tag{5.2a}$$

$$\dot{v}_i = -\sum_{j=1}^{N} L_{ij} v_j - k_3 v_i + k_2 u_i v_i, \tag{5.2b}$$

for $i = 1, \ldots, N$ where $k_0 > 0$ is the healthy protein production rate, $k_1 > 0$ and $k_3 > 0$ are the healthy and toxic clearance (protein degradation) rates, and $k_2 > 0$ is the rate of conversion from healthy to toxic proteins.

With the ultimate goal of understanding how the possible dynamics of this system are affected by oscillatory activity, we start with the simple case of two nodes connected by an undirected link as shown in Figure 5.1a:

$$\dot{u}_1 = -\ell u_1 + \ell u_2 + k_0 - k_1 u_1 - k_2 u_1 v_1, \tag{5.3a}$$

$$\dot{v}_1 = -\ell v_1 + \ell v_2 - k_3 v_1 + k_2 u_1 v_1, \tag{5.3b}$$

$$\dot{u}_2 = \ell u_1 - \ell u_2 + k_0 - k_1 u_2 - k_2 u_2 v_2, \tag{5.3c}$$

$$\dot{v}_2 = \ell v_1 - \ell v_2 - k_3 v_2 + k_2 u_2 v_2, \tag{5.3d}$$

where $\ell > 0$ is the single, reciprocal weight link. Note that all parameters and variables are nonnegative. The system has two fixed points. In general, we refer to a fixed point as *healthy* if $v_i = 0$ for all $i = 1, \ldots, N$ and *toxic* if $v_i > 0$ for at least one $i \in \{1, \ldots, N\}$. The 2-node heterodimer model has exactly one healthy fixed point (denoted by a superscript H) and one toxic fixed point (superscript T), given by

$$u_1^{\mathrm{H}} = u_2^{\mathrm{H}} = \frac{k_0}{k_1}, \quad v_1^{\mathrm{H}} = v_2^{\mathrm{H}} = 0, \tag{5.4a}$$

$$u_1^{\mathrm{T}} = u_2^{\mathrm{T}} = \frac{k_3}{k_2}, \quad v_1^{\mathrm{T}} = v_2^{\mathrm{T}} = \frac{\kappa}{k_2 k_3}, \tag{5.4b}$$

where $\kappa = k_0 k_2 - k_1 k_3$.

Regarding the dynamics, we are mostly interested in the transition between healthy and toxic states. In other words, we are interested in bifurcations where a healthy equilibrium loses stability and a toxic equilibrium becomes stable. For (5.3), a direct computation of the linearized system around the healthy equilibrium indicates that healthy and toxic equilibria exchange stability through a transcritical bifurcation occurring at $\kappa = 0$. Indeed, the stability of the healthy state is governed by a single eigenvalue

$$\lambda^{\mathrm{H}} = \frac{\kappa}{k_1}, \tag{5.5}$$

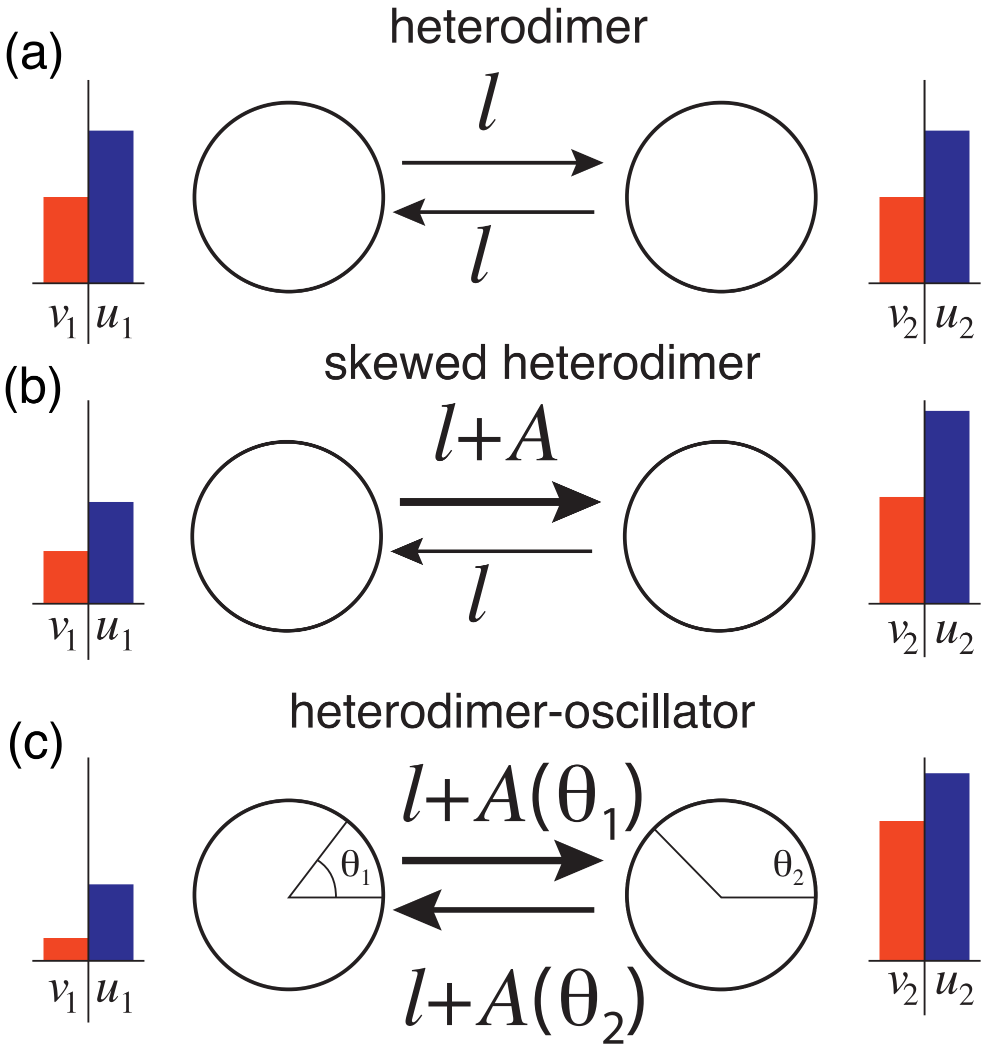

Figure 5.1: Overview of the heterodimer variations. *(a)* The original heterodimer model, with healthy and toxic species transported between the nodes at equal rates. *(b)* The skewed heterodimer model where node 1 has higher activity and thus increases the transport rate into node 2. Note that toxic species do not affect the activity parameter A. *(c)* The heterodimer-oscillator model, where each node harbors an oscillator operating at a faster time rate than the spreading process. The oscillators are coupled, and their frequency determines the transport rate of species between the nodes; in this illustration, node 1 has a higher frequency. Conversely, the toxic species affect the intrinsic frequency of the oscillators.

of the system's Jacobian matrix evaluated at the healthy fixed point. Hence, we conclude that the healthy state is stable for $\kappa \leq 0$ and the toxic fixed point is stable for $\kappa > 0$.

5.2.2 The skewed heterodimer model

To understand the effect of activity dynamics on spreading, we now consider a constant difference in activity between the nodes, $A \geq 0$, that affects the spreading as shown in Figure 5.1b. More specifically, we assume that the activity in node 2 is zero, while the activity in node 1 is at a constant level given by $A \geq 0$. For now, we exclude the effect that spreading may have on activity dynamics. Assuming that the activity process $A > 0$ taking place in node 1 increases spreading out of itself and into its neighbor, we obtain a *skewed heterodimer model* where the concentrations evolve according to

$$\dot{u}_1 = -(\ell + A)u_1 + \ell u_2 + k_0 - k_1 u_1 - k_2 u_1 v_1, \tag{5.6a}$$

$$\dot{v}_1 = -(\ell + A)v_1 + \ell v_2 - k_3 v_1 + k_2 u_1 v_1, \tag{5.6b}$$

$$\dot{u}_2 = (\ell + A)u_1 - \ell u_2 + k_0 - k_1 u_2 - k_2 u_2 v_2, \tag{5.6c}$$

$$\dot{v}_2 = (\ell + A)v_1 - \ell v_2 - k_3 v_2 + k_2 u_2 v_2. \tag{5.6d}$$

If $A = 0$ we recover (5.3). For the skewed heterodimer model (5.6), there is a single healthy fixed point

$$u_1^{\mathrm{H}} = \frac{k_0(2\ell + k_1)}{k_1(2\ell + A + k_1)}, \quad u_2^{\mathrm{H}} = \frac{k_0(2(\ell + A) + k_1)}{k_1(2\ell + A + k_1)}, \quad v_1^{\mathrm{H}} = v_2^{\mathrm{H}} = 0. \tag{5.7a}$$

Note that introducing A breaks the symmetry in the healthy fixed point between the two nodes, which previously were independent of ℓ. Eliminating u_1, u_2 and v_1 from the first fixed points, we find a cubic equation for the toxic fixed point ($v_2^{\mathrm{T}} \neq 0$) given by

$$c_0 + c_1 v_2 + c_2 v_2^2 + c_3 v_2^3 = 0$$

with coefficient values given in Appendix A.

We linearize the vector field at the healthy fixed point to identify transitions between healthy and toxic states. The eigenvalues of the Jacobian at the healthy fixed point are

$$\lambda_1 = -k_1 - 2\ell - A, \qquad \lambda_2 = -k_1, \tag{5.8a}$$

$$\lambda_3 = \frac{\kappa - \zeta}{k_1}, \qquad \lambda_4 = \frac{\kappa + \kappa^{\mathrm{crit}}}{k_1}, \tag{5.8b}$$

where κ^{crit} and ζ are given by

$$\kappa^{\text{crit}} = k_1(2\ell + A)\frac{\sqrt{s_0^2 + s_1} - s_0}{2s_0}, \tag{5.9a}$$

$$\zeta = k_1(2\ell + A)\frac{\sqrt{s_0^2 + s_1} + s_0}{2s_0}, \tag{5.9b}$$

with constants $s_0 = k_1(2\ell + A)(2\ell + A + k_1)$, $s_1 = 4A^2k_0k_2(k_1(2\ell + A + k_1) + k_0k_2)$. Since all parameters are positive, it follows that $\kappa^{\text{crit}} \geq 0$ and $\zeta \geq 0$. As such, we have that $\lambda_3 \leq \lambda_4$ and $\lambda_1 < \lambda_2 < 0$, and hence λ_4 dictates the stability of the healthy fixed point. The fixed point switches stability at a critical value $\kappa = -\kappa^{\text{crit}}$, from which we can easily separate k_3. Freezing all parameters but the toxic clearance rate k_3, we look at the bifurcation in terms of the parameter k_3, with critical value

$$k_3^{\text{crit}} = \frac{k_0k_2 + \kappa^{\text{crit}}}{k_1}, \tag{5.10}$$

which satisfies $k_0k_2/k_1 \leq k_3^{\text{crit}} \leq 2k_0k_2/k_1$ and is monotonically increasing in A (see Appendix A). Introducing the activity parameter A shifts the transcritical bifurcation to higher values with respect to k_3. The effect of activity is to *destabilize* the healthy fixed point as shown in Figure 5.2. Equivalently, in terms of neuroscientific applications, heterogeneous neuronal activity pushes neurons toward pathology.

It is interesting to understand the behavior of the toxic equilibrium as a function of the activity. Assuming that activity A is small compared to ℓ, we can expand the toxic equilibrium to first order in A to obtain

$$u_1^{\text{T}} = \frac{k_3}{k_2}\left(1 + \frac{\kappa - 2k_3\ell}{4k_3\ell^2 + 2k_0k_2\ell + k_3\kappa}A\right) + \mathcal{O}(A^2), \tag{5.11a}$$

$$u_2^{\text{T}} = \frac{k_3}{k_2}\left(1 - \frac{\kappa - 2k_3\ell}{4k_3\ell^2 + 2k_0k_2\ell + k_3\kappa}A\right) + \mathcal{O}(A^2), \tag{5.11b}$$

$$v_1^{\text{T}} = \frac{\kappa}{k_2k_3}\left(1 - \frac{2k_3\ell + k_3^2 + k_0k_2}{4k_3\ell^2 + 2k_0k_2\ell + k_3\kappa}A\right) + \mathcal{O}(A^2), \tag{5.11c}$$

$$v_2^{\text{T}} = \frac{\kappa}{k_2k_3}\left(1 + \frac{2k_3\ell + k_3^2 + k_0k_2}{4k_3\ell^2 + 2k_0k_2\ell + k_3\kappa}A\right) + \mathcal{O}(A^2), \tag{5.11d}$$

We see that activity can affect the fixed point in two distinct ways (assuming $\kappa > 0$ so that the healthy fixed point is unstable): If $\kappa - 2k_3\ell > 0$, then u_1 increases while v_1 decreases and u_2 decreases while v_2 increases. By contrast, if $\kappa - 2k_3\ell < 0$ is small, then u_1 decreases while v_1 decreases, and u_2 increases while v_2 increases. In the former case, the conversion process dominates, and the effective conversion at node 1 has decreased while increasing in node 2. In the latter case, the transport process

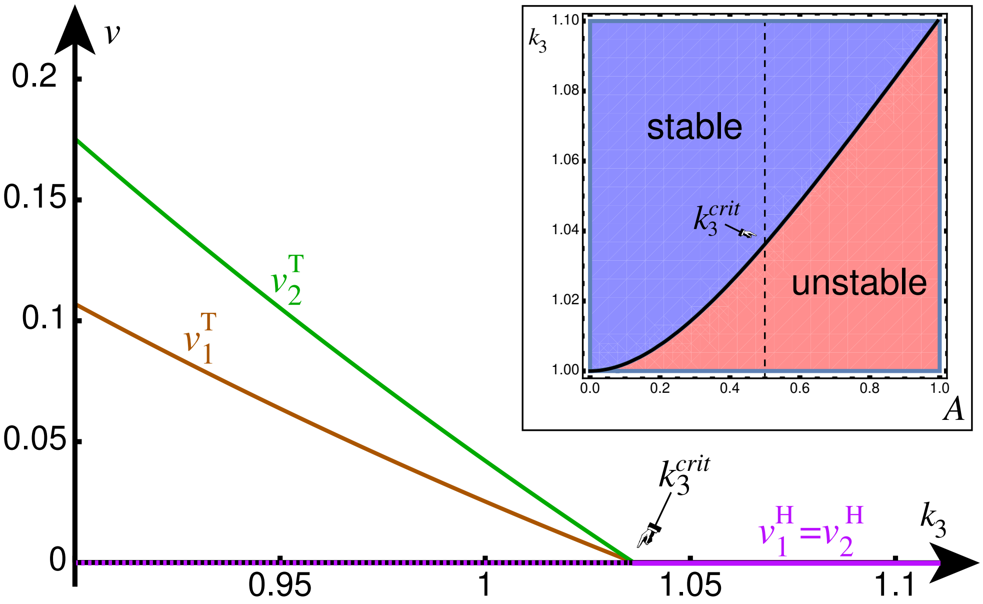

Figure 5.2: Bifurcation diagram for toxic load in nodes 1 and 2 as a function of toxic clearance k_3; other parameters are $A = 1/2, \ell = 1, k_0 = 1, k_1 = 1, k_2 = 1$. Inset: Bifurcation in (A,k_3) parameter space. Increasing activity destabilizes the healthy fixed point by shifting the transcritical bifurcation.

dominates, and both species at node 1 are being shunted over to node 2. This *shunting* phenomenon does not occur in the original heterodimer model and is showcased in Figure 5.3.

5.3 Coupling heterodimer dynamics with oscillatory activity

In the previous analysis, we considered the activity A to be a constant. In the brain, activity may relate to neural oscillations, which are fast compared to disease progression. Therefore, we now assume that A is determined by the evolution of a pair of phase oscillators with Kuramoto coupling. Since the spreading and activity processes evolve on different time scales, the coupling between the two systems defines a slow-fast dynamical system.

5.3.1 Two coupled phase oscillators

First, consider two phase oscillators, one on each node, with Kuramoto coupling (as introduced briefly in Section 3.1.1). That is, the state of the oscillation on node

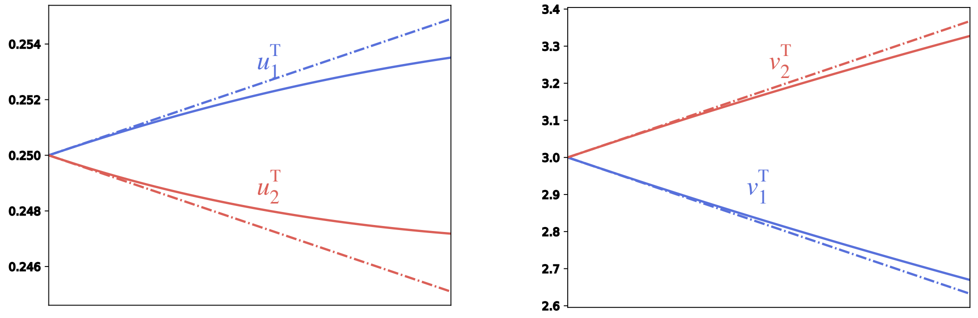

low toxic clearance

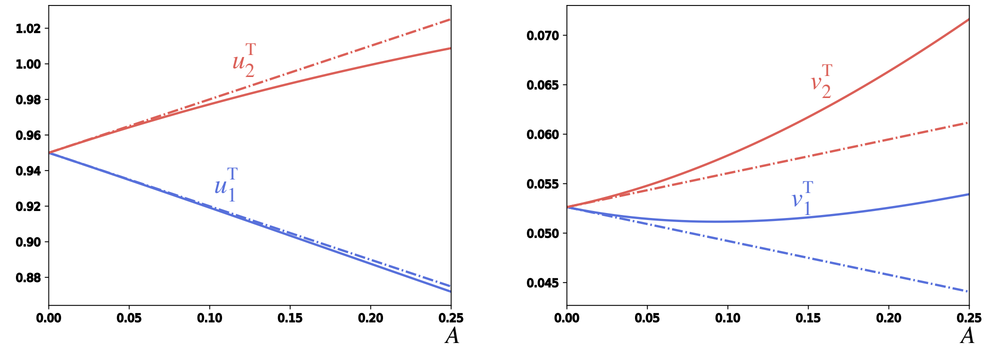

high toxic clearance

Figure 5.3: Comparison of steady-states of healthy and toxic species in nodes 1 (blue) and 2 (red) determined by simulation (solid lines) and first-order Taylor expansion (stippled line) of the activity parameter A. The upper row demonstrates the conversion-dominated regime, whereas the bottom row demonstrates the shunting-dominated regime. All parameters are set to 1, except for $k_3 = 0.25$ in the first row (far from the transcritical bifurcation at $k_3^{\text{crit}} = 1$) and $k_3 = 0.95$ in the second row (close to the transcritical bifurcation).

$i \in \{1, 2\}$ is given by a phase $\theta_i \in \mathbb{S}$ that evolves according to

$$\dot{\theta}_1 = \omega_1 + \frac{K}{2} \sin{(\theta_2 - \theta_1)}, \tag{5.12a}$$

$$\dot{\theta}_2 = \omega_2 + \frac{K}{2} \sin{(\theta_1 - \theta_2)}, \tag{5.12b}$$

where $\omega_i > 0$ are the intrinsic frequencies of the nodes and $K \geq 0$ is the *coupling strength*. Since the coupling depends solely on the phase difference, the dynamics are completely determined by the evolution of the phase difference $\phi := \theta_1 - \theta_2$ determined by

$$\dot{\phi} = \Delta\omega - K \sin\phi, \tag{5.13}$$

where $\Delta\omega = \omega_1 - \omega_2$ is assumed to be positive, without loss of generality. For $K > |\Delta\omega|$, there are two fixed points (one unstable and one stable attracting all initial conditions except the unstable fixed point). For $K < |\Delta\omega|$, there are no fixed points, and any solution $\phi(t)$ is periodic. There is a saddle-node bifurcation at the critical coupling strength $K = |\Delta\omega|$. Hence, depending on the dynamics, we have two regimes: the strong-coupling regime (fixed points) and the weak-coupling regime (periodic orbit).

We assume that the activity at each node is related to the *instantaneous frequencies*, $\dot{\theta}_1$ and $\dot{\theta}_2$, of each node. We define the *average frequency* of each oscillator:

$$\Omega_i = \lim_{T\to\infty} \frac{1}{T} \int_0^T \dot{\theta}_i(t) \mathrm{d}t, \tag{5.14}$$

which is independent of the initial conditions. In the strong-coupling regime (the coupling between oscillators is strong compared to the frequency mismatch, and the phase difference ϕ converges to a fixed point), the oscillators are frequency locked. At the fixed points, we have a constant instantaneous frequency $\dot{\theta}_1(t) = \dot{\theta}_2(t) = \langle\omega\rangle := (\omega_1 + \omega_2)/2$, which implies

$$\Omega_1 = \Omega_2 = \langle\omega\rangle. \tag{5.15}$$

In the weak-coupling regime (the coupling between the oscillators is weak compared to their frequency mismatch, so the phase difference undergoes periodic oscillations), we compute the average frequencies Ω_i through the average frequency difference

$$\Delta\Omega = \lim_{T\to\infty} \frac{1}{T} \int_0^T \dot{\phi}(t) \mathrm{d}t. \tag{5.16}$$

Define $\Delta T = 2\pi/\Delta\Omega$, assume $0 \leq K < \Delta\omega$, and let $\phi(t)$ be the ΔT-periodic solution of (5.13). Note that the sign of $\dot{\phi}$ is constant. With (5.13) we have

$$\Delta\Omega = \Delta\omega - K \lim_{T\to\infty} \frac{1}{T} \int_0^T \sin\phi(t) \mathrm{d}t, \tag{5.17}$$

With $m = T/|\Delta T|$, we can rewrite the integral as

$$\lim_{m\to\infty} \frac{1}{m|\Delta T|} \int_0^{m|\Delta T|} \sin\phi(t)\mathrm{d}t = \frac{1}{|\Delta T|} \int_0^{|\Delta T|} \sin\phi(t)\mathrm{d}t = \frac{\Delta\Omega}{K}\left(\frac{\Delta\omega}{\sqrt{\Delta\omega^2 - K^2}} - 1\right), \tag{5.18}$$

where the last equality follows from substituting t by ϕ (which is possible since the sign of $\dot{\phi}$ is constant) and solving the resulting integral by Weierstrass substitution. Using this last expression in (5.17) yields

$$\Delta\Omega = \sqrt{\Delta\omega^2 - K^2}, \tag{5.19}$$

from which we compute the asymptotic frequencies of each node

$$\Omega_1 = \langle\omega\rangle + \frac{\sqrt{\Delta\omega^2 - K^2}}{2}, \tag{5.20a}$$

$$\Omega_2 = \langle\omega\rangle - \frac{\sqrt{\Delta\omega^2 - K^2}}{2}. \tag{5.20b}$$

5.3.2 Slow-fast heterodimer-oscillator dynamics

Next, we couple the oscillatory dynamics with the heterodimer protein-spreading model. The two processes will evolve on distinct time scales, determined by a small strictly positive constant $\epsilon \ll 1$, representing the ratio between the fast activity time scale and the slow spreading time scale. Specifically, the two-node *heterodimer-oscillator* (see Fig. 5.1c) system is

$$\dot{u}_1 = -(\ell + \delta A_1(\phi))u_1 + (\ell + \delta A_2(\phi))u_2 + k_0 - k_1 u_1 - k_2 u_1 v_1, \tag{5.21a}$$

$$\dot{v}_1 = -(\ell + \delta A_1(\phi))v_1 + (\ell + \delta A_2(\phi))v_2 - k_3 v_1 + k_2 u_1 v_1, \tag{5.21b}$$

$$\dot{u}_2 = (\ell + \delta A_1(\phi))u_1 - (\ell + \delta A_2(\phi))u_2 + k_0 - k_1 u_2 - k_2 u_2 v_2, \tag{5.21c}$$

$$\dot{v}_2 = (\ell + \delta A_1(\phi))v_1 - (\ell + \delta A_2(\phi))v_2 - k_3 v_2 + k_2 u_2 v_2, \tag{5.21d}$$

$$\epsilon\dot{\theta}_1 = \widehat{\omega}_1(v_1) + \frac{K}{2}\sin(\theta_2 - \theta_1), \tag{5.21e}$$

$$\epsilon\dot{\theta}_2 = \widehat{\omega}_2(v_2) + \frac{K}{2}\sin(\theta_1 - \theta_2), \tag{5.21f}$$

where $\delta > 0$ scales the oscillators' effect on spreading. We assume that the coupling between heterodimer and oscillatory dynamics is through the phase-dependent activity of nodes 1 and 2, that is,

$$A_1(\phi) = \epsilon\dot{\theta}_1, \quad A_2(\phi) = \epsilon\dot{\theta}_2, \tag{5.22}$$

and the intrinsic frequencies

$$\widehat{\omega}_1(v_1) = \omega_1 - cv_1, \quad \widehat{\omega}_2(v_2) = \omega_2 - cv_2, \tag{5.23}$$

which are decreased by toxic proteins by a scaling parameter $c > 0$. As discussed above, we may replace the phase dynamics in (5.21) by the evolution of the phase difference ϕ as above given by

$$\epsilon\dot{\phi} = \Delta\omega - c\Delta v - K\sin\phi, \tag{5.24}$$

where $\Delta v = v_1 - v_2$ is the difference in toxic protein concentration. The phase locking behavior is now determined by the effective intrinsic frequency difference $\Delta\widehat{\omega} = \widehat{\omega}_1 - \widehat{\omega}_2 = \Delta\omega - c\Delta v$, which is a function of Δv. As there is no sensible interpretation of *negative* neuronal activity, we will only consider parameters for which $A_i(t) \geq 0, i \in \{1, 2\}$ for all t, which implies that the intrinsic frequencies are positive $\omega_i > 0$.

Given that the spreading dynamics is much slower than the oscillator dynamics (on the order of years versus seconds), we are interested in the dynamics for small ϵ close to the singular limit $\epsilon \to 0$. In the singular limit, the phase dynamics relax instantaneously to the asymptotic dynamics of the phase-difference $\phi(t)$. Thus, the dynamics in the singular limit depend on which dynamical regime the phase difference is operating in. In the phase-locked regime, the dynamics relax instantaneously to equilibrium, which defines the critical manifold of the slow-fast system on which A_i takes its value at equilibrium. In the regime where the phase difference $\phi(t)$ is drifting, we replace the instantaneous frequency in A_i by the temporal average Ω_i; this is similar to the approach by Thiele *et al.* [196]. Finally, we consider the system at the border between the two regimes.

5.3.3 The phase-locking regime

Assume that $|\Delta\widehat{\omega}(\Delta v)| \leq K$. Then, the singular-limit dynamics on the slow manifold is determined by the stable phase-difference equilibria

$$\phi = \sin^{-1}\left(\frac{\Delta\omega - c\Delta v}{K}\right). \tag{5.25}$$

Inserting the fixed point into A_i, both nodes have identical activities

$$A_1 = A_2 = \langle\omega\rangle - \frac{c(v_1 + v_2)}{2}. \tag{5.26}$$

Substituting these expressions into the slow system gives us the dynamics on the phase-locking critical manifold.

Since the nodes have identical activity levels, the dynamics are qualitatively equivalent to those of the isolated heterodimer model. In particular, the system has the same pair of healthy and toxic fixed points as the heterodimer model given by (5.4):

$$u_1^{\mathrm{H,P}} = u_2^{\mathrm{H,P}} = \frac{k_0}{k_1}, \quad v_1^{\mathrm{H,P}} = v_2^{\mathrm{H,P}} = 0, \tag{5.27a}$$

$$u_1^{\mathrm{T,P}} = u_2^{\mathrm{T,P}} = \frac{k_3}{k_2}, \quad v_1^{\mathrm{T,P}} = v_2^{\mathrm{T,P}} = \frac{\kappa}{k_2 k_3}. \tag{5.27b}$$

The eigenvalues of the Jacobian matrix determine the stability of the healthy fixed point:

$$\lambda_1 = -k_1 - 2(\ell + \delta\langle\omega\rangle), \qquad \lambda_2 = -k_1, \tag{5.28a}$$

$$\lambda_3 = \frac{\kappa}{k_1} - 2(\ell + \delta\langle\omega\rangle), \qquad \lambda_4 = \frac{\kappa}{k_1}. \tag{5.28b}$$

Thus, the healthy fixed point loses its stability at $\kappa = 0$.

The assumption of being in the phase-locking regime, $|\Delta\widehat{\omega}(\Delta v)| < K$, gives a consistency condition for the existence of the fixed points on the critical manifold. Note that since the activity of each node in the phase-locking regime is identical, the slow dynamics is symmetric in the sense that exchanging the two nodes has no impact on the dynamics. As such, for both fixed points, the nodes are "equal" in the sense that they take the same state and satisfy $\Delta v = 0$. Thus, the healthy and toxic fixed points only exist as fixed points on the critical manifold for the slow dynamics if $|\Delta\widehat{\omega}(0)| = |\Delta\omega| \leq K$.

5.3.4 The drifting regime

Outside the phase-locked regime, $|\Delta\widehat{\omega}(\Delta v)| > K$, the fast oscillatory dynamics do not relax to equilibrium but evolve on a periodic orbit. As these oscillations are much faster than the evolution of the slow dynamics, we average out the fast oscillations by replacing the activities A_i by their temporal averages to define the *drifting regime*. Specifically, replacing ω_i with $\widehat{\omega}_i(v_i)$ in (5.20) and assuming, without loss of generality, that $\Delta\widehat{\omega} \geq 0$ yields the activities

$$A_1(v) := \epsilon\widehat{\Omega}_1 = \langle\omega\rangle - \frac{c(v_1 + v_2) - \sqrt{(\Delta\widehat{\omega}(\Delta v))^2 - K^2}}{2}, \tag{5.29a}$$

$$A_2(v) := \epsilon\widehat{\Omega}_2 = \langle\omega\rangle - \frac{c(v_1 + v_2) + \sqrt{(\Delta\widehat{\omega}(\Delta v))^2 - K^2}}{2}. \tag{5.29b}$$

Substituting these activities into the dynamical equations for the slowly evolving heterodimer equations yields the dynamics of the drifting regime. As the activities of the two nodes are now distinct, the dynamics is similar to the skewed heterodimer model in Section 5.2.2. There is one healthy fixed point $u^{\mathrm{H,D}}$ in the drifting regime with coefficients

$$u_1^{\mathrm{H,D}} = \frac{k_0}{k_1}\left(1 - \delta\frac{\sqrt{\Delta\omega^2 - K^2}}{k_1 + 2\ell + 2\delta\langle\omega\rangle}\right), \tag{5.30a}$$

$$u_2^{\mathrm{H,D}} = \frac{k_0}{k_1}\left(1 + \delta\frac{\sqrt{\Delta\omega^2 - K^2}}{k_1 + 2\ell + 2\delta\langle\omega\rangle}\right), \tag{5.30b}$$

$$v_1^{\mathrm{H,D}} = v_2^{\mathrm{H,D}} = 0, \tag{5.30c}$$

under the assumption that $|\Delta\widehat{\omega}(0)| = |\Delta\omega| \geq K$. Similar to the skewed heterodimer model, the symmetry of the fixed points is broken. The eigenvalues of the Jacobian matrix determine the linear stability of the healthy fixed point:

$$\lambda_1 = -k_1 - 2(\ell + \delta\langle\omega\rangle), \qquad \lambda_2 = -k_1, \tag{5.31a}$$

$$\lambda_3 = \frac{\kappa - \zeta}{k_1}, \qquad \lambda_4 = \frac{\kappa + \kappa^{\mathrm{crit}}}{k_1}, \tag{5.31b}$$

where

$$\kappa^{\mathrm{crit}} = k_1(\ell + \delta\langle\omega\rangle)\frac{\sqrt{s_0^2 + s_1} - s_0}{s_0},$$

$$\zeta = k_1(\ell + \delta\langle\omega\rangle)\frac{\sqrt{s_0^2 + s_1} + s_0}{s_0},$$

with $s_0 = 2k_1(\ell + \delta\langle\omega\rangle)(k_1 + 2\ell + 2\delta\langle\omega\rangle)$ and $s_1 = 4\delta^2 k_0 k_2(\Delta\omega^2 - K^2)(k_0 k_2 + k_1(k_1 + 2\ell + 2\delta\langle\omega\rangle))$. Remembering that the healthy fixed point only exists for $|\Delta\omega| \geq K$, we can assert that $\kappa^{\mathrm{crit}}, \zeta \geq 0$, as is verifiable by inspecting s_1. As such, λ_4 determines the stability of $u^{\mathrm{H,D}}$. The critical value for k_3^{crit} at which the transcritical bifurcation occurs is

$$k_3^{\mathrm{crit}} = \frac{k_0 k_2 + \kappa^{\mathrm{crit}}}{k_1}. \tag{5.32}$$

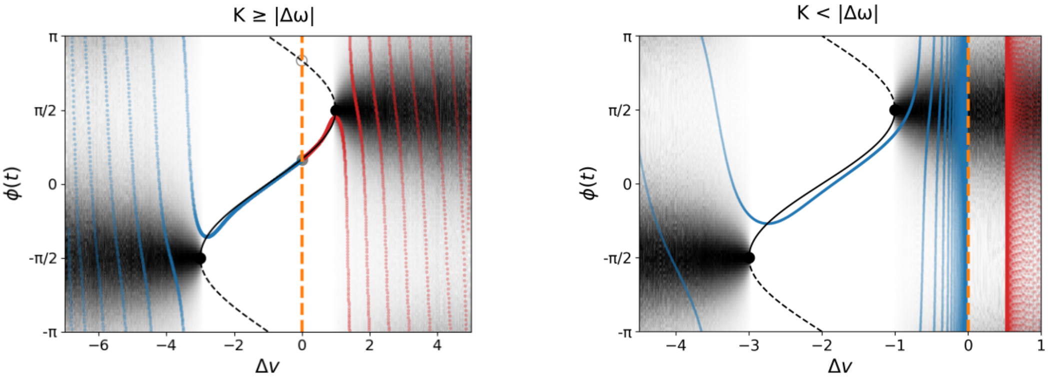

Figure 5.4: Summary of the dynamics in the phase-locking and drifting regime with simulations in the healthy (blue) and toxic (red) regimes of the heterodimer-oscillator with $\epsilon > 0$. *Left:* Summary for $K > \Delta\omega$ over the phase-difference and toxic species difference, where $K = 2, \Delta\omega = 1, c = 1, k_0 = 1, k_1 = 1, k_2 = 1, \delta = 1, \ell = 10^{-3}$ with forward solutions in the toxic ($\epsilon = 0.2$, $k_3 = 0.75$) and healthy regime ($\epsilon = 0.075$, $k_3 = 1.25$). Both forward solutions are symmetric with respect to the slow variables. *Right:* Summary for $K < \Delta\omega$ where $K = 1, \Delta\omega = 2, c = 1, k_0 = 1.5, k_1 = 1, k_2 = 1, \delta = 1, \ell = 10^{-3}$ and with forward solutions in toxic ($\epsilon = 0.1, k_3 = 0.125$) and healthy regimes ($\epsilon = 0.075, k_3 = 1.25$). Both forward solutions are asymmetric with respect to the slow variables (the healthy solution is asymmetric with respect to the healthy species). Note that the trajectories in the healthy regimes converge to $\Delta v = 0$ (highlighted with a stippled, orange line) in both diagrams.

Assuming δ small compared to ℓ, we expand the toxic fixed point $u^{\mathrm{T,D}}$ in the drifting regime to first order in δ, giving us

$$u_1^{\mathrm{T,D}} = \frac{k_3}{k_2}\left(1 + \delta\frac{(\kappa - 2k_3\ell)\sqrt{\Delta\omega^2 - K^2}}{4k_3\ell^2 + 2k_0k_2\ell + k_3\kappa}\right) + \mathcal{O}(\delta^2), \tag{5.33a}$$

$$u_2^{\mathrm{T,D}} = \frac{k_3}{k_2}\left(1 - \delta\frac{(\kappa - 2k_3\ell)\sqrt{\Delta\omega^2 - K^2}}{4k_3\ell^2 + 2k_0k_2\ell + k_3\kappa}\right) + \mathcal{O}(\delta^2), \tag{5.33b}$$

$$v_1^{\mathrm{T,D}} = \frac{\kappa}{k_2k_3}\left(1 - \delta\frac{(2k_3\ell + k_3^2 + k_0k_2)\sqrt{\Delta\omega^2 - K^2}}{4k_3\ell^2 + 2k_0k_2\ell + k_3\kappa}\right) + \mathcal{O}(\delta^2), \tag{5.33c}$$

$$v_2^{\mathrm{T,D}} = \frac{\kappa}{k_2k_3}\left(1 + \delta\frac{(2k_3\ell + k_3^2 + k_0k_2)\sqrt{\Delta\omega^2 - K^2}}{4k_3\ell^2 + 2k_0k_2\ell + k_3\kappa}\right) + \mathcal{O}(\delta^2), \tag{5.33d}$$

where the coefficients are similar to the expansion of the skewed heterodimer toxic fixed point, except that they are scaled by $\sqrt{\Delta\omega^2 - K^2}$. As such, we have transport- and conversion-dominated behavior for small and large values of $\kappa - 2k_3\ell$, respectively. More importantly, we have established the existence of a toxic fixed point $u^{\mathrm{T,D}}$ in the drifting regime for small δ.

Note that the above coefficients are only defined for $K \leq |\Delta\omega|$, similarly to $u^{\mathrm{H,D}}$. As such, our preceding analysis suggests a symmetry-breaking global bifurcation oc-

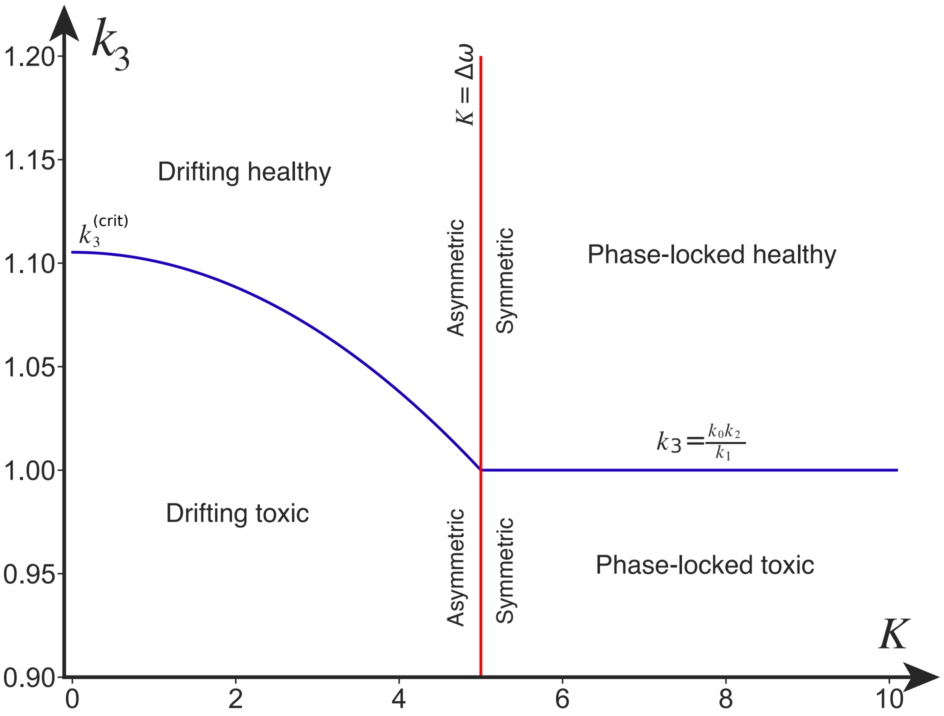

Figure 5.5: Summary of the dynamics of the 2-node heterodimer-oscillator in the singular limit ($\epsilon \to 0$). The labels in each quadrant state which fixed point we know to be stable. The transcritical bifurcation in the weak-coupling and strong-coupling regimes is presented, together with the breaking of the symmetry between the two nodes in the fixed points, which occurs at $K = |\Delta\omega|$. Parameters are $k_0 = 1, k_1 = 1, k_2 = 1, \ell = 1, \omega_1 = 10, \omega_2 = 5, \delta = 5$.

curring at $K = |\Delta\omega|$ in which from one side (from the phase-locking regime), two fixed point branches collide and disappear (saddle-node bifurcation on an invariant circle). But, from the other side (from the drifting regime,) two periodic solutions collide and disappear. Furthermore, the fixed points in the phase-locking regime are symmetric between the nodes with respect to their heterodimer variables, whereas both the periodic solutions are asymmetric in this respect. A summary of the heterodimer-oscillator dynamics in the strong-coupling and weak-coupling regimes can be found in Figure 5.4 alongside numerical solutions for $\epsilon > 0$. Moreover, an overview of the dynamical regimes and the (singular-limit) transcritical bifurcation is illustrated in (K, k_3) parameter space in Figure 5.5.

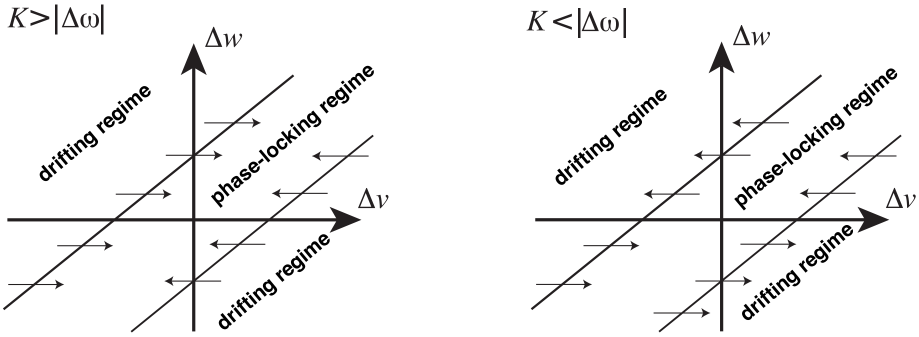

Figure 5.6: The vector field of Δv in terms of $\Delta\omega$ and Δv in the strong-coupling (left) and weak-coupling regime (right). The inner region in both diagrams is the phase-locking regime, and the outer regions are the drifting regime. We see that for strong coupling $K > |\Delta\omega|$, the vector field points inwards to the phase-locking regime. However, for the weak-coupling regime $K < |\Delta\omega|$, the vector field points to the left-hand drifting regime for $\Delta\omega > 0$ (node 1 is more active than node 2) and to the right-hand drifting regime for $\Delta\omega < 0$ (node 2 is more active than node 1).

5.3.5 Transitions between the phase-locking and drifting regimes

With an understanding of the dynamics within the phase-locking (Section 5.3.3) and drifting regimes (Section 5.3.4) at hand, we can now elucidate possible transitions between the regimes. The boundary between the regimes is where the fast dynamics undergo a saddle-node bifurcation at $|\Delta\widehat{\omega}(\Delta v)| = |\Delta\omega - c\Delta v| = K$. Equivalently, we obtain the following condition for the regime border

$$\Delta v = \frac{\Delta\omega \pm K}{c}. \tag{5.34}$$

The value of Δv is subject to the slow dynamics (5.21). Specifically, the sign of $(\Delta v)^{\cdot} := \frac{\mathrm{d}}{\mathrm{d}t}(\Delta v)$ determines the transitions between the phase-locking and drifting regimes: For the right boundary of the phase-locking regime, $\Delta v = \frac{\Delta\omega+K}{c}$, negative $(\Delta v)^{\cdot}$ indicates that the slow flow points from the drifting regime into the phase-locking regime and a positive $(\Delta v)^{\cdot}$ in the opposite direction. For the left boundary, the conditions are the other way around. In the following, we will argue that, under certain assumptions, the flow points towards the phase-locking regime for $K > |\Delta\omega|$ and towards the drifting regime for $K < |\Delta\omega|$; this is sketched in Figure 5.6.

To determine the transitions between the regimes, we consider the dynamics of Δv. In the singular limit, the dynamics have relaxed to the saddle-node equilibrium, and thus, $A^* := A_1 = A_2$. Now we assume that the u_i take their equilibrium values, with

$u_1 = u_2 = k_0/k_1$ (healthy regime) and $u_1 = u_2 = k_3/k_2$ (toxic regime); $u_1 = u_2 =: u^*$ in either case. According to (5.21), the evolution of Δv is determined by

$$(\Delta v)^{\dot{}} = -(2\ell + \delta A^* + (k_3 - k_2 u^*))\Delta v. \tag{5.35}$$

We claim that the first factor is not positive (i.e., the quantity in the parentheses is not negative). The first two terms are positive since $\ell \geq 0$ and, by assumption, $A^* \geq 0$. For the third term, $k_3 - k_2 u^* \geq 0$ is equivalent to $u^* \leq k_3/k_2$. But, by assumption, $u^* = k_3/k_2$ or $u^* = k_0/k_1 \leq k_3/k_2$, so in either case, the third term is not negative. We conclude that the sign of $(\Delta v)^{\dot{}}$ only depends on the sign of Δv. For the right boundary of the phase-locking regime, we have $\Delta v = (\Delta\omega + K)/c$ so $\Delta v > 0$ or equivalently $K > -\Delta\omega$ implies $(\Delta v)^{\dot{}} \leq 0$ (flow towards the phase-locking regime). Conversely, $K < -\Delta\omega$ implies $(\Delta v)^{\dot{}} \geq 0$ (flow towards the drifting regime). Similarly, for the left boundary of the phase-locking regime, we have $\Delta v = (\Delta\omega - K)/c$, so $K < \Delta\omega$ implies $(\Delta v)^{\dot{}} \leq 0$ (flow towards the drifting regime) and $K > \Delta\omega$ implies $(\Delta v)^{\dot{}} \geq 0$ (flow towards the phase-locking regime).

Thus, in terms of the system parameters, the crucial quantity is the oscillator coupling relative to the intrinsic frequency mismatch. If $K > |\Delta\omega|$, the flow points towards the phase-locking regime on either boundary. If $K < |\Delta\omega|$, then the flow points in the same direction on each boundary, and the direction is determined by the sign of Δv. These cases are illustrated in Figure 5.6.

5.3.6 Extending the parameter regime

From the beginning, we have assumed c and δ to be positive. These assumptions, however, may not be fit for all applications of the heterodimer-oscillator model. For example, one might envision spreading processes that *increases* oscillatory activity locally ($c < 0$), and, in return, oscillatory processes that *decreases* spreading to its neighboring oscillators ($\delta < 0$). First, we consider the case $c < 0$. None of the singular-limit fixed points nor their stability depend on c, and the regime border analysis above can be repeated successfully for $c < 0$ and $\delta > 0$ (noting that the left- and right-hand borders swap places). For $\delta < 0$, we may assume $\delta\langle\omega\rangle > -\ell$ to guarantee that our stability analysis of the phase-locking and drifting equilibria remains unaffected (see eigenvalues in (5.28) and (5.31)). The assumption is within reason; it is equivalent to stating that the link between the nodes $\ell + \delta A(\phi)$ does not change signs for $\Delta v = 0$. For the regime border analysis to hold, we require $\delta \geq -2\ell/A^*_{\max}$ where $A^*_{\max}$ is the maximum of the phase-locked activity over v_1 and v_2 (see (5.26)). For $c > 0$, we have that $A^*_{\max} = \langle\omega\rangle$ giving $\delta\langle\omega\rangle \geq -2\ell$, which is already satisfied by $\delta\langle\omega\rangle > -\ell$. However, $A^*_{\max}$ increases indefinitely in v_1 and v_2 for $c < 0$. Hence, we need additional bounds on the variables v_1 and v_2 to ensure that the regime border analysis holds. Although the regime border analysis cannot be repeated for $c, \delta < 0$ without further assumptions, we conclude that the fixed point linear stability analysis generalizes to $c, \delta \in \mathbb{R}$,

5.4 Activity-spreading feedback on networks

Investigating the dynamics of the heterodimer-oscillator system on more general networks, we find that the results from the 2-node heterodimer-oscillator system provide a strong intuition for the generalized network dynamics. Specifically, we consider a network of N nodes determined by the $N \times N$ (weighted) adjacency matrix $\mathbf{W}$ with Laplacian $\mathbf{L}$. Let $u, v \in \mathbb{R}^N$ denote the healthy and toxic species concentration at each node and $\theta \in \mathbb{S}^N$ the state of the oscillators on each node. Generalizing (5.21), the states evolve according to

$$\dot{u}_i = -\sum_{j=1}^{N} L_{ij}(1 + \delta A_j)u_j + k_0 - k_1 u_i - k_2 u_i v_i, \tag{5.36a}$$

$$\dot{v}_i = -\sum_{j=1}^{N} L_{ij}(1 + \delta A_j)v_j - k_3 v_i + k_2 u_i v_i, \tag{5.36b}$$

$$\epsilon\dot{\theta}_i = \omega_i - c v_i + K \sum_{j=1}^{N} W_{ij} \sin(\theta_j - \theta_i), \tag{5.36c}$$

for $i = 1, \dots, N$ where $A = \epsilon[\dot{\theta}_1, \dot{\theta}_2, \dots, \dot{\theta}_N]$.

5.4.1 Numerical exploration of key example networks

Erdős–Rényi random graphs. Erdős–Rényi graphs are randomly generated networks in which each link is included in the graph by the same probability [197]. Heterodimer-oscillator dynamics on Erdős–Rényi random graphs retain the transcritical bifurcation near $\kappa = 0$ alongside its symmetry for small differences between the intrinsic frequencies of the nodes; cf. Figure 5.7. However, with large differences in the intrinsic frequencies, the transcritical bifurcation extends the toxic parameter regime and breaks the symmetry of the fixed points between the nodes, as expected from our analysis of the 2-node system.

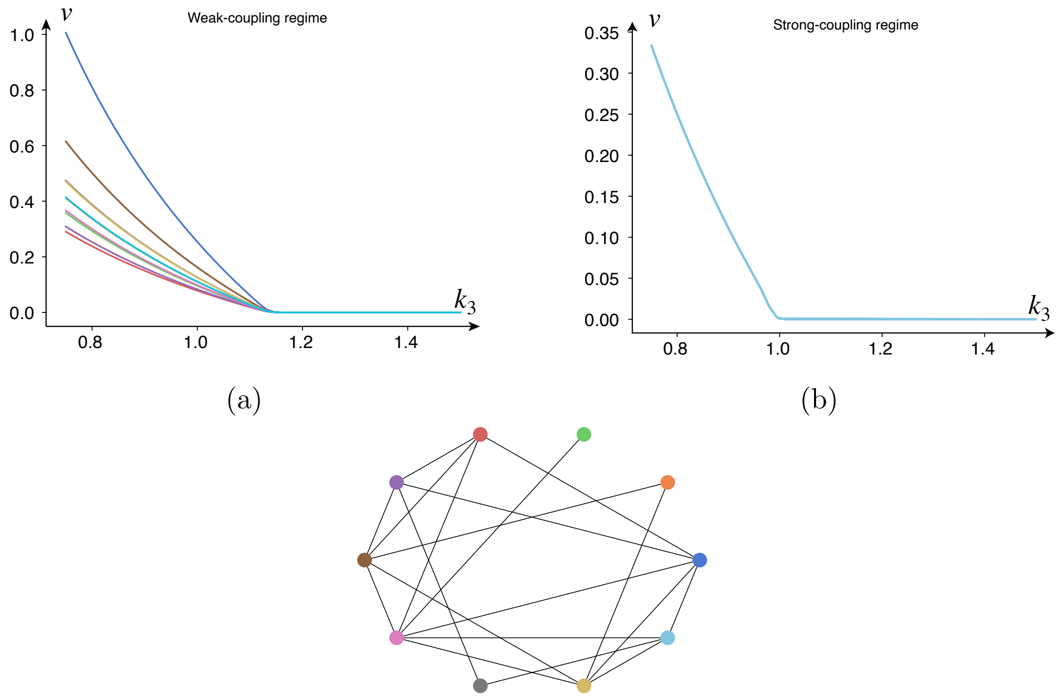

(a)

(b)

(c)

Figure 5.7: Simulations demonstrating the transcritical bifurcation during the weak-coupling and strong-coupling regime in a random graph. All weights in the network are set to 1, and the intrinsic frequencies were drawn from a normal distribution. *(a)* The weak-coupling parameters are $\rho = 0.1, k_0 = 1, k_1 = 1, k_2 = 1, E(\omega) = 10, \mathrm{Var}(\omega) = 0.25, c = 0.5, \epsilon = 10^{-3}, \delta = 10, K = 0.1$, while one of the oscillators (dark blue) is set at a slower frequency $\omega = 5$. *(b)* The strong-coupling parameters are $\rho = 0.1, k_0 = 1, k_1 = 1, k_2 = 1, E(\omega) = 10, \mathrm{Var}(\omega) = 0, c = 0.5, \epsilon = 10^{-3}, \delta = 10, K = 0.1$. *(c)* The Erdős–Rényi graph ($N = 10, p = 0.5$).

Chain graphs. A chain graph is a network of nodes connected, one by one, in a line (see Fig. 5.8e). To further test our intuition, we create a chain graph with decreasing frequencies along the chain. If we initialize a small amount of toxic species in each node, we expect (in the steady state) a gradient of increasing toxic species along the chain. This prediction is accurate, as observed in Figure 5.8. Additionally, we observe shunting behavior: First, the healthy species are quickly transported according to the nodes' activity gradient, and then the healthy species are converted into toxic species. According to our 2-node analysis, such shunting behavior should occur close to the original transcritical bifurcation $\kappa = 0$, which is where the simulation in Figure 5.8 has been parameterized.

Clustered networks. Many complex networks show high degrees of clustering. As such, we created a network of 3 fully connected clusters of 10 nodes each, where each cluster is connected to each other by two links chosen between a random node pair; cf. Figure 5.9. We then drew the intrinsic frequencies from normal distributions where each cluster has a different mean. That is, one cluster will be highly active, one will be moderately active, and one will be less active. By doing so, we will have 3 synchronized clusters that are weakly connected to each other. As before, we set the parameters in the toxic regime close to the original transcritical bifurcation at $\kappa = 0$. As shown in Figure 5.9, the simulations confirm the intuition from the 2-node system. At first, the healthy species are shunted towards the lesser active clusters, where they are subsequently converted into toxic species. Thus, the least active cluster produces the most toxic species, followed by the moderately active and highly active clusters. These simulations suggest that the heterodimer-oscillator might also be suitable for mean-field models of population dynamics.

5.4.2 Exploring activity-dependent spreading in Alzheimer's disease

Our original motivation was to investigate the effect that the slow-fast dynamics between neuronal activity and pathological protein spreading exert on the progression of neurodegenerative diseases. In the previous chapter, we modeled the progression of Alzheimer's disease as a spreading process on a network reconstruction of the human brain.

Hyperphosphorylated tau proteins start to aggregate at the entorhinal cortex and spread progressively to the hippocampus, the limbic system, and the neocortex. The successive spread of τP has been shown to follow a pattern, and, as such, the spreading

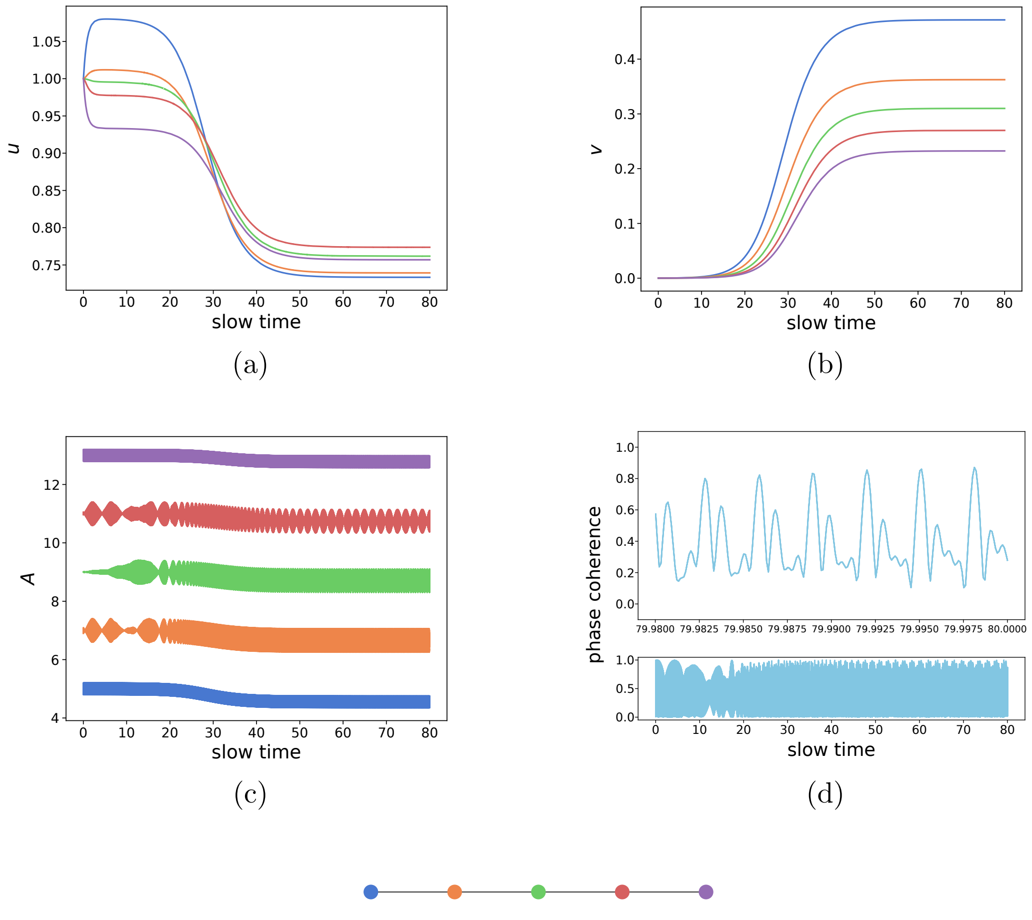

(a) (b)

(c) (d)

(e)

Figure 5.8: Simulations demonstrating heterodimer-oscillator dynamics on a chain network. All link weights are set to 0.1 while other parameters are $\rho = 0.5, k_0 = 1, k_1 = 1, k_3 = 0.75, k_2 = 1, \epsilon = 10^{-3}, \delta = 1\, K = 1, c = 0.5$. The natural frequencies of the nodes, ω_i, range from 5 to 15 with increments of 2.5. Colors are consistent across figure panels. *(a)* The evolution of healthy species. *(b)* The evolution of toxic species. *(c)* The activity (instantaneous frequencies) of the nodes. *(d)* The phase-coherence of the Kuramoto order parameter of the oscillators. *(e)* Graph of the network.

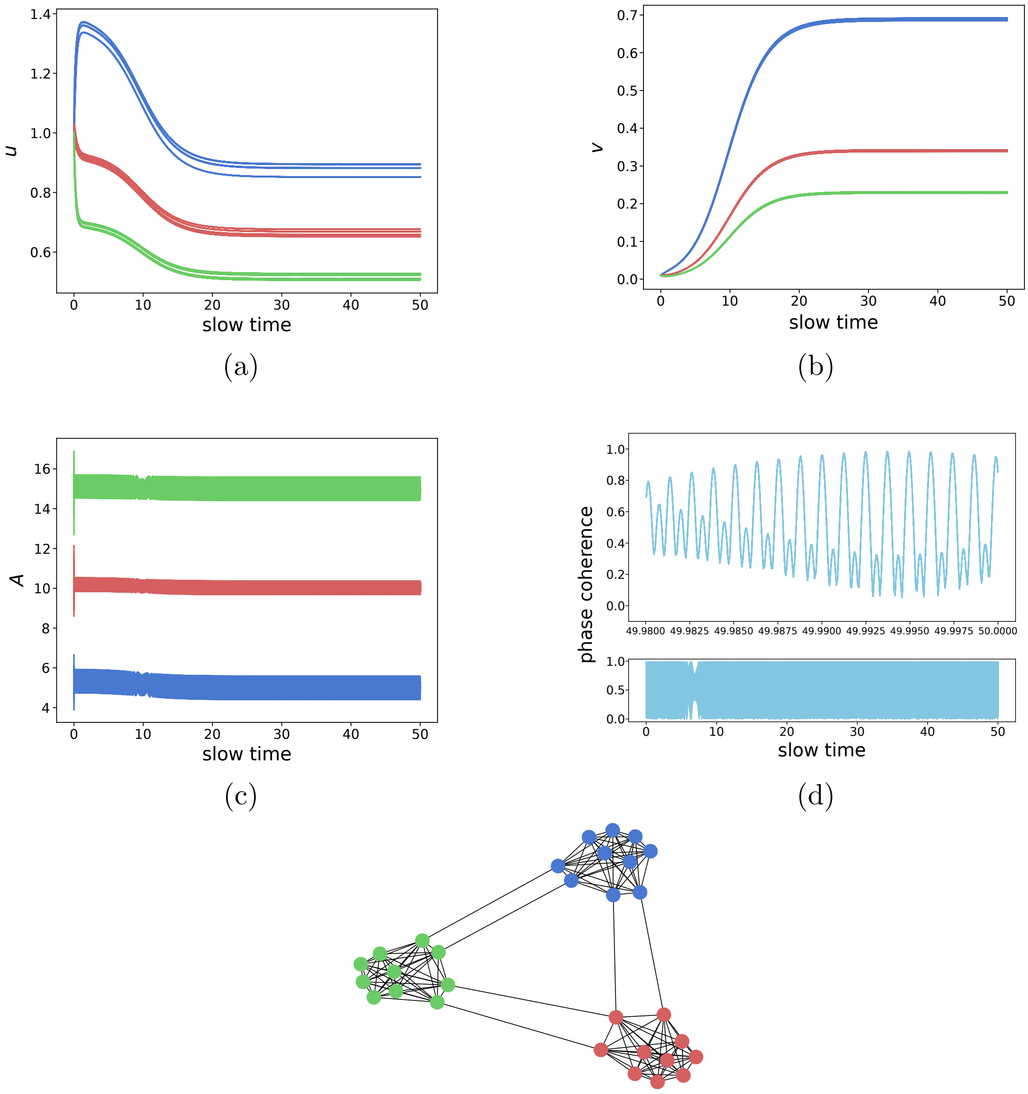

(a)

(b)

(c)

(d)

(e)

Figure 5.9: Simulations demonstrating heterodimer-oscillator dynamics on a clustered network. All network link weights are set to 0.1, while other parameters are $\rho = 0.5, k_0 = 1, k_1 = 1, k_3 = 0.75, k_2 = 1, \epsilon = 10^{-3}, \delta = 1\, K = 1, c = 0.5$. Clusters are colored green (highest activity), red (medium activity), and blue (lowest activity), respectively. The average intrinsic frequencies of the clusters, ω_i, are normally distributed with means 5 (blue), 10 (red), and 15 (green) and a common standard deviation of 0.5. *(a)* The evolution of healthy species. *(b)* The evolution of toxic species. *(c)* The activity (instantaneous frequencies) of the nodes *(d)* The phase-coherence of the Kuramoto order parameter of the oscillators. *(e)* Graph of the network.

of τP is divided into six stages known as the Braak staging scheme. However, not all patients follow the Braak staging scheme. Studies suggest that Alzheimer's patients fit into different subgroups based on their staging patterns [198, 199]. Furthermore, tau proteins are believed to be transported at a higher rate from higher-active neurons [200], and several studies suggest a crucial link between brain-wide correlations of brain activity and disease spreading patterns [201, 202]. Here, we provide proof of concept, with our heterodimer-oscillator model, that neuronal activity may play a mechanistic role in the spreading of τP seen in Alzheimer's disease staging.

We simulate the spreading of tau (omitting Aβ) on the 83-node Budapest Reference Connectome [203]—in which the simulation initially follows the canonical Braak staging pattern—and gradually increase the effect that neuronal activity has on spreading, which is achieved by increasing δ. To simulate the natural progression of Alzheimer's disease, we only initialize a nonzero concentration of toxic protein in the entorhinal cortex (Braak stage I).

To visualize the Alzheimer's simulations more easily, we investigate metrics averaged over the regions per their Braak staging. As shown in Fig. 5.10a, we see that neuronal activity induces symmetry breaking in asymptotic toxic protein concentrations (asymptotic refers here to the end of disease simulation). Different regions become more susceptible to tau pathology than others due to the activity-dependence of tau spreading. Furthermore, in Fig. 5.10b, we see that the arrival time of the Braak staging is affected by neuronal activity, although the ordering of the Braak stages is quite robust. The tau spreading model achieves the correct Braak staging even without activity-dependent spreading. Including neuronal activity swaps the order of Braak stage II and III for higher values of δ, but the ordering remains unaffected otherwise.

However, the inclusion of activity-dependent spreading has little effect on the neuronal dynamics, as evidenced in Fig. 5.10c–d. In Fig. 5.10c, we show the asymptotic average frequency of the neural oscillators. As τP spreads, it decreases the intrinsic frequencies of the oscillators. However, the amount of frequency slowing caused by τP spreading is not impacted by its activity dependence. As such, there is little change in asymptotic frequencies due to the parameter δ. The average phase coherence of the neural oscillators is not affected either by the inclusion of activity dependence, as shown in Fig. 5.10d. Therefore, we find that the spreading dynamics is affected by its dependence on neuronal dynamics, while the neuronal dynamics themselves appear mostly unaffected.

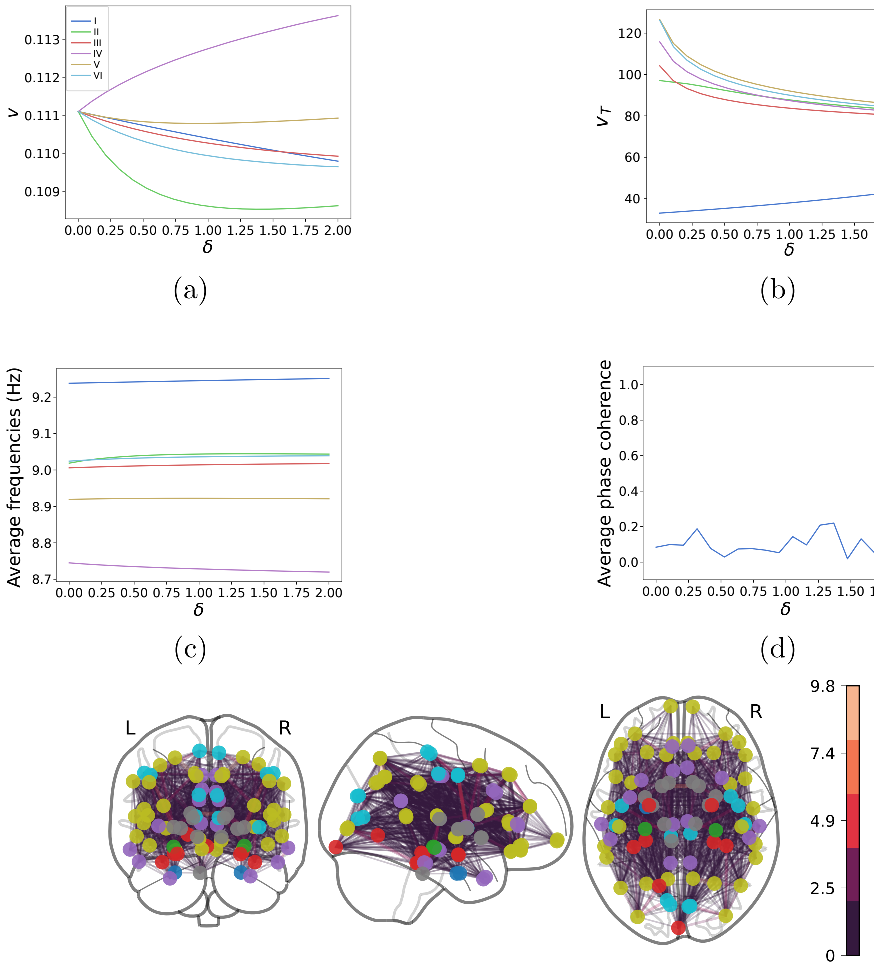

(a) (b)

(c) (d)

(e)

Figure 5.10: Simulations of toxic tau spreading across an 83-node human connectome showing the asymptotic (steady-state) behavior of the system as a function of δ (the effect activity has on spreading). Parameters are $\rho = 0.001, k_0 = 1, k_1 = 1, k_3 = 0.9, k_2 = 1, \epsilon = 0.01, K = 0.1, c = 10$. The natural frequencies, ω_i, are drawn from a normal distribution with a mean 10 and standard deviation of 0.5. Nodes are initialized with $u_i = 1$ and $v_i = 0$, apart from the entorhinal cortices, which are initialized with $u_i = 1$ and $v_i = 0.1$ (nonzero toxic concentration). *(a)* Average asymptotic amount of tau species in each Braak stage. *(b)* Average time for regions in different Braak stages to become infected with τP. *(c)* Asymptotic average frequencies of the oscillators at the end of the slow-time simulation. *(d)* Average global phase-coherence over the entire slow-time spreading simulation. *(e)* Graph of the brain network with edges colored according to their weight. Nodes that are not part of any Braak stage are colored gray.

5.5 Conclusion

In the previous chapter, we modeled the spreading of toxic proteins during Alzheimer's disease and its impact on neuronal dynamics. In this chapter, we formulated a model integrating the effect neuronal dynamics have on protein spreading. A key difference between this approach and the preceding chapter is the spatial scale and the absence of a damage variable. In this chapter, the neural oscillators are interpreted not as brain regions but as neurons. This is because the experimental work the model was based on was performed on *in vitro* neurons. Damage variables were introduced in the preceding chapter primarily to transform the toxic protein concentration into a variable ranging from 0 to 1. As we were most interested in understanding the dynamics of introducing activity-dependent spreading, we omitted the damage variable for simplicity's sake. However, this means that we need further assumptions in this chapter, such as assuming that the toxic protein never grows so large that it causes the frequencies of the oscillators to reach negative values.

The formulation of the heterodimer-oscillator was primarily motivated by the case of Alzheimer's disease and other neurodegenerative diseases. The impact of neuronal activity on pathological protein spreading patterns is becoming increasingly clear and provokes the need for mechanistic, mathematical modeling of the bidirectional relationship between disease progression and neuronal activity. Building our model from mechanistic principles from the neuroscientific literature, we provide a simple mathematical model of this relationship. Notably, the heterodimer-oscillator provides falsifiable hypotheses on the nature of prion-like spreading; protein spreading patterns follow a neuronal activity gradient, and more extreme gradients push the brain towards a pathological state. We have also demonstrated that the heterodimer-oscillator indeed alters the regional vulnerability to τP infection when simulated on a human brain connectome. It is not uncommon for patients to deviate from the stereotypical Braak staging patterns, and the heterodimer-oscillator may also provide a mechanistic explanation for such aberrations. However, we focused on asymptotic behavior when analyzing the spread of τP on the connectome, which may have missed transient phenomena induced by the multiple-timescale dynamics. Future work is needed to establish the predictive power and ramifications of the heterodimer-oscillator in applications to neurodegenerative disease modeling.

In the preceding couple of chapters, we have discussed the relationship between disease and neuronal activity. However, we have not yet discussed how diseases change neuronal activity in quantitative terms. In the following chapter, we will see how mathematical modeling can reveal abnormalities in neuronal activity in brain cancer patients by fitting a whole-brain model to clinical data.

Chapter 6

A whole-brain model reveals tumor-induced alterations to neuronal dynamics in glioma patients

6.1 Overview

One of the ultimate goals of neuroscience is to understand and control neuronal dynamics across scales, from the individual neuron to the whole brain. On the larger end of the scale, researchers have developed whole-brain models to understand brain activity. These models are mainly used to understand functional connectivity patterns (correlations in brain waves between brain regions). As discussed in Section 2.10, functional connectivity is increased in the alpha band in glioma patients, which may be linked to the excretion of excitatory neurotransmitters by tumor cells. However, the precise mechanism behind abnormalities in functional connectivity in glioma patients is disputed, and how tumors impact neuronal activity is not fully understood.

In this chapter, we use a whole-brain model of Hopf oscillators to explain the functional connectivity differences in glioma patients compared to healthy controls, as measured by MEG. We do so by identifying the optimal parameterization of the whole-brain model to empirical phase-lag index connectivity computed from MEG data of glioma patients and healthy controls. We find that the goodness-of-fit of the Hopf whole-brain model is invariant under a particular scaling law for the parameters. This scaling law demonstrates that the phase dynamics is almost solely determined by the *normalized coupling strength*, defined as the ratio of interregional coupling and intraregional excitability. Furthermore, we find that the optimal normalized coupling strength is higher in the glioma cohort than in the controls both on an individual and population-based level. We also show that the tumor regions generally induce increases in normalized coupling strength, though there is considerable variability between patients. In summary, we find that the ratio of interregional and intraregional dynamics uniquely determines the phase dynamics of the Hopf whole-brain model and that tumors increase the relative contribution of interregional dynamics in glioma patients. This chapter is based on the preprint by Alexandersen *et al.* [26].

6.2 Simulating functional connectivity with a whole-brain model

6.2.1 Computation of the phase-lag index as a measure of functional connectivity

MEG data was gathered and preprocessed for a healthy (33 subjects) and glioma (10 patients) cohort. A structural connectome was constructed by averaging individual connectomes of the healthy cohort, which will be used for all the whole-brain simulations in this chapter. For a thorough discussion of the data processing and gathering see Appendix B.

Here, we use the *phase-lag index* (PLI) as a measure of functional connectivity [57]. PLI is a measure of the average asymmetry in pairwise phase differences of oscillatory MEG signals from different brain regions and ranges from 0 (symmetry) to 1 (asymmetry) for each pair of regions. Though we already covered the basic premise of PLI in Section 2.4.3, it will be repeated here for ease of reading.

The phase-lag index is computed in the same way for each cohort. For each cohort, we have S subjects. For each subject $s \in \{1, \ldots, S\}$, we have E_s epochs, each consisting of a $N \times M$ matrix, where N is the number of brain regions and M is the number of time points. We denote each matrix by $\hat{x}_{s,e} \in \mathbb{R}^{N \times M}$ with dimensions N and M, where $e \in \{1, \ldots, E_s\}$ denotes the epoch and $s \in \{1, \ldots, S\}$ denotes the subject.

For processing, we apply a Butterworth filter to bandpass the signal into the alpha frequency band at 8–12 Hz. Thus, the Butterworth filter is a function $F : \mathbb{R}^{N \times M} \rightarrow \mathbb{R}^{N \times M}$ that can be applied to each epoch. After bandpassing the data, we find the angle of its Hilbert transform $\Theta : \mathbb{R}^{N \times M} \rightarrow \mathbb{R}^{N \times M}$. Next, we compute the phase-lag index connectivity. That is, we apply a function $P : \mathbb{R}^{N \times M} \rightarrow \mathbb{R}^{N \times N}$ to the data to construct a N-by-N, symmetric functional connectivity matrix. This phase-lag index transformation is given explicitly by

$$P(\theta)_{ij} = |\langle \mathrm{sign}(\sin(\theta_i - \theta_j)) \rangle_t| \quad \text{for } i = 1, \dots, N,\ j = 1, \dots, N, \tag{6.1}$$

where $\langle \ \cdot \rangle_t$ is the time average. We apply this process to compute the PLI for each matrix $\hat{x}_{s,e}$:

$$P(\hat{x}_{s,e}) = P(\Theta(F(\hat{x}_{s,e}))) \tag{6.2}$$

and compute the average experimental phase-lag index matrix for the entire cohort as

$$P^{\mathrm{exp}} = \frac{1}{S} \sum_{s=1}^{S} \frac{1}{E_s} \sum_{e=1}^{E_s} P(\hat{x}_{s,e}). \tag{6.3}$$

Experimental PLI matrices are here averaged over epochs and, at times, over individuals. This averaging leads to a level of background noise in the matrices, which is lacking in our computational model. As such, direct comparisons between experimental and simulated PLI matrices may lead to nonsensical optimal model parameters. This is because the model may optimize its parameters to better fit the background noise rather than the structure of the functional connectivity patterns. Thresholding the experimental PLI matrices provides optimal model parameters that more faithfully capture the empirical functional connectivity patterns. The experimental PLI matrices are thus thresholded to ease the comparison with the noiseless whole-brain model. Thresholding the PLI matrix at a certain percentage $X\%$ means setting all elements in the lower $X\%$ percent to zero as ordered per magnitude.

6.2.2 The Hopf whole-brain model

We use a whole-brain model consisting of a network of Hopf oscillators. More specifically, we use the Hopf normal form (see Section 3.1.2) on a reconstruction of the physical human brain network, where the oscillators interact through a sigmoidal function without delays. As such, each Hopf oscillator denotes a brain region, where the links of the network denote axonal bundles connecting a pair of brain regions.

The human structural connectome network is, as previously, represented by the adjacency matrix $\mathbf{W} = (W_{ij})$. The state of the Hopf oscillators, $z_i \in \mathbb{C}$, are complex variables having real and complex parts $z_i = x_i + \mathrm{i} y_i$, where $\mathrm{i} = \sqrt{-1}$. The Hopf oscillators are coupled through their real parts x_i, and subsequent analysis of simulations will only consider the real part and not the imaginary part. Indeed, the real part x_i represents the simulated MEG signals, while the imaginary part y_i can be thought of as a hidden variable needed to produce the necessary oscillatory dynamics.

The Hopf whole-brain model for a network $\mathbf{W}$ with N regions evolves through the following system of complex ordinary differential equations

$$\dot{z}_i = \mathcal{F}(z_i; \lambda, \omega_i) + K \tanh\left(C \sum_{j=1}^{N} W_{ij} x_j\right), \qquad i = 1, \ldots, N, \tag{6.4}$$

with

$$\mathcal{F}(z_i; \lambda, \omega_i) = z_i \left(\lambda + \mathrm{i}\omega_i - |z_i^2|\right). \tag{6.5}$$

Here, $K \geq 0$ is the *global coupling strength*, $\lambda \in \mathbb{R}$ is the *global excitability parameter* (called the Hopf bifurcation parameter in previous chapters), $\omega_i > 0$ is the local natural frequency of oscillation, and $C \geq 0$ is the *global scaling* of the structural connectome.

Each natural frequency ω_i is parameterized from the healthy control MEG data using the frequency peaks found for each brain region (see Appendix B). Thus, the remaining free parameters are the coupling strength K, the excitability λ, and the structural connectivity scaling C.

6.2.3 Fitting whole-brain model to experimental functional connectivity

To assess the goodness-of-fit of the Hopf whole-brain model to experimental MEG data, we compare the functional connectivity of the simulated and experimental signals. The objective (cost) function we use to assess the goodness-of-fit is the Pearson correlation of the time-averaged pairwise phase-lag indices [169]. We will now describe the settings of whole-brain model simulations, the processing of the simulated data, and the computation of the objective function.

We simulate the Hopf whole-brain model for 14.5 seconds and discard the first second of simulations to account for transient dynamics induced by the initial conditions. We save the simulated data with a sampling frequency of 1250 Hz. As such, the simulated data has the same length and sampling frequency as the experimental MEG data. The simulations are performed with the RK45 method (using the JiTCODE module for Python) with an absolute tolerance of 10^{-6} and a relative tolerance of 10^{-3}.

As mentioned, we interpret the real part of the Hopf oscillator variables x_i as MEG signal and process it in the same manner as the experimental MEG signal. That is, we bandpass the signal into the alpha frequency band (8-12Hz) using a Butterworth filter (denoted by the function F) and subsequently apply the Hilbert transform to find the angles of the oscillators (denoted by the function Θ). We then compute the pairwise time-averaged phase-lag index of the processed simulated signal and compute the Pearson correlation of the simulated PLI matrix and the experimental PLI matrix.

Let $x \in \mathbb{R}^{N\times M}$ denote the simulated time series of N regions over M time points. Note that x is a function of the parameters and the initial conditions $z(0) = z_0$ of the whole-brain model. As such, the simulated phase-lag index is $P^{\text{sim}} = P(\Theta(F(x(K, \lambda, C, x_0)))$, with P, F, and Θ defined above. Remembering that P^{exp} denotes the experimental MEG PLI matrix averaged over epochs and subjects, the objective function is

$$f(K, \lambda, C, z_0; P^{\text{exp}}) = \frac{\left(\sum_{ij}^{N} P_{ij}^{\text{sim}} - \langle P^{\text{sim}}\rangle\right)\left(\sum_{ij}^{N} P_{ij}^{\text{exp}} - \langle P^{\text{exp}}\rangle\right)}{\sqrt{\sum_{ij}^{N}\left(P_{ij}^{\text{sim}} - \langle P^{\text{sim}}\rangle\right)^2\left(P_{ij}^{\text{exp}} - \langle P^{\text{exp}}\rangle\right)^2}}, \tag{6.6}$$

where $\langle\cdot\rangle$ denotes the average over all matrix entries. As the objective function depends on the initial conditions z_0, we average the objective function over several runs with random initial conditions. For random initial conditions, each oscillator's initial state z_i for $i = 1, \ldots, N$ is a random point in the unit disk $|z_i| \leq 1$ picked with uniform probability.

In Section 6.5, we investigate the impact of tumor regions on the dynamics of the whole-brain model in individual patients and clusters of tumor regions. We do so by performing a *pseudo-craniotomy*, in which we remove the rows and columns corresponding to the tumor brain regions from both P^{sim} and P^{exp}. In effect, the objective function ignores the tumor regions, resulting in a change in optimal model parameters.

6.3 Phase correlations emerge from the competition between inter- and intra-regional dynamics

To assess the goodness-of-fit for the Hopf whole-brain model, we compare simulations to experimental data. Specifically, we compute the phase-lag index of the simulated signals of the whole-brain model (example shown in Fig. 6.1a) and compare them with the averaged experimental phase-lag index of a healthy control group (experimental PLI found in Fig. 6.1c). The goodness-of-fit is defined as the Pearson correlation between the simulated and experimental pairwise phase-lag indices.

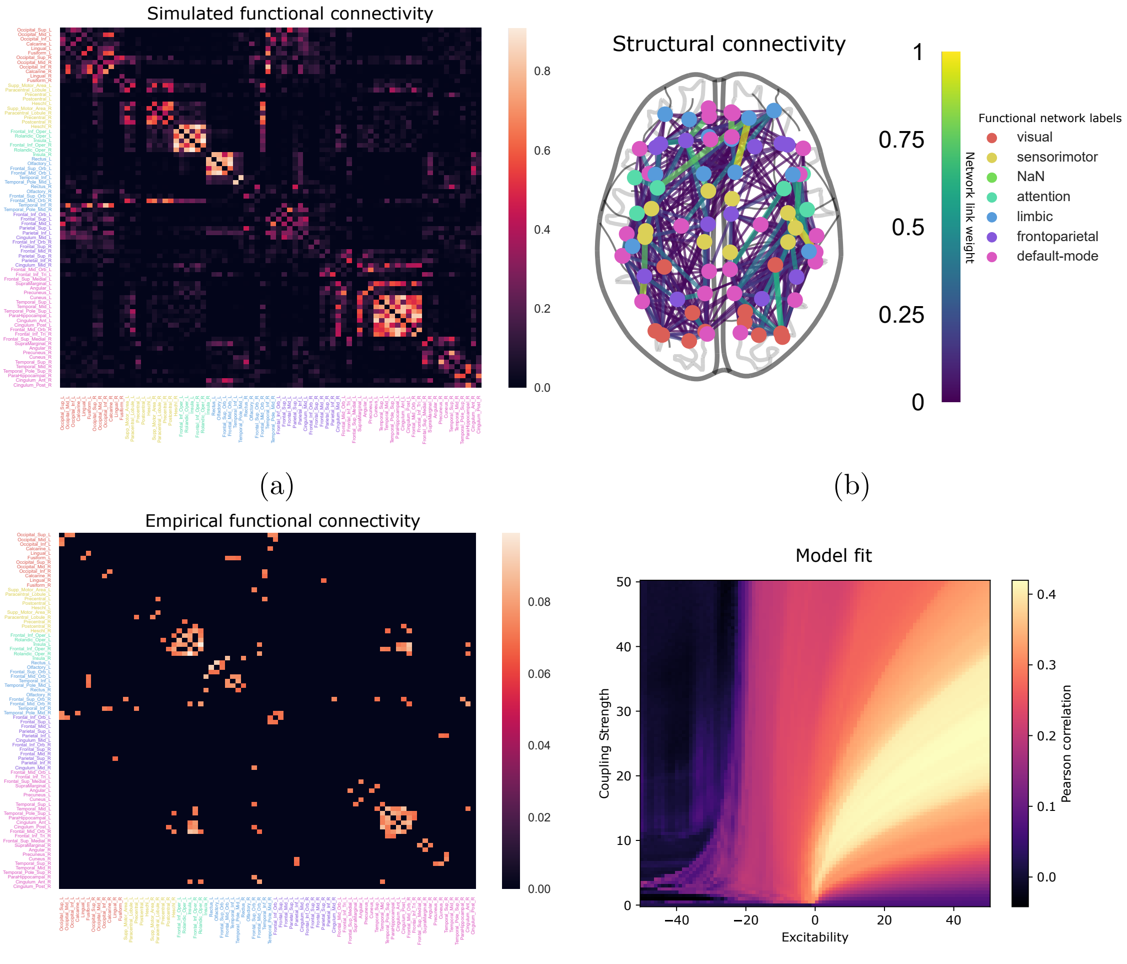

(a) (b)

(c) (d)

Figure 6.1: *(a,c)* An example of synthetic (simulated) phase-lag index from a Hopf whole-brain model and experimental PLI averaged over 33 healthy subjects from the control group. The name of each brain region is labeled and colored according to canonical functional networks (see legend to the upper right). *(b)* The weighted physical connectome averaged over the control group. Each node is colored similarly to the functional connectivity matrices. *(d)* The goodness-of-fit of the Hopf whole-brain model with respect to the coupling strength and excitability parameter. Each pixel shows the Pearson correlation between the simulated and experimental (control group average) phase-lag indices averaged over 500 whole-brain simulations with random initial conditions.

The experimental PLI is noisy and is thus thresholded to make it comparable to the noiseless, simulated PLI. Figure C.3 in Appendix C shows the effect of thresholding on the average control PLI. We threshold the experimental, averaged PLI at the optimal threshold providing the best fit to the simulated data (see Fig. C.4 in Appendix C). However, we note that the following results hold for a wide range of threshold values, as demonstrated in Appendix C. In particular, the results have also been reproduced by thresholding the experimental PLI by their median value so that all elements of the PLI matrix below the median value are set to zero (see Fig. C.6).

The structural connectivity used to provide the network of the Hopf whole-brain network is the averaged dMRI connectome of the healthy control cohort (see Fig.6.1b and Appendix B). The structural connectivity is unitless, and hence, we use a scaling constant C as a free parameter. We found that the goodness-of-fit of the Hopf whole-brain model is not sensitive to structural connectivity scaling (see Fig. C.1 in Appendix C). As long as the scaling parameter is large enough, it has no impact on the goodness-of-fit. As such, we parameterize the scaling at $C = 20$ and keep it this way for the remainder of this chapter. The natural frequencies of the individual brain regions must also be parameterized in the Hopf whole-brain model. We set the natural frequencies equal to the average peak frequencies of the experimental MEG signal of the healthy cohort. As such, the only remaining parameters of the Hopf whole-brain model are the global coupling strength K and the global excitability parameter λ.

We perform a two-dimensional grid search over the coupling strength and excitability parameter to find the optimal parameterization of the Hopf whole-brain model to average control phase-lag index connectivity as shown in Fig. 6.1d. Contrary to previous modeling assumptions, we find that the optimal fit to functional connectivity occurs at positive excitability parameter values ($\lambda > 0$). We also see that there are contour lines over the coupling strength and positive excitability parameters where the goodness-of-fit does not change. This suggests that the phase dynamics (as measured by PLI) are invariant—to some degree—under some transformation for positive excitability values.

By scaling the variables of the Hopf whole-brain model by $\tilde{x}_i = \sqrt{\lambda} x_i, \tilde{y}_i = \sqrt{\lambda} y_i$ for $i = 1 \dots N$, we obtain the following equivalent system

$$\frac{d\tilde{x}_i}{dt} = \lambda \tilde{x}_i - \omega_i \tilde{y}_i - \lambda \tilde{x}_i (\tilde{x}_i^2 + \tilde{y}_i^2) + \frac{K}{\sqrt{\lambda}} \tanh \left(\sqrt{\lambda} \sum_{j=1}^{N} W_{ij} \tilde{x}_j \right), \tag{6.7a}$$

$$\frac{d\tilde{y}_i}{dt} = \lambda \tilde{y}_i + \omega_i \tilde{x}_i - \lambda \tilde{y}_i (\tilde{x}_i^2 + \tilde{y}_i^2), \tag{6.7b}$$

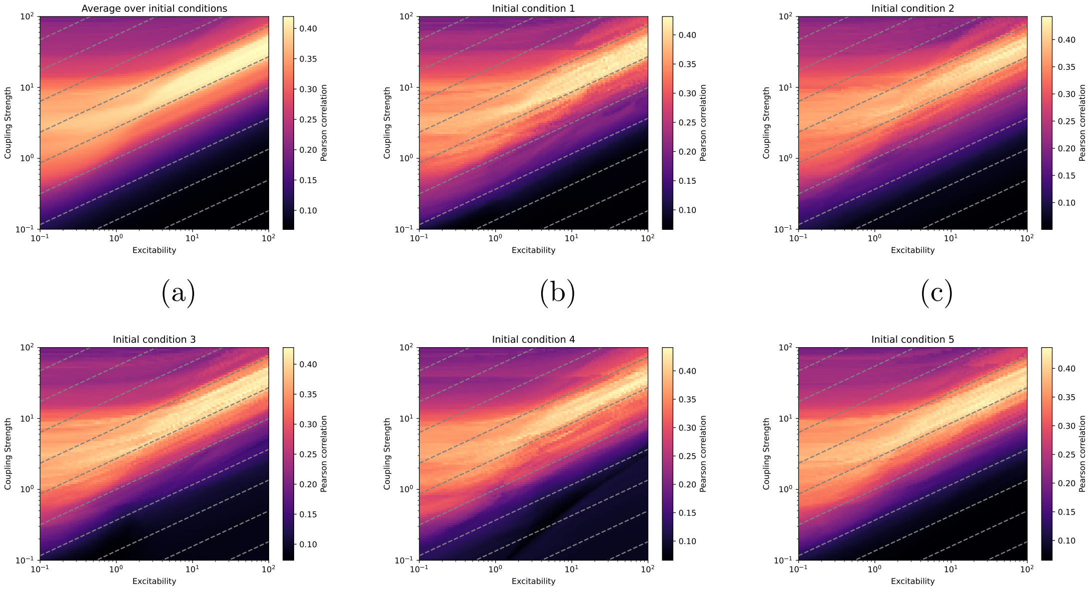

(a) (b) (c)

(d) (e) (f)

Figure 6.2: Parameter grid-search on logarithmic axes for a Hopf whole-brain model for individual initial conditions (b–f) and averaged over 300 initial conditions (a). The grey stippled lines represent a square-root scaling of the coupling strength with respect to excitability. That is, the grey stippled lines show $K = k\sqrt{\lambda}$ for different k. Each pixel shows the Pearson correlation between the simulated and experimental (average, control group) phase-lag index connectivity. The grids indicate that the Pearson correlation is unchanged as the coupling strength scales with the square root of excitability, such that $K \sim \sqrt{\lambda}$.

for $\lambda > 0$. The scaled system above is equivalent to a system coupling Hopf oscillators with a stable limit cycle of radius 1 with a modified coupling constant $K/\sqrt{\lambda}$. Additionally, the excitability parameter λ does not scale the radius of the limit cycle as in the original system. Instead, it is the timescale of the amplitude dynamics. As such, we expect the phase dynamics of the Hopf whole-brain model to be determined mainly by the ratio $K/\sqrt{\lambda}$ and not by the coupling strength and excitability independently. We see that this is indeed the case when computing the goodness-of-fit over coupling strength and excitability on a log-log grid (see Fig. 6.2), showing that the goodness-of-fit is invariant under $K \sim \sqrt{\lambda}$. The coupling strength is a measure of interregional (global) coupling, whereas the excitability parameter is a measure of intraregional (local) excitability. As such, it is the competition between interregional and intraregional dynamics that determines the phase correlations in the Hopf whole-brain model. We will refer to the ratio $k = K/\sqrt{\lambda}$ as the *normalized coupling strength*.

6.4 Whole-brain modeling reveals higher interregional coupling in glioma cohort

We have now determined that the normalized coupling strength controls the phase dynamics of the Hopf whole-brain model, and we can investigate whether the normalized coupling strength differs between glioma patients and healthy controls. As before, we perform two-dimensional grid searches over the coupling and excitability parameters, computing the goodness-of-fit to the averaged PLI of the healthy control group and the glioma group, respectively (see Fig. 6.3b–c). We then find the optimal coupling strength per excitability parameter for both cohorts and compute the mean and standard deviation of the optimal coupling strength over randomized initial conditions for the whole-brain simulations (see Fig. 6.3a, solid lines).

We find that the glioma cohort has a higher coupling strength over the excitability parameters, suggesting that their *normalized coupling strength* is higher. To confirm this, we find the optimal fit for the mean optimal coupling strength per the square root of the excitability parameter through least squares regression. That is, we find the scaling k providing the best fit for $K = k\sqrt{\lambda}$ for the mean of the two cohorts. As shown in Fig. 6.3a, the regression provides an excellent fit for larger excitability values and produces a higher normalized coupling strength for the glioma cohort compared to the control cohort. The fitted regression lines of the normalized coupling strength have been plotted on top of the 2-dimensional grid searches in Figure 6.3b–c.

To further investigate the differences in functional connectivity between the control and glioma cohorts, we compute the distribution of optimal whole-brain parameters over the initial conditions for fixed excitability values. For 1000 initial conditions, we compute the difference in optimal coupling strengths between the glioma and control cohorts for five different excitability parameter values and plot the resulting distributions in Figure 6.4a–e. Interestingly, there is considerable variation between initial conditions. In particular, there seem to be two peaks in the distributions: one at zero difference and one at a positive difference. The bimodality disappears once all the optimal coupling strengths from the different excitability values are pooled into one distribution, as shown in Figure 6.4f. Many initial conditions do not lead to different optima between the glioma and control cohorts. However, those that *do* exhibit differences have a bias towards higher coupling strength in the glioma cohort.

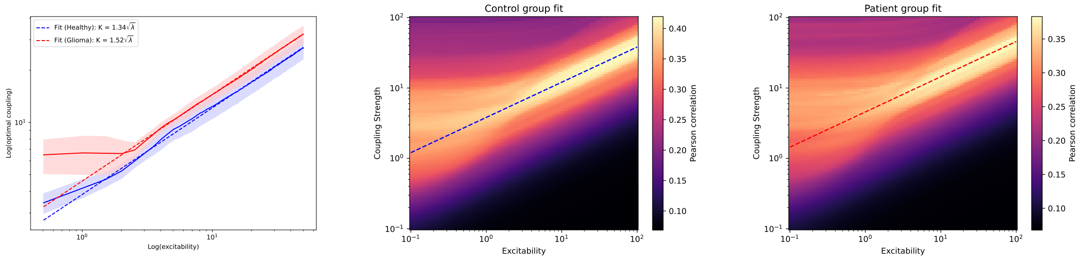

(a) (b) (c)

Figure 6.3: Optimal parameter fits of the Hopf whole-brain model to experimental phase-lag index connectivity for the control (blue) and glioma (red) cohort average. The optimal normalized coupling strength is fitted by regression (stippled line) and is the slope of the average optimal coupling strength per excitability parameter (solid line). Notice that all plots are in log-log coordinates. *(a)* The average (line) and standard deviation (shaded region) of optimal excitability and coupling strength over 1000 initial conditions. The average optimal coupling strength is fitted to a square-root dependence on the excitability (Hopf) parameter per the healthy (blue) and glioma (red) cohort. The regression fits the average optimal parameters well. *(b,c)* The fitted line (regression) of the optimal ratio between coupling strength and excitability parameters is shown on the parameter grid search for the healthy and glioma cohorts.

6.5 Tumors contribute to higher interregional coupling in glioma

We have established that the normalized coupling strength (interregional versus intraregional dynamics) is higher in the glioma-cohort average than in the controls. However, we will see that individual patients also exhibit higher normalized coupling strengths. For fixed excitability values, we find the optimal coupling strength when fitting simulated PLI to the *patient-specific* PLI (thresholded by their median value). We then compute the difference between these optimal coupling strengths to that of the average control group over different initial conditions, as shown in Figure 6.5 normalized by the standard deviation of the average control over ICs. As demonstrated in the previous section, considerable variations between initial conditions exist. Nevertheless, we observe a general trend in which patients individually have higher coupling strengths, with some patients exhibiting increases in coupling strength several standard deviations above the control average.

To probe the role of tumors in shaping functional connectivity alterations, we perform a *pseudo-craniotomy* in which we remove the tumor regions of the particular patient from the goodness-of-fit evaluation when finding optimal model parameters. The regions themselves are not removed from the model, as such a virtual

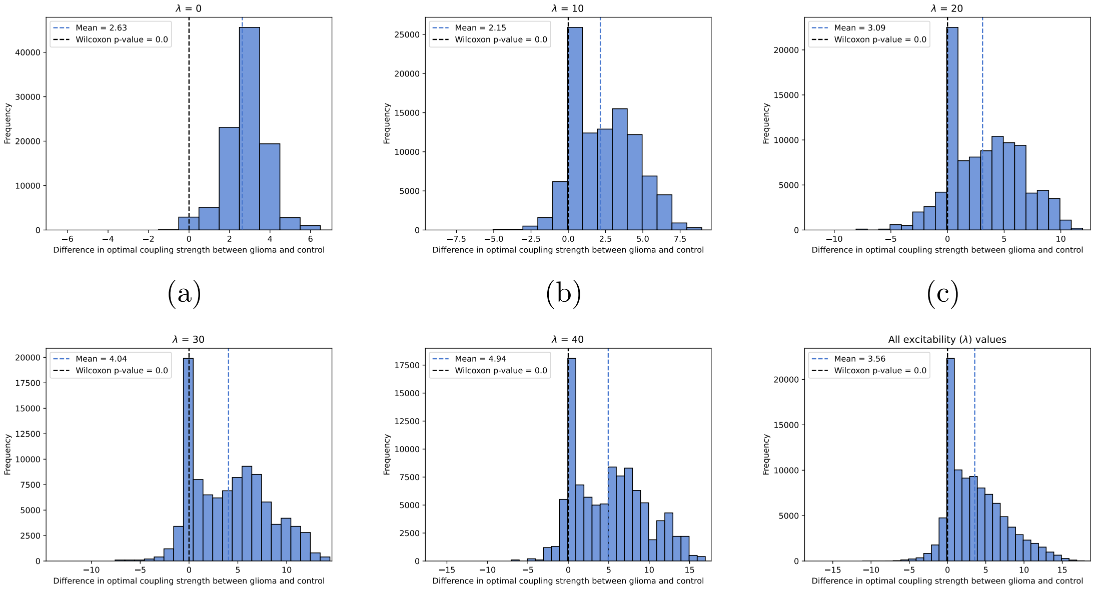

(a) (b) (c)

(d) (e) (f)

Figure 6.4: Distributions of the difference in optimal coupling strength between the healthy and glioma cohort for fixed excitability parameters over 1000 initial conditions for the Hopf whole-brain model. The black stippled line illustrates where there is zero difference between the cohorts, and the blue stippled line shows the mean of the distributions. *(a-e)* For different excitability (Hopf) parameter values, we find the difference in optimal coupling strength between the averaged control and glioma cohort when optimized for the best fit to experimental phase-lag index connectivity. The difference is positive when the glioma cohort has a higher optimal coupling strength and negative when the glioma cohort has a lower optimal coupling strength. The distributions arise from 1000 simulations of the Hopf whole-brain model for random initial conditions. *(f)* In this histogram, all the optimal coupling strengths for all the excitability parameters (ranging from 0 to 50 with a step of 0.1) are pooled together into one larger distribution. For all distributions, the Wilcoxon rank-sum test was performed, for which all were highly significant (to orders smaller than -100).

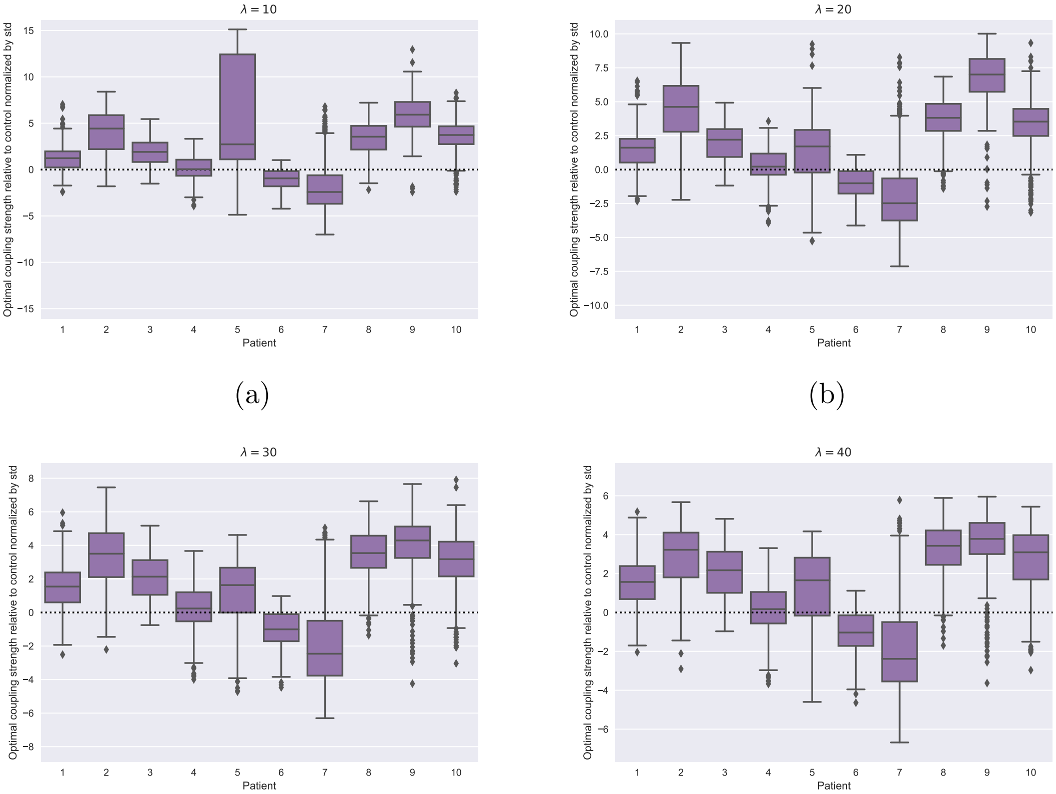

(a)

(b)

(c)

(d)

Figure 6.5: The difference in coupling strength found for individual patients and the healthy control at different excitability parameter values λ. The box plots show the difference between optimal coupling strengths per patients' individual phase-lag index compared to the optimal coupling strength found per the healthy control, averaged over 500 initial conditions for the Hopf whole-brain model. The values have been normalized by the standard deviation in the average control over initial conditions. A box distributed towards positive values indicates that the patients' optimal coupling strength is higher than the optimal coupling strength for the healthy control average.

procedure would be too disruptive; we are interested in the effect tumors have on global dynamics, not in how dynamics change once they are surgically removed. In the pseudo-craniotomy, the objective function (Pearson correlation between simulated and empirical functional connectivity) ignores the tumor regions when identifying optimal parameters. If the optimal coupling strength is lower after pseudo-craniotomy, it means that the tumor regions of that patient contribute to a pathologically high coupling strength.

The tumor regions of the patients in the glioma cohort are shown in Figure 6.6a–j with their position in the physical structural connectome. For each patient, we first find the optimal parameters with respect to their complete, individual PLI connectome. We then recompute the optimal parameters with respect to their individual PLI connectome after pseudo-craniotomy, that is, where the rows and columns of the tumor regions (all correlations involving the tumor regions) have been removed. The change in optimal parameters reflects the impact the regions have on the goodness-of-fit of the whole-brain model and, by extension, their impact on the overall whole-brain dynamics.

We also identify three clusters of tumor regions by the K-means clustering algorithm, as shown in Figure 6.6k & f. In addition to investigating the tumor regions impact on global brain dynamics per patient, we also investigate the impact of the clusters—as well as the union of tumors across all patients—on the overall global dynamics, where we now fit the optimal parameters to the average PLI of the glioma cohort.

Setting the excitability parameter at $\lambda = 40$, we compute the optimal coupling strength before and after pseudo-craniotomy for each patient and tumor cluster (see Fig. 6.7). The goodness-of-fit is computed with patient-specific PLIs for each patient and averaged PLI (across patients) for each cluster. For each simulation, we perform the same patient-specific pseudo-craniotomy to the average healthy control (fitting to the average healthy PLI). To keep the control and patient fit as comparable as possible, we use the average healthy structural connectome for both control and patient-specific simulations. Simulations are repeated over 500 initial conditions with the resulting distributions shown in Figure 6.7a & c. There is considerable variation between patients, with some showing a clear reduction in coupling strength, whereas others are difficult to distinguish from their respective control. In Figure 6.7c–d, we show the distributions of the differences in the optimal coupling strength after pseudo-craniotomy for each patient and their control. Wilcoxon rank sum tests were computed for each patient/cluster/union showing highly significant results. Patients

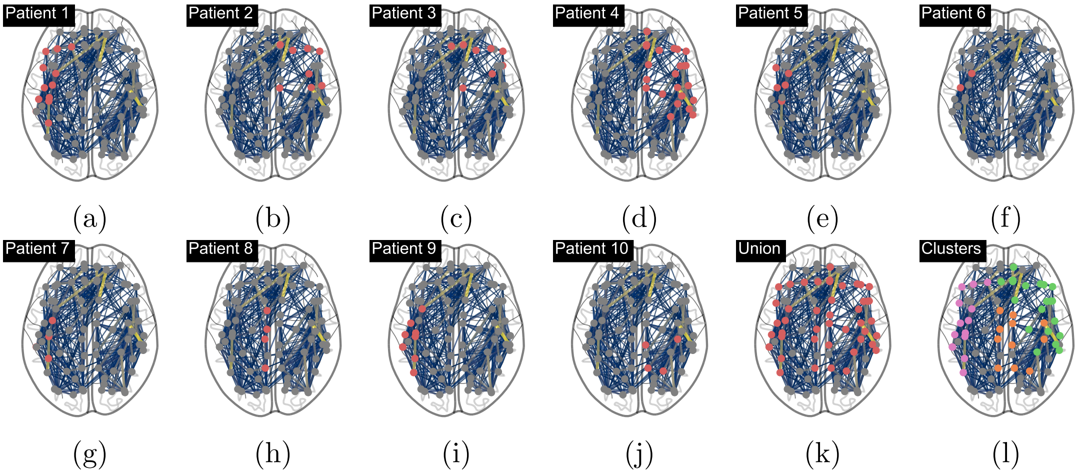

(a) (b) (c) (d) (e) (f)

(g) (h) (i) (j) (k) (l)

Figure 6.6: Pseudo-craniotomies were performed to assess the contribution of tumors to the whole-brain model dynamics. Here, we show the locations of the tumor regions on top of the average structural connectivity. We also found three clusters (Kmeans clustering algorithm) of tumor regions, which will be used in subsequent analyses. The union of all tumor regions will also be used.

show either no change or a decrease in coupling strength after pseudo-craniotomy. We reiterate that decreases in coupling strength after pseudo-craniotomy correspond to the tumors contributing to higher coupling strengths.

To further assess general changes caused by a pseudo-craniotomy, we pool the changes in optimal coupling (relative to the change in control) for the patients and clusters, as seen in Figure 6.7e–f. For both patients and clusters, the distributions show a bias towards lower coupling strengths as induced by the pseudo-craniotomy. The Wilcoxon Rank Sum test was computed for the pooled patient and cluster distribution with a highly significant result, indicating a trend towards lower coupling strengths per the means of the distributions. Effectively, there is a general trend indicating that tumors contribute to higher coupling strengths, though, as expected, there is considerable variability between patients.

6.6 Conclusion

We found that the optimal parameter fit of the Hopf whole-brain model to phase-based functional connectivity is invariant when $K \sim \sqrt{\lambda}$ for $\lambda \geq 0$. That is, the phase correlations of the simulated signal remain unchanged as the coupling strength scales with the square root of the excitability (Hopf) parameter. This is intuitive, as for isolated Hopf oscillators, the radius of the stable limit cycle arising at the Hopf bifurcation (occurring at $\lambda = 0$) is given by $|z| = \sqrt{\lambda}$. Mathematically speaking,

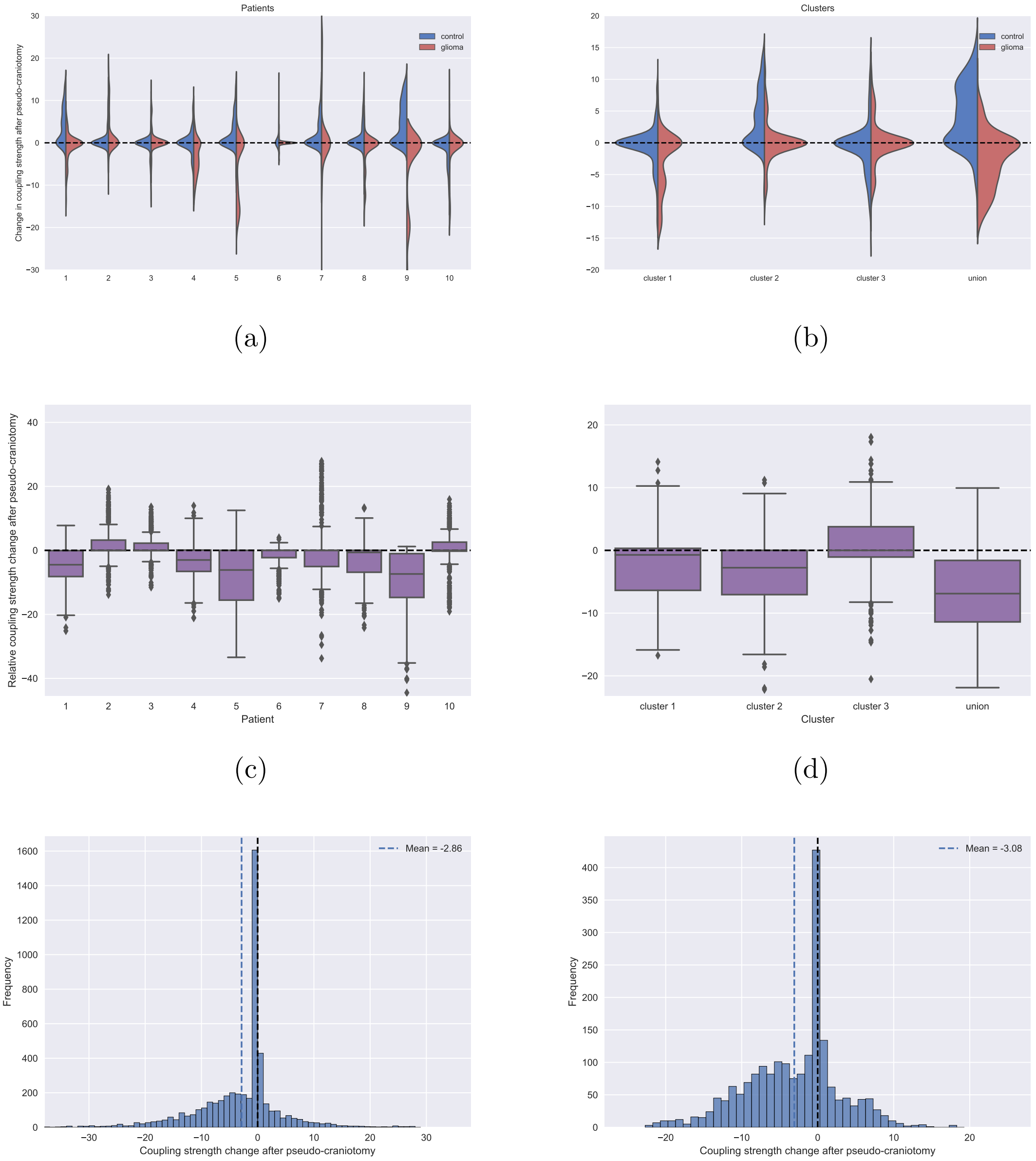

(a) (b) (c) (d) (e) (f)

Figure 6.7: Pseudo-craniotomies were performed to assess the impact of tumors on brain dynamics. The excitability parameter was kept constant ($\lambda = 40$) for over 500 initial conditions for the Hopf whole-brain model per patient (left column) and per tumor cluster (right column). *(a,b)* Violin plots of the change in optimal coupling strength after pseudo-craniotomy (red - patient, blue - control). *(c,d)* The difference in the change after pseudo-craniotomy between the patients and healthy average control. *(e,f)* A histogram showing the distribution of changes in optimal coupling strength across all patients and initial conditions relative to the change in the average healthy control.

$K \sim \sqrt{\lambda}$ tells us that the phase dynamics does not change as the ratio between the coupling strength (interregional dynamics) and the radius of the self-sustained, local oscillations (intraregional dynamics) are constant. Interestingly, however, we find the optimal fit to functional connectivity at positive excitability parameters.

Contrary to common modeling assumptions [156, 204, 205], we did not find that the optimal parameter fit of the whole-brain model was close to criticality, in the sense that the local dynamics is *not* close to the Hopf bifurcation point ($\lambda = 0$). Indeed, we found the optimal fit to be arbitrary as long as the model was parameterized beyond criticality, with $K \sim \sqrt{\lambda}$ for $\lambda \geq 0$. To be more precise, in our optimal fit, the individual local dynamics sustains oscillations independently of network interactions (the network interactions still affect the oscillations but are not necessary to produce oscillatory signals locally). In most modeling studies—including our simulations in Chapter 4—the parameters are set so that the individual oscillators can only sustain oscillations with the aid of network interactions. That is, the parameters are set close to a critical (bifurcation) point, which in our case would be $\lambda \leq 0$. This assumption ($\lambda \leq 0$) is based on the hypothesis that the brain is a dynamical system operating at criticality [206]. However, in our case, we have shown that the static, time-averaged functional connectivity—as measured by phase correlations—is better captured beyond criticality as defined by the Hopf bifurcation. Nonetheless, when considering the changes in phase correlation as a function of coupling strength, there is another sense of criticality as viewed through the lens of phase transition [207]. For example, for low coupling strengths, there will be no correlation patterns. However, patterns will arise as the coupling strength is increased, with an optimal coupling strength at intermediary values. In recent years, dynamic functional connectivity has been of growing interest as it reveals the temporal evolution of functional connectivity [208]. It seems likely that parameterizing the bifurcation parameter far beyond criticality $\lambda \gg 0$ will *not* reproduce the switching between correlation patterns as observed experimentally with dynamic functional connectivity metrics.

In this chapter, we showed that the phase dynamics of the Hopf whole-brain model is primarily determined by the ratio of interregional and intraregional dynamics, where the ratio is shifted towards interregional dynamics in glioma patients. More precisely, the phase dynamics is unchanged as the coupling strength grows with the square root of the excitability (Hopf) parameter. At the individual and population-based level, we found that glioma patients exhibit whole-brain dynamics with stronger interregional coupling than controls. Moreover, the tumor regions of individual patients contribute to this increase though there is considerable variation across patients. In summary, we demonstrate the existence of an intimate link between global and local dynamics in whole-brain modeling and show that the contribution of global and local dynamics to emergent whole-brain dynamics is disrupted by the presence of tumors in glioma patients.

Chapter 7

Epilogue

7.1 Summary

In this thesis, we have explored how brain diseases affect neuronal dynamics. We have seen how a dynamical systems approach can formulate existing hypotheses quantitatively and inspire new theories of brain pathologies. Given the long timescales involved and the impracticalities of brain imaging, theoretical models are essential for making sense of brain diseases.

- In Chapter 4, we linked a model for Alzheimer's disease progression to a model for neuronal activity, both on the whole-brain scale. By doing so, we could test a recently proposed hypothesis of Alzheimer's disease mechanism. Despite numerous hypotheses, the precise mechanism behind the pathology of Aβ and τP is unknown. One hypothesis is that Aβ causes hyperactivity and that τP causes hypoactivity. Our mathematical model tested this hypothesis, demonstrating that it reproduces the hallmark changes in neuronal activity in Alzheimer's disease. Furthermore, we can explain why our model reproduces these features due to our choice of simple phenomenological models. For example, we demonstrate that τP induces the oscillatory slowing effect seen in the later stages of the disease. However, we did not take into account how neuronal activity can impact disease progression.
- In Chapter 5, we explored how neuronal activity can affect protein spreading. Recent experimental work demonstrates that higher neuronal firing leads to higher rates of protein transport between neurons. The particular proteins in question spread via synapses between connected neurons and are relevant to diseases including Alzheimer's and Parkinson's disease. As such, two processes interact on the same neuronal network: neuronal activity and protein

spreading. These two processes are naturally captured as a slow-fast dynamical system, as the neuronal activity occurs on a much faster timescale than the protein spreading. We find that heterogeneous neuronal firing induces symmetry breaking in protein spreading and can induce toxic outbreaks. From these results, it is conceivable that neuronal firing patterns determine which regions are more vulnerable to neurodegenerative diseases. In this and the previous chapter, however, we relied on simulations and analysis to draw conclusions, without the assimilation of clinical data.

- In Chapter 6, we explored the differences in neuronal dynamics in brain cancer patients using a whole-brain model. By fitting a Hopf whole-brain model to empirical functional connectivity, we demonstrated that the ratio between interregional coupling and intraregional excitability largely determines phase correlations. Furthermore, we observed considerable differences in interregional-versus-intraregional dynamics between glioma patients and healthy controls, both on an individual and population-based level. In particular, we showed that local tumor pathology induces shifts in the global brain dynamics by increasing the strength of interregional coupling.

In conclusion, brain diseases impart differences in brain function, which can be understood by combining mathematical models of neuronal activity and disease progression. In this thesis, we have demonstrated that these two modeling frameworks can be integrated to understand the changes in brain functioning during disease.

7.2 Limitations

It is important to acknowledge that the thesis presented herein has certain limitations. These limitations may affect the generalizability of the findings and should be taken into account when interpreting the results.

In Chapter 4, we present a mathematical model which recapitulates early-stage hyperactivity, late-stage hypoactivity, and oscillatory slowing. We interpret the power component of the periodogram of the simulated data as neuronal activity. From a clinical perspective, this is inaccurate. It is unclear how neuronal oscillations measured by MEG relate to levels of neuronal activity. It may very well be that higher power in MEG relates to synchrony in neuronal populations and not their general activity levels. However, in the context of neuronal mass modeling, in which we have full control of the mathematical interpretability of the simulated data, we deem it reasonable that higher power relates to higher activity. The oscillatory slowing identified in Alzheimer's disease is also not free from controversy. Power spectra are often normalized so that their total power equals one. Therefore, it is conceivable that rises in the lower frequency band may lead to an artificial decrease in the alpha peak. Furthermore, frequency resolutions of simulated and empirical data will impact the interpretation of changes in power spectra. If the frequency resolution is too large, it may not detect changes in frequency but may also give the impression of sudden large changes in peak frequency, which in reality is the result of numerical error (in the case of simulated data) or inaccuracies in the empirical data processing. Computation of frequency resolutions is also a best-case estimate, as different periodogram estimation algorithms may lower the resolution further. The choice of neural mass model can have significant impact on the conclusions drawn in computational studies [209]. It is important to note that the results given here are expected for neural mass dynamics parameterized close to a Hopf bifurcation. Furthermore, when comparing parameters between neural mass models it is important to consider their impact on the model from a dynamical systems perspective and not from their biological interpretation.

In Chapter 5, we present a model of the interplay between neuronal activity and protein spreading. As a starting point, we chose to model neuronal activity by phase oscillators with Kuramoto coupling. Though this is a common modeling assumption, it would be more accurate to opt for quadratic integrate-and-fire neurons instead, as the model parameters would have a clearer biological interpretation. The analytic results in this chapter were found by critical manifold methods and crude averaging, both of which are only good approximations of the dynamics in the singular limit (the time scale separation growing to infinity). As such, it is unclear whether dynamic phenomena beyond those discussed are present in the system. Numerical continuation methods may be employed to study this system further. Additionally, although it is reasonable to assume that the protein spreading and neuronal activity operate on significantly different timescales on a whole-brain level, it is unclear whether this is true at the neuronal level. Hence, it may be important to consider dynamics where timescale separation is not valid.

In Chapter 6, we fit a whole-brain model of neuronal activity to MEG data to investigate the impact of glioma on neuronal dynamics. Due to the difficulties of parameterizing whole-brain models, we are only able to consider global parameters and not local parameters specific to different regions. This is a considerable limitation that also plagues other studies employing whole-brain models. As such, it is not clear how changes in global parameters between patients and control should be interpreted.

It is not possible to directly state which region is contributing to the global changes or whether synergistic effects between regions contribute. Our pseudo-craniotomy approach is an attempt to glean the impact of specific regions on the overall global dynamics. However, the pseudo-craniotomy approach needs to be further studied to clarify its methodological potential. Although the PLI metric is designed to avoid artificial correlations due to volume conduction, the computational methods used to assign sensor signals to brain regions may nonetheless suffer from volume conduction. As such, although the zero-lag correlation may be removed, that does not mean that volume conduction has disappeared from the data and may still impact the PLI computation in the empirical data. Furthermore, the processing of both the simulated and empirical data may affect the PLI computation. For example, the filtering of the signal (Butterworth filter) may induce artificial correlation values between regions that operate in separate frequency bands. All in all, it should be noted that there are several data processing steps that may inflate the correlations seen, and only robustly reproducible PLI values should be trusted.

7.3 Future work

There are several directions to take the research presented further. We will outline a few of them here.

Although the multiscale model of Alzheimer's disease presented in Chapter 4 successfully reproduces several key characteristics of the disease, it has not yet been fitted to clinical data. This massive undertaking would involve protein concentration data (PET) and neuronal dynamics data (EEG/MEG/fMRI), where these modalities could be fitted either concurrently or in isolation. Recent work has successfully fitted individualized tau trajectories using Bayesian inference methods [7]. As such, it is possible that individualized trajectories of neuronal activity abnormalities—and, further down the line, cognitive abnormalities—may be predictable with mathematical modeling. With the integration of clinical data, more refined methods for model selection, e.g. Bayesian inference, can be used to test hypotheses of protein-mediated pathology in neurodegenerative disease.

The slow-fast model of interacting protein transport and neuronal activity from Chapter 5 is based on experimental results found at the single neuron scale. As such, the heterodimer-oscillator model is better interpreted as a model for transport between neuronal cells, not brain regions, as are commonly used in modeling disease progression. For this reason, developing a mean-field description of a large network of heterodimer-oscillator neurons would be advantageous. Such an approach could consist of combining a next-generation neural mass model of quadratic integrate-and-fire neurons [151, 210, 211] and network mean-field models of spreading processes [212]. Furthermore, the theoretical implications of the symmetry-breaking identified in the spreading patterns can be explored using clinical data. For example, glucose PET can be used as a proxy for average neuronal activity, which can then be utilized to create a modified (asymmetric) Laplacian matrix for spreading dynamics. This approach incorporates the impact of neuronal activity on protein transport without the need for computationally expensive fast-slow dynamics simulations.

As for the neuronal dynamics of glioma patients, it would be valuable to understand not only the global changes—as studied in Chapter 6—but also the local changes induced by tumors. Doing so, more precise hypotheses could be tested about the direct impact tumors have on neuronal dynamics, as opposed to adaptive changes to global brain dynamics. It may thus be advantageous to infer parameters of more detailed and biophysical neural masses with local MEG signals, instead of focusing on global functional connectivity patterns. Furthermore, the spreading of metastasizing tumors can be introduced to the model in a similar fashion to the multiscale model of Alzheimer's progression. It is also conceivable to explore the glutamate-mediated feedback loop between glial tumors and neuronal activity in a similar vein to the heterodimer-oscillator model.

More generally, we can envision a more complete mathematical model for disease progression in the brain, where both neuronal activity and disease progression interact with slow-fast dynamics and are equipped with parameters inferred from clinical data. Such a comprehensive mathematical model will be challenging to integrate efficiently, in particular, if the neuronal activity is transmitted with delays. Additionally, fitting such a model necessitates longitudinal data from multiple modalities, such as PET and MEG, of individual patients over numerous years. Obtaining such a dataset would be a remarkable achievement. Nonetheless, bringing all these elements together could provide the vital knowledge needed to finally understand and treat diseases such as Alzheimer's, Parkinson's, and brain cancer.

In this thesis, we have explored the effects of diseases on brain function using mathematical models of neuronal activity and disease spreading. We have demonstrated how these models can be used to quantitatively formulate hypotheses regarding disease mechanisms and to understand changes in brain functioning. Furthermore, we have shown that neuronal activity can impact the progression of brain diseases, opening up several fruitful avenues of research. The research presented herein provides a foundation for further investigation into the role of neuronal dynamics in brain diseases and has significant implications for understanding and treating neurodegenerative diseases.

Appendix A

Complementary results to Chapter 5

A.1 Coefficients of the cubic

The toxic solution for the skewed heterodimer model is given by the real positive solution (when it exists) of a cubic equation for the toxic fixed point ($v_2 \neq 0$) given by

$$c_0 + c_1 v_2 + c_2 v_2^2 + c_3 v_2^3 = 0$$

with

$$\begin{aligned}
c_0 =& (A+\ell)(k_3(A+2\ell+k_3) + k_1^4 + 4\ell(A+\ell)k_0^2k_2^2 - 2(A+2\ell)k_0k_1k_2(A^2+2\ell(\ell+k_3)+ \\
&A(2\ell+k_3) - k_0k_2) + k_1^3(2(A+2\ell)k_3(A+2\ell+k_3) - (A+2(\ell+k_3))k_0k_2) \\
&+ k_1^2((A+2\ell)^2k_3(A+2\ell+k_3) - (3A^2+8\ell(\ell+k_3)+4A(2\ell+k_3))k_0k_2 + k_0^2k_2^2)), \\
c_1 =& k_2(A^4k_1k_3 + A^3(3k_1^2k_3 - 2k_0k_1k_2 + 2k_0k_3k_2 + 6k_1k_3\ell) + A^2(2k_1^3k_3 + 2k_0k_2(k_3^2 + 2k_0k_2 + k_3\ell) \\
&+ k_1^2(3k_3^2 - k_0k_2 + 15k_3\ell) - k_1(k_3^3 + 6k_0k_3k_2 + 8k_0k_2\ell - 14k_3\ell^2)) \\
&+ (k_1+2\ell)(k_1^2k_3(k_3^2+5k_3\ell+6\ell^2) + k_0k_2(-2k_3\ell^2 + k_0k_2(k_3+2\ell)) + k_1(2k_3\ell^2(k_3+2\ell) \\
&- k_0k_2(2k_3^2+7k_3\ell+4\ell^2))) + A(k_1^3k_3(3k_3+7\ell) + 2k_0k_2(k_3(k_3-2\ell)\ell + k_0k_2(k_3+4l)) \\
&+ k_1^2(-5k_0k_2(k_3+l) + k_3\ell(11k_3+26\ell)) + 2k_1(k_0^2k_2^2 - k_0k_2(k_3^2+10k_3\ell+7\ell^2) \\
&+ k_3\ell(-k_3^2+k_3\ell+8\ell^2))), \\
c_2 =& k_2^2(A^3(k_1-k_3)k_3 + A^2k_3(k_1^2+2k_1k_3-k_3^2-4k_0k_2+5k_1\ell-3k_3\ell) \\
&+ (k_3+2\ell)(-3k_0k_3k_2\ell - k_0k_1k_2(2k_3+\ell) + k_1^2k_3(2k_3+3\ell) + k_1k_3\ell(3k_3+4\ell)) \\
&+ A(k_1^2k_3(3k_3+5\ell) + k_1(k_3^3 - 3k_0k_3k_2 + 8k_3^2\ell - 2k_0k_2\ell \\
&+ 10k_3\ell^2) - k_3(k_3\ell(k_3+2\ell) + k_0k_2(3k_3+10\ell))), \\
c_3 =& k_3k_2^3(A+k_3+2\ell)(Ak_3+k_3\ell+k_1(k_3+\ell)).
\end{aligned}$$

A.2 Critical clearance for the skewed heterodimer model

In this section, we show that the critical clearance of the 2-node skewed heterodimer model is constrained to the interval $[k_0k_2/k_1, 2k_0k_2/k_1]$ and is monotonically increasing in the activity parameter A.

A.2.1 Critical clearance bounds

In the skewed heterodimer 2-node system (Section 5.2), the healthy fixed point switches stability at a critical value for toxic clearance given by

$$k_3^{\text{crit}} = \frac{k_0k_2 + \kappa^{\text{crit}}}{k_1}, \tag{A.1}$$

where κ^{crit} is given in Section 5.2. We now verify the statement that $\frac{k_0k_2}{k_1} \leq k_3^{\text{crit}} \leq 2\frac{k_0k_2}{k_1}$ by showing that $0 \leq \kappa^{\text{crit}} \leq k_0k_2$. As all parameters are nonnegative the following inequality holds

$$4k_0k_2\left(k_1\left(A+k_1+2l\right)\left(k_1(A+2l)+4l(A+l)\right)+k_0k_2\left(k_1+2l\right)\left(2(A+l)+k_1\right)\right) \geq 0. \tag{A.2}$$

The inequality can be rewritten in terms of s_0 and s_1 as defined in Section 2.2, giving

$$(2l+A+k_1)^2(k_1(2l+A)+2k_0k_2)^2 \geq s_0^2 + s_1. \tag{A.3}$$

Taking the square root of both sides and rearranging gives us the desired $\kappa^{\text{crit}} \leq k_0k_2$. As mentioned in Section 2.2, $\kappa^{\text{crit}} \geq 0$ since all parameters are nonnegative. Conclusively, we have that $\frac{k_0k_2}{k_1} \leq k_3^{\text{crit}} \leq 2\frac{k_0k_2}{k_1}$.

A.2.2 Monotonic dependence of critical clearance on activity

We now verify the statement that k_3^{crit} is monotonically increasing in A by showing that $\frac{\delta\kappa^{\text{crit}}}{\delta A} \geq 0$. As all parameters are nonnegative, the following inequality holds

$$\frac{4Ak_0k_2}{k_1^2(2l+A+k_1)^4}[B_1+B_2+B_3+B_4] \geq 0, \tag{A.4}$$

where

$$B_1 = k_1^3\left(A+k_1+2l\right)^4\left(k_1(A+4l)+4l(A+2l)\right), \tag{A.5a}$$

$$B_2 = k_0k_1^2k_2\left(k_1+2l\right)\left(A+k_1+2l\right)^2\left(4A^2+k_1(5A+4l)+14Al+8l^2\right), \tag{A.5b}$$

$$B_3 = 4Ak_0^2k_1k_2^2\left(k_1+2l\right)\left(A+k_1+2l\right)\left(A+2k_1+4l\right), \tag{A.5c}$$

$$B_4 = 4Ak_0^3k_2^3\left(k_1+2l\right)^2. \tag{A.5d}$$

Rearranging the above inequality gives

$$\left(\frac{4Ak_0^2k_2^2\left(k_1+2l\right)}{k_1\left(A+k_1+2l\right)^2}+\frac{2Ak_0k_2\left(A+2k_1+4l\right)}{A+k_1+2l}+k_1(A+2l)\left(A+k_1+2l\right)\right)^2 \geq s_0^2+s_1, \tag{A.6}$$

where s_0 and s_1 are again defined as in Section 5.2. Taking the square root of the right- and left-hand side of the above inequality and dividing both sides by $4(2l + A + k_1)^2\sqrt{s_0^2+s_1}$ produces

$$k_1\frac{\partial\kappa^{\text{crit}}}{\partial A} \geq 0, \tag{A.7}$$

showing that k_3^{crit} is monotonically increasing in A. The full expression of the partial derivative has been omitted due to its length.

Appendix B

Data gathering and processing for Chapter 6

B.1 Participants

A total of $S = 10$ patients seen between 2011–2023 at Amsterdam UMC with suspected diffuse glioma were randomly selected from an ongoing prospective study on brain networks. Patients underwent MEG when glioma was suspected based on clinical history and MRI before tumor treatment or surgery was performed. Exclusion criteria were (1) age < 18 years, (2) psychiatric disease, (3) comorbidities of the central nervous system, (4) insufficient mastery of the Dutch language, and (5) inability to communicate adequately. After resection, molecular characteristics were assessed as part of the clinical routine, including prognostically favorable isocitrate dehydrogenase (IDH) mutations and 1p/19q codeletions [213]. This led to three subgroups: IDH-wildtype glioma (glioblastoma), IDH-mutant, non-codeleted glioma, and IDH-mutant, 1p/19q-codeleted glioma. Additionally, $S = 33$ healthy controls were included, as described in [214]. We refer to these two cohorts as the *glioma cohort* and the *control cohort*. The VUmc Medical Ethical Committee approved this study, which was conducted following the principles of the Declaration of Helsinki. All participants provided written informed consent before participation.

B.2 MEG data acquisition and processing

MEG was recorded for 5 min in the supine position during the eyes-closed, no-task resting state in a magnetically shielded room (VacuumSchmelze GmBh, Hanau, Germany), using a 306-channel (102 magnetometers, 204 gradiometers) whole-head MEG system (Elekta Neuromag Oy, Helsinki, Finland) and a sampling frequency of 1250Hz.

Anti-aliasing (410Hz) and high-pass filters (0.1Hz) were applied online. Preprocessing involved visual inspection, noisy channel removal, and noise removal in the remaining signals. Anatomical MRI was used for co-registration with the digitized scalp surface and the Automated Anatomical Labeling atlas [215] for parcellation of the cortical ribbon into 78 regions. Broadband time series of neuronal activity were then reconstructed for each region's centroid [216] using a scalar beamformer approach [217].

Median peak frequencies of the spectral density were also computed for the control cohort (for the parameterization of the whole-brain model). For this purpose, epochs were curated visually by discarding epochs without clear alpha frequency peaks in occipital brain regions. Then, the peak frequency of each region in each epoch was computed by finding the frequency above 4Hz with the highest spectral density and discarding peaks that were less than twice the average spectral density of the background spectrum. The median peak frequency of each brain region was then computed across all subjects and epochs.

B.3 MRI data and structural connectome reconstruction

Control MRI data were obtained using a 3T MRI system (Philips Ingenia CX) with a 32-channel receive-only head coil at the Spinoza Centre for Neuroimaging in Amsterdam, The Netherlands. A high-resolution 3D T1-weighted image was collected with a magnetization-prepared rapid acquisition with gradient echo (MPRAGE; TR = 8.1 ms, TE = 3.7 ms, flip angle = 8°, voxel dimensions = 1 mm^3 isotropic). This anatomical scan was registered to MNI space through linear registration with nearest-neighbor interpolation and was used for co-registration and normalization of other modalities (dMRI and MEG) to the same space.

Diffusion MRI was collected in the controls only, with diffusion weightings of $b = 1,000$ and 2,000 s/mm^2 applied in 29 and 59 directions, respectively, along with 9 nondiffusion weighted (b = 0s/mm2) volumes using a multiband sequence (MultiBand SENSE factor = 2, TR = 4.7 s, TE = 95 ms, flip angle = 90°, voxel dimensions = 2 mm3 isotropic, no interslice gap). In addition, two scans with opposite phase encoding directions were collected for blip-up blip-down distortion correction using FSL topup [218]. Structural connectomes were constructed by performing probabilistic anatomically-constrained tractography (ACT) [219] in MRtrix3 [220]. A tissue response function was estimated from the preprocessed and bias field corrected dMRI data using the multishell multitissue five-tissue-type algorithm (msmt_5tt). Subsequently, the fiber orientation distribution for each voxel was determined by performing multishell multitissue-constrained spherical deconvolution (MSMT-CSD) [221]. ACT was performed by randomly seeding 100 million fibers within the white matter to construct a tractogram, and spherical-deconvolution informed filtering of tractograms (SIFT, SIFT2 method in MRtrix3) [222] was then performed to improve the accuracy of the reconstructed streamlines and reduce false positives. For every participant, their respective 3D T1-weighted image was used to parcellate the brain into the 78 cortical regions. We then used this parcellation to convert the tractogram to a structural network, where weighted edges represented the sum of all streamlines leading to and from all voxels within two brain regions. For patients, tumor masks were manually drawn on a combination of T1-weighted MRI, with and without contrast, and FLAIR. Then, the atlas regions overlapping with each patient's tumor mask were considered tumor regions.

Appendix C

Complementary results to Chapter 6

C.1 Structural connectivity scaling

For varying levels of excitability values, we find that the goodness of fit of the Hopf whole-brain model is largely insensitive to the scaling of the structural connectome. As demonstrated in Figure C.1, the scaling of the structural connectome just needs to be of sufficient magnitude to achieve optimal fit.

C.2 Network metrics of simulated functional connectivity

The network metrics of the simulated phase-lag index connectivity are not similar to the metrics found for empirical phase-lag index connectivity for optimal model parameters. There are only minor differences in network metrics between the optimal fit for the glioma and the control cohort, as shown in Fig. C.2.

C.3 The effect of thresholding the empirical functional connectivity

The difference in optimal normalized coupling strength between the glioma and control cohort is for the most part positive across varying degrees of thresholding (see Figure C.4 and C.5). Both cohorts' functional connectivity fit has its peak around 97% thresholding, which is the threshold used for the simulations in Chapter 6 unless specified otherwise.

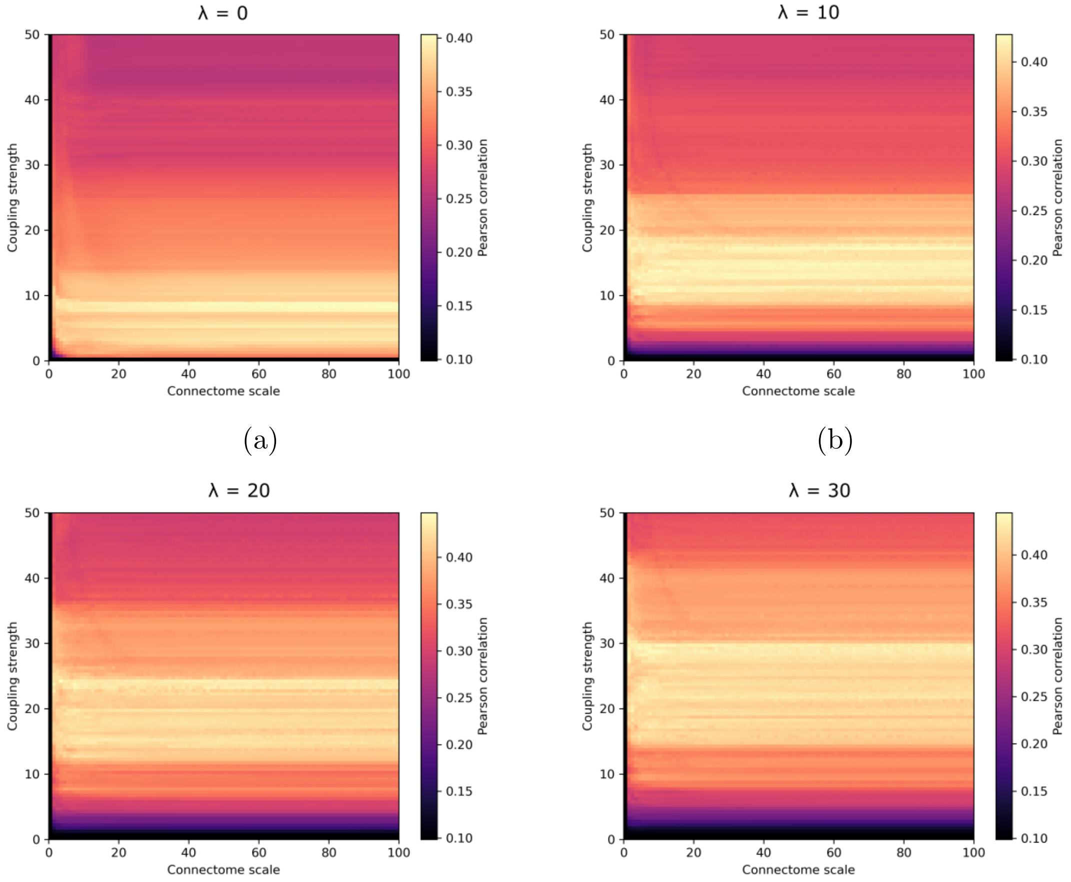

(a) (b)

(c) (d)

Figure C.1: Grid search over coupling strength and connectome scaling for different excitability values for a set, random initial condition of the Hopf whole-brain model. Each pixel corresponds to the Pearson correlation between simulated and experimental (healthy control group) phase-lag index connectivity derived from MEG. As shown, the connectome scaling does not alter the model fit when sufficiently large, when varying the coupling strength and global excitability parameter λ. *(a)* $\lambda = 0$, *(b)* $\lambda = 10$, *(c)* $\lambda = 20$, *(d)* $\lambda = 30$.

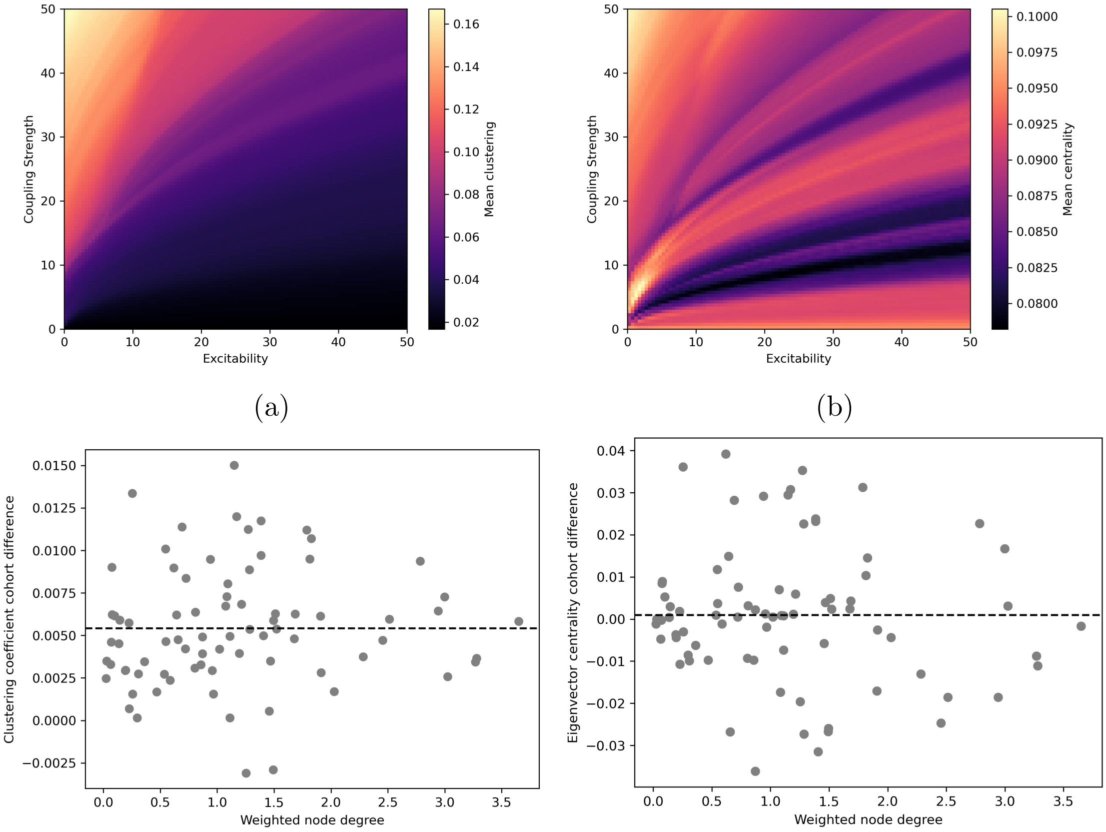

(a) (b)

(c) (d)

Figure C.2: Network metrics of the simulated phase-lag index connectivity. *(a)* The average clustering coefficient of synthetic functional connectivity (phase-lag index) of the Hopf whole-brain model over the coupling strength and excitability parameter. The experimental clustering coefficient is around 0.2 for the healthy cohort. *(b)* The average eigenvector centrality over coupling strength and excitability. The empirical average eigenvector centrality is close to 0.05. *(c,d)* The difference in the simulated clustering coefficient and eigenvector centrality between the optimal model fit for the glioma and control group per node (plotted by their weighted structural node degree). The black stippled line shows the average difference, both of which are close to zero.

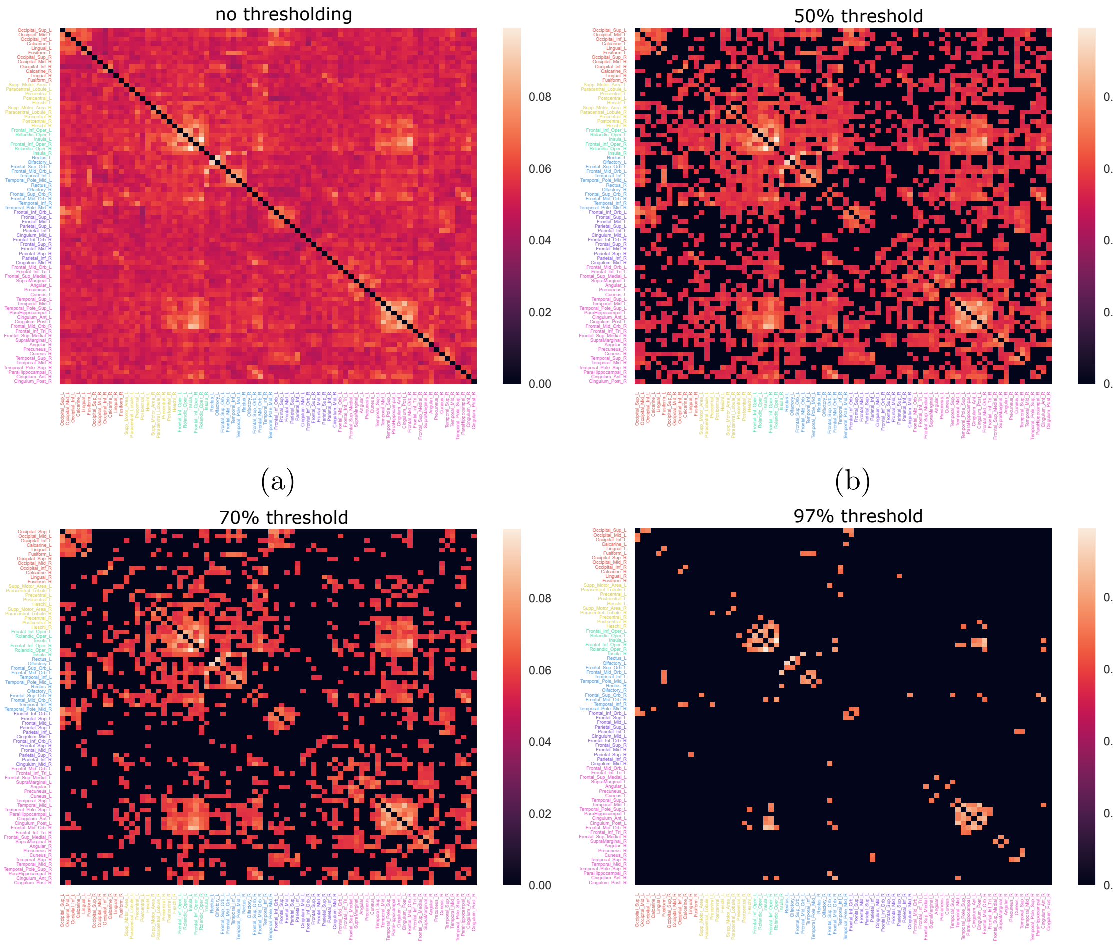

(a) (b)

(c) (d)

Figure C.3: The post-processed average experimental phase-lag index connectome of the control group for varying levels of thresholding. During thresholding, all elements that belong to the lower X% are set to zero while others are kept at their original value. *(a)* before thresholding, *(b)* 50% (median threshold), *(c)* 70%, *(d)* 97% (the percentage giving the highest goodness of fit to simulated data).

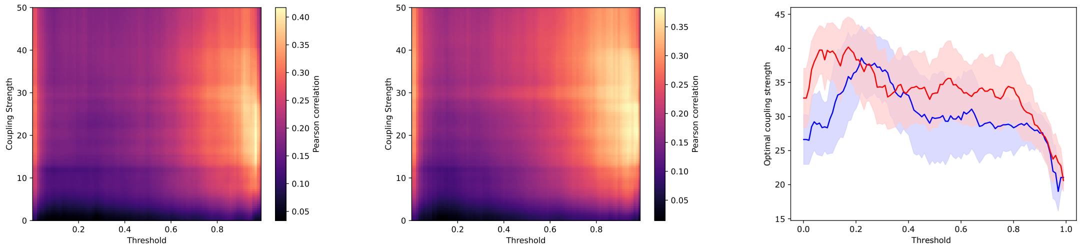

Figure C.4: Grid searches showing the effect of coupling strength and thresholding of experimental phase-lag connectomes on the Pearson correlation between simulated and experimental phase-lag connectivity. The grid search matrices show the average of 300 initial conditions for the Hopf whole-brain model. *(a)* Grid search showing the fit to the average healthy phase-lag connectivity. *(b)* Grid search showing the fit to the average glioma patient phase-lag connectivity. *(c)* Plot showing the average (solid line) and standard deviation (shaded region) of the optimal coupling strength per experimental threshold for the control (blue) and glioma (red) cohort over initial conditions.

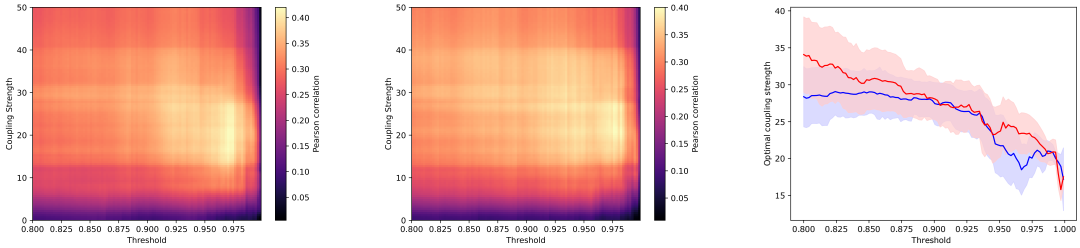

Figure C.5: This plot is identical to Fig. C.4 but zoomed in for higher threshold values.

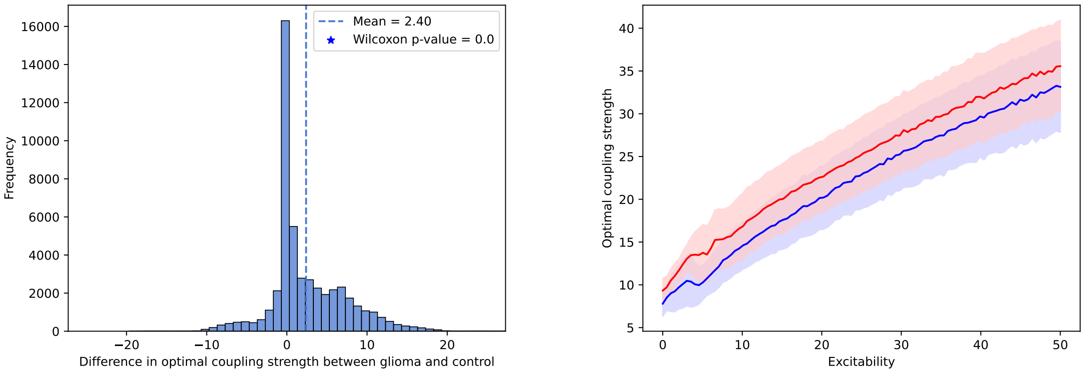

(a)

(b)

Figure C.6: Optimal parameters for the Hopf whole-brain model fitted to PLI functional connectivity data when thresholded by their median value. The model was fitted to average PLI over each group for 100 randomized initial conditions. (a) The difference in optimal coupling strength (pooled over all excitability parameter values for 100 different initial conditions. (b) The mean (solid line) and standard deviation (shaded region) of optimal coupling strength per excitability parameter for the healthy (blue) and glioma cohort (red).

When thresholding the glioma and control cohort by their median values (not the same thresholding value between the cohorts), we obtain similar results as for the optimal thresholding value (as shown in Chapter 6) though with smaller differences in optimal coupling strength between the cohorts (see Figure C.6).

Bibliography

1. Carbonell, F., Iturria-Medina, Y. & Evans, A. C. Mathematical Modeling of Protein Misfolding Mechanisms in Neurological Diseases: A Historical Overview. *Frontiers in Neurology* **9.** doi:`10.3389/fneur.2018.00037`. (2024) (2, 2018).
2. Vogel, J. W. *et al.* Connectome-based modelling of neurodegenerative diseases: towards precision medicine and mechanistic insight. *Nature Reviews Neuroscience* **24,** 620–639. doi:`10.1038/s41583-023-00731-8`. (2024) (2023).
3. Mould, D. R., Denman, N. G. & Duffull, S. Using disease progression models as a tool to detect drug effect. *Clinical Pharmacology and Therapeutics* **82,** 81–86. doi:`10.1038/sj.clpt.6100228` (2007).
4. Chan, P. L. & Holford, N. H. Drug treatment effects on disease progression. *Annual Review of Pharmacology and Toxicology* **41,** 625–659. doi:`10.1146/annurev.pharmtox.41.1.625` (2001).
5. Sanga, S. *et al.* Mathematical modeling of cancer progression and response to chemotherapy. *Expert Review of Anticancer Therapy* **6,** 1361–1376. doi:`10.1586/14737140.6.10.1361`. (2024) (1, 2006).
6. Henderson, M. X. *et al.* Spread of alpha-synuclein pathology through the brain connectome is modulated by selective vulnerability and predicted by network analysis. *Nature Neuroscience* **22,** 1248–1257. doi:`10.1038/s41593-019-0457-5`. (2024) (2019).
7. Chaggar, P. *et al.* *Personalised Regional Modelling Predicts Tau Progression in the Human Brain* 29, 2023. doi:`10.1101/2023.09.28.559911`. (2024).
8. Bies, R., Gastonguay, M. & Schwartz, S. Mathematics for Understanding Disease. *Clinical Pharmacology & Therapeutics* **83,** 904–908. doi:`10.1038/clpt.2008.53`. (2024) (2008).
9. Dugger, B. N. & Dickson, D. W. Pathology of Neurodegenerative Diseases. *Cold Spring Harbor Perspectives in Biology* **9,** a028035. doi:`10.1101/cshperspect.a028035`. (2024) (1, 2017).
10. Jucker, M. & Walker, L. C. Propagation and spread of pathogenic protein assemblies in neurodegenerative diseases. *Nature Neuroscience* **21,** 1341–1349. doi:`10.1038/s41593-018-0238-6`. (2024) (2018).

11. Walker, L. C. in *Human Prion Diseases* (eds Pocchiari, M. & Manson, J.) 303–319 (Elsevier, 2018). doi:`https://doi.org/10.1016/B978-0-444-63945-5.00016-7`.

12. Hsiao, F.-J., Wang, Y.-J., Yan, S.-H., Chen, W.-T. & Lin, Y.-Y. Altered oscillation and synchronization of default-mode network activity in mild Alzheimer's disease compared to mild cognitive impairment: an electrophysiological study. *PloS one* **8,** e68792–e68792. doi:`10.1371/journal.pone.0068792` (2013).

13. Wang, R. *et al.* Multiple feature extraction and classification of electroencephalograph signal for Alzheimers' with spectrum and bispectrum. *Chaos: An Interdisciplinary Journal of Nonlinear Science* **25,** 013110. doi:`10.1063/1.4906038` (2015).

14. Gouw, A. A. *et al.* EEG spectral analysis as a putative early prognostic biomarker in nondemented, amyloid positive subjects. *Neurobiology of Aging* **57,** 133–142. doi:`https://doi.org/10.1016/j.neurobiolaging.2017.05.017` (2017).

15. Campbell, S. L., Buckingham, S. C. & Sontheimer, H. Human glioma cells induce hyperexcitability in cortical networks. *Epilepsia* **53,** 1360–1370. doi:`10.1111/j.1528-1167.2012.03557.x` (2012).

16. Tao, J.-C. *et al.* Interactions between microglia and glioma in tumor microenvironment. *Frontiers in Oncology* **13.** doi:`10.3389/fonc.2023.1236268`. (2024) (28, 2023).

17. Hodgkin, A. L. & Huxley, A. F. A quantitative description of membrane current and its application to conduction and excitation in nerve. *The Journal of Physiology* **117,** 500–544. doi:`10.1113/jphysiol.1952.sp004764`. (2024) (1952).

18. Pathak, A., Roy, D. & Banerjee, A. Whole-Brain Network Models: From Physics to Bedside. *Frontiers in Computational Neuroscience* **16.** (2023) (2022).

19. Deco, G. & Kringelbach, M. L. Great Expectations: Using Whole-Brain Computational Connectomics for Understanding Neuropsychiatric Disorders. *Neuron* **84,** 892–905. doi:`10.1016/j.neuron.2014.08.034`. (2023) (3, 2014).

20. Toga, A. W., Clark, K. A., Thompson, P. M., Shattuck, D. W. & Van Horn, J. D. Mapping the Human Connectome. *Neurosurgery* **71,** 1–5. doi:`10.1227/NEU.0b013e318258e9ff` (2012).

21. Raj, A. & Powell, F. Models of Network Spread and Network Degeneration in Brain Disorders. *Biological Psychiatry: Cognitive Neuroscience and Neuroimaging. Computational Methods and Modeling in Psychiatry* **3,** 788–797. doi:`10.1016/j.bpsc.2018.07.012`. (2024) (1, 2018).

22. Vogel, J. W. *et al.* Spread of pathological tau proteins through communicating neurons in human Alzheimer's disease. *Nature Communications* **11,** 2612. doi:`10.1038/s41467-020-15701-2`. (2023) (26, 2020).

23. Freundt, E. C. *et al.* Neuron-to-neuron transmission of alpha-synuclein fibrils through axonal transport. *Annals of Neurology* **72,** 517–524. doi:`10.1002/ana.23747` (2012).

24. Alexandersen, C. G., de Haan, W., Bick, C. & Goriely, A. A multi-scale model explains oscillatory slowing and neuronal hyperactivity in Alzheimer's disease. *Journal of The Royal Society Interface* **20,** 20220607. doi:`10.1098/rsif.2022.0607`. (2023) (4, 2023).

25. Alexandersen, C. G., Goriely, A. & Bick, C. *Neuronal activity induces symmetry breaking in neurodegenerative disease spreading* 2, 2023. doi:`10.1101/2023.10.02.560495`. (2023).

26. Alexandersen, C. G., Douw, L., Zimmermann, M. L. M., Bick, C. & Goriely, A. *Pseudo-craniotomy of a whole-brain model reveals tumor-induced alterations to neuronal dynamics in glioma patients* 23, 2023. doi:`10.1101/2023.12.22.573027`. (2024).

27. Herculano-Houzel, S. The Human Brain in Numbers: A Linearly Scaled-up Primate Brain. *Frontiers in Human Neuroscience* **3,** 31. doi:`10.3389/neuro.09.031.2009`. (2024) (9, 2009).

28. Longstaff, A. *Instant notes : neuroscience* (BIOS Scientific Publishers, London, 2000).

29. Henley, C. *Foundations of Neuroscience* (Michigan State University, 2021).

30. Quinton, S. Saundra K. Ciccarelli and J. Noland White, Psychology (4th Edition/Global Edition) (2015).

31. Ackerman, S. in *Discovering the Brain* (National Academies Press (US), 1992). (2024).

32. Jawabri, K. H. & Sharma, S. in *StatPearls* (StatPearls Publishing, Treasure Island (FL), 2024). (2024).

33. Alreja, A., Nemenman, I. & Rozell, C. J. Constrained brain volume in an efficient coding model explains the fraction of excitatory and inhibitory neurons in sensory cortices. *PLOS Computational Biology* **18,** e1009642. doi:`10.1371/journal.pcbi.1009642`. (2024) (21, 2022).

34. Custo Greig, L., Woodworth, M., Galazo, M., Padmanabhan, H. & Macklis, J. Molecular logic of neocortical projection neuron specification, development and diversity. *Nature reviews. Neuroscience* **14,** 10.1038/nrn3586. doi:`10.1038/nrn3586`. (2024) (2013).

35. *Brain Anatomy and How the Brain Works* (2024).

36. Pang, J. C. *et al.* Geometric constraints on human brain function. *Nature* **618,** 566–574. doi:`10.1038/s41586-023-06098-1`. (2024) (2023).

37. Bressloff, P. C. Spatiotemporal dynamics of continuum neural fields. *Journal of Physics A: Mathematical and Theoretical* **45,** 033001. doi:`10.1088/1751-8113/45/3/033001`. (2024) (2011).

38. Lowe, M. J. *et al.* Modern Methods for Interrogating the Human Connectome. *Journal of the International Neuropsychological Society : JINS* **22,** 105–119. doi:`10.1017/S1355617716000060` (2016).

39. Cabral, J., Kringelbach, M. L. & Deco, G. Functional connectivity dynamically evolves on multiple time-scales over a static structural connectome: Models and mechanisms. *NeuroImage. Functional Architecture of the Brain* **160,** 84–96. doi:`10.1016/j.neuroimage.2017.03.045`. (2024) (15, 2017).

40. Stefanovski, L. *et al.* Linking Molecular Pathways and Large-Scale Computational Modeling to Assess Candidate Disease Mechanisms and Pharmacodynamics in Alzheimer's Disease. *Frontiers in Computational Neuroscience* **13.** (2023) (2019).

41. Liu, Z., Han, F. & Wang, Q. A review of computational models for gamma oscillation dynamics: from spiking neurons to neural masses. *Nonlinear Dynamics* **108,** 1849–1866. doi:`10.1007/s11071-022-07298-6`. (2024) (1, 2022).

42. Ermentrout, G. B. & Chow, C. C. Modeling neural oscillations. *Physiology & Behavior* **77,** 629–633. doi:`10.1016/S0031-9384(02)00898-3`. (2024) (1, 2002).

43. Cooper, N. R., Croft, R. J., Dominey, S. J. J., Burgess, A. P. & Gruzelier, J. H. Paradox lost? Exploring the role of alpha oscillations during externally vs. internally directed attention and the implications for idling and inhibition hypotheses. *International Journal of Psychophysiology* **47,** 65–74. doi:`10.1016/S0167-8760(02)00107-1`. (2024) (1, 2003).

44. Ward, L. M. Synchronous neural oscillations and cognitive processes. *Trends in Cognitive Sciences* **7,** 553–559. doi:`10.1016/j.tics.2003.10.012`. (2024) (1, 2003).

45. Akeju, O. & Brown, E. N. Neural oscillations demonstrate that general anesthesia and sedative states are neurophysiologically distinct from sleep. *Current Opinion in Neurobiology. Neurobiology of Sleep* **44,** 178–185. doi:`10.1016/j.conb.2017.04.011`. (2024) (1, 2017).

46. Caplan, J. B., Madsen, J. R., Raghavachari, S. & Kahana, M. J. Distinct patterns of brain oscillations underlie two basic parameters of human maze learning. *Journal of Neurophysiology* **86,** 368–380. doi:`10.1152/jn.2001.86.1.368` (2001).

47. Khanna, P. & Carmena, J. M. Neural oscillations: beta band activity across motor networks. *Current Opinion in Neurobiology. Large-Scale Recording Technology (32)* **32,** 60–67. doi:`10.1016/j.conb.2014.11.010`. (2024) (1, 2015).

48. Fell, J. *et al.* Human memory formation is accompanied by rhinal-hippocampal coupling and decoupling. *Nature Neuroscience* **4,** 1259–1264. doi:`10.1038/nn759` (2001).

49. Miltner, W. H., Braun, C., Arnold, M., Witte, H. & Taub, E. Coherence of gamma-band EEG activity as a basis for associative learning. *Nature* **397,** 434–436. doi:`10.1038/17126` (4, 1999).

50. Hyafil, A., Giraud, A.-L., Fontolan, L. & Gutkin, B. Neural Cross-Frequency Coupling: Connecting Architectures, Mechanisms, and Functions. *Trends in Neurosciences* **38,** 725–740. doi:`10.1016/j.tins.2015.09.001`. (2024) (1, 2015).

51. Buzsáki, G. *Rhythms of the brain.* xv, 448–xv, 448. doi:`10.1093/acprof:oso/9780195301069.001.0001` (Oxford University Press, New York, NY, US, 2006).

52. *EEG Recording and Brain Waves — BioSerendipity* (2024).

53. Cherninskyi, A. *Sample of human EEG with prominent resting state activity - alpha-rhythm.* (2024).

54. Fries, P. Rhythms for Cognition: Communication through Coherence. *Neuron* **88,** 220–235. doi:`10.1016/j.neuron.2015.09.034`. (2024) (7, 2015).

55. Yu, M. Benchmarking metrics for inferring functional connectivity from multi-channel EEG and MEG: A simulation study. *Chaos: An Interdisciplinary Journal of Nonlinear Science* **30,** 123124. doi:`10.1063/5.0018826` (2020).

56. Bastos, A. M. & Schoffelen, J.-M. A Tutorial Review of Functional Connectivity Analysis Methods and Their Interpretational Pitfalls. *Frontiers in Systems Neuroscience* **9.** (2024) (2016).

57. Stam, C. J., Nolte, G. & Daffertshofer, A. Phase lag index: Assessment of functional connectivity from multi channel EEG and MEG with diminished bias from common sources. *Human Brain Mapping* **28,** 1178–1193. doi:`10.1002/hbm.20346`. (2023) (2007).

58. Mohammadi, Y. & Moradi, M. H. Prediction of Depression Severity Scores Based on Functional Connectivity and Complexity of the EEG Signal. *Clinical EEG and Neuroscience* **52,** 52–60. doi:`10.1177/1550059420965431`. (2024) (1, 2021).

59. Thomas Yeo, B. T. *et al.* The organization of the human cerebral cortex estimated by intrinsic functional connectivity. *Journal of Neurophysiology* **106,** 1125–1165. doi:`10.1152/jn.00338.2011`. (2024) (2011).

60. Başar, E. & Güntekin, B. in *Supplements to Clinical Neurophysiology* (eds Başar, E., Başar-Eroĝlu, C., Özerdem, A., Rossini, P. M. & Yener, G. G.) 303–341 (Elsevier, 1, 2013). doi:`10.1016/B978-0-7020-5307-8.00019-3`. (2024).

61. Nimmrich, V., Draguhn, A. & Axmacher, N. Neuronal Network Oscillations in Neurodegenerative Diseases. *NeuroMolecular Medicine* **17,** 270–284. doi:`10.1007/s12017-015-8355-9`. (2024) (1, 2015).

62. Bullmore, E. & Sporns, O. Complex brain networks: graph theoretical analysis of structural and functional systems. *Nature Reviews Neuroscience* **10,** 186–198. doi:`10.1038/nrn2575`. (2024) (2009).

63. Wu, J. W. *et al.* Neuronal activity enhances tau propagation and tau pathology in vivo. *Nature Neuroscience* **19,** 1085–1092. doi:`10.1038/nn.4328`. (2023) (2016).

64. Pooler, A. M., Phillips, E. C., Lau, D. H. W., Noble, W. & Hanger, D. P. Physiological release of endogenous tau is stimulated by neuronal activity. *EMBO reports* **14,** 389–394. doi:`10.1038/embor.2013.15`. (2023) (2013).

65. Sokolow, S. *et al.* Pre-synaptic C-terminal truncated tau is released from cortical synapses in Alzheimer's disease. *Journal of Neurochemistry* **133,** 368–379. doi:`10.1111/JNC.12991` (3 2015).

66. Wu, Q. *et al.* Neuronal activity modulates alpha-synuclein aggregation and spreading in organotypic brain slice cultures and in vivo. *Acta neuropathologica* **140,** 831–849. doi:`10.1007/s00401-020-02227-6`. (2024) (2020).

67. Fortin, D. L. *et al.* Neural Activity Controls the Synaptic Accumulation of alpha-Synuclein. *The Journal of Neuroscience* **25,** 10913–10921. doi:`10.1523/JNEUROSCI.2922-05.2005`. (2024) (23, 2005).

68. Bloom, G. S. Amyloid-beta and tau: the trigger and bullet in Alzheimer disease pathogenesis. *JAMA neurology* **71,** 505–508. doi:`10.1001/jamaneurol.2013.5847` (2014).

69. Burns, A. & Iliffe, S. Alzheimer's disease. *BMJ* **338.** doi:`10.1136/bmj.b158` (2009).

70. Alzheimer's Association. 2020 Alzheimer's disease facts and figures. *Alzheimer's & Dementia* **16,** 391–460 (2020).

71. C., P. *World Alzheimer Report 2018. The State of the Art of Dementia Reserach: New Frontiers* 2018.

72. Holtzman, D. M., Morris, J. C. & Goate, A. M. Alzheimer's Disease: The Challenge of the Second Century. *Science Translational Medicine* **3,** 77sr1–77sr1. doi:`10.1126/scitranslmed.3002369` (2011).

73. Jack Clifford R., J. *et al.* Prevalence of Biologically vs Clinically Defined Alzheimer Spectrum Entities Using the National Institute on Aging–Alzheimer's Association Research Framework. *JAMA Neurology* **76,** 1174–1183. doi:`10.1001/jamaneurol.2019.1971` (2019).

74. Sevigny, J. *et al.* The antibody aducanumab reduces Abeta plaques in Alzheimer's disease. *Nature* **537,** 50–56. doi:`10.1038/nature19323` (7618 2016).

75. Alexander, G. C. & Karlawish, J. The Problem of Aducanumab for the Treatment of Alzheimer Disease. *Annals of Internal Medicine.* doi:`10.7326/M21-2603` (2021).

76. Walsh, S., Merrick, R., Milne, R. & Brayne, C. Aducanumab for Alzheimers disease? *BMJ* **374.** doi:`10.1136/bmj.n1682` (2021).

77. Van der Kant, R., Goldstein, L. S. B. & Ossenkoppele, R. Amyloid-β-independent regulators of tau pathology in Alzheimer disease. *Nature Reviews Neuroscience* **21,** 21–35. doi:`10.1038/s41583-019-0240-3` (2020).

78. Duyckaerts, C., Clavaguera, F. & Potier, M.-C. The prion-like propagation hypothesis in Alzheimer's and Parkinson's disease. *Current Opinion in Neurology* **32** (2019).

79. Cho, H. *et al.* In vivo cortical spreading pattern of tau and amyloid in the Alzheimer disease spectrum. *Annals of Neurology* **80,** 247–258. doi:`https://doi.org/10.1002/ana.24711` (2016).

80. Mrdjen, D. *et al.* The basis of cellular and regional vulnerability in Alzheimer's disease. *Acta neuropathologica* **138,** 729–749. doi:`10.1007/s00401-019-02054-4` (2019).

81. Arnold, S. E., Hyman, B. T., Flory, J., Damasio, A. R. & Van Hoesen, G. W. The Topographical and Neuroanatomical Distribution of Neurofibrillary Tangles and Neuritic Plaques in the Cerebral Cortex of Patients with Alzheimer's Disease. *Cerebral Cortex* **1,** 103–116. doi:`10.1093/cercor/1.1.103` (1991).

82. Liu, L. *et al.* Trans-Synaptic Spread of Tau Pathology In Vivo. *PLOS ONE* **7,** 1–9. doi:`10.1371/journal.pone.0031302` (2012).

83. Vogel, J. W., Iturria-Medina, Y., Strandberg, O. T., Initiative, A. D. N. & the Swedish BioFinder Study. Spread of pathological tau proteins through communicating neurons in human Alzheimer's disease. *Nature Communications* **11,** 2612. doi:`10.1038/s41467-020-15701-2` (2020).

84. Cho, H. *et al.* Progressive Tau Accumulation in Alzheimer Disease: 2-Year Follow-up Study. *Journal of Nuclear Medicine* **60,** 1611–1621. doi:`10.2967/jnumed.118.221697` (2019).

85. Harrison, T. M. *et al.* Longitudinal tau accumulation and atrophy in aging and alzheimer disease. *Annals of Neurology* **85,** 229–240. doi:`https://doi.org/10.1002/ana.25406` (2019).

86. Pontecorvo, M. J. *et al.* A multicentre longitudinal study of flortaucipir (18F) in normal ageing, mild cognitive impairment and Alzheimer's disease dementia. *Brain* **142,** 1723–1735. doi:`10.1093/brain/awz090` (2019).

87. Brier, M. R. *et al.* Tau and Aβ imaging, CSF measures, and cognition in Alzheimer's disease. *Science Translational Medicine* **8,** 338ra66–338ra66. doi:`10.1126/scitranslmed.aaf2362` (2016).

88. La Joie, R. *et al.* Prospective longitudinal atrophy in Alzheimer's disease correlates with the intensity and topography of baseline tau-PET. *Science Translational Medicine* **12.** doi:`10.1126/scitranslmed.aau5732` (2020).

89. Wang, L. *et al.* Evaluation of Tau Imaging in Staging Alzheimer Disease and Revealing Interactions Between β-Amyloid and Tauopathy. *JAMA Neurology* **73,** 1070–1077. doi:`10.1001/jamaneurol.2016.2078` (2016).

90. Pontecorvo, M. J. *et al.* Relationships between flortaucipir PET tau binding and amyloid burden, clinical diagnosis, age and cognition. *Brain* **140,** 748–763. doi:`10.1093/brain/aww334` (2017).

91. Hardy, J. Amyloid, the presenilins and Alzheimer's disease. *Trends in Neurosciences* **20,** 154–159. doi:`https://doi.org/10.1016/S0166-2236(96)01030-2` (1997).

92. Haass, C. & Selkoe, D. J. Soluble protein oligomers in neurodegeneration: lessons from the Alzheimer's amyloid β-peptide. *Nature Reviews Molecular Cell Biology* **8,** 101–112. doi:`10.1038/nrm2101` (2007).

93. Brorson, J. R. *et al.* The Ca2+ influx induced by beta-amyloid peptide 25–35 in cultured hippocampal neurons results from network excitation. *Journal of Neurobiology* **26,** 325–338. doi:`https://doi.org/10.1002/neu.480260305` (1995).

94. Busche, M. A. *et al.* Clusters of Hyperactive Neurons Near Amyloid Plaques in a Mouse Model of Alzheimer's Disease. *Science* **321,** 1686–1689. doi:`10.1126/science.1162844` (2008).

95. Sanchez-Mejia, R. O. *et al.* Phospholipase A2 reduction ameliorates cognitive deficits in a mouse model of Alzheimer's disease. *Nature Neuroscience* **11,** 1311–1318. doi:`10.1038/nn.2213` (2008).

96. Ye, C. P., Selkoe, D. J. & Hartley, D. M. Protofibrils of amyloid beta-protein inhibit specific K+ currents in neocortical cultures. *Neurobiology of Disease* **13,** 177–190. doi:`https://doi.org/10.1016/S0969-9961(03)00068-8` (2003).

97. Busche, M. A. *et al.* Tau impairs neural circuits, dominating amyloid-β effects, in Alzheimer models in vivo. *Nature Neuroscience* **22,** 57–64. doi:`10.1038/s41593-018-0289-8` (2019).

98. Keskin, A. D. *et al.* BACE inhibition-dependent repair of Alzheimer's pathophysiology. *Proceedings of the National Academy of Sciences* **114,** 8631–8636. doi:`10.1073/pnas.1708106114` (2017).

99. Harris, S. S., Wolf, F., De Strooper, B. & Busche, M. A. Tipping the Scales: Peptide-Dependent Dysregulation of Neural Circuit Dynamics in Alzheimer's Disease. *Neuron* **107,** 417–435. doi:`https://doi.org/10.1016/j.neuron.2020.06.005` (2020).

100. Ciccone, R. *et al.* Amyloid β-Induced Upregulation of Nav1.6 Underlies Neuronal Hyperactivity in Tg2576 Alzheimer's Disease Mouse Model. *Scientific Reports* **9,** 13592. doi:`10.1038/s41598-019-50018-1` (2019).

101. Verret, L. *et al.* Inhibitory Interneuron Deficit Links Altered Network Activity and Cognitive Dysfunction in Alzheimer Model. *Cell* **149,** 708–721. doi:`https://doi.org/10.1016/j.cell.2012.02.046` (2012).

102. Mandelkow, E.-M. & Mandelkow, E. Tau in Alzheimer's disease. *Trends in Cell Biology* **8,** 425–427. doi:`https://doi.org/10.1016/S0962-8924(98)01368-3` (1998).

103. Binder, L. I., Guillozet-Bongaarts, A. L., Garcia-Sierra, F. & Berry, R. W. Tau, tangles, and Alzheimer's disease. *Biochimica et Biophysica Acta (BBA) - Molecular Basis of Disease* **1739,** 216–223. doi:`https://doi.org/10.1016/j.bbadis.2004.08.014` (2005).

104. Marinković, P. *et al.* In vivo imaging reveals reduced activity of neuronal circuits in a mouse tauopathy model. *Brain* **142,** 1051–1062. doi:`10.1093/brain/awz035` (2019).

105. Rocher, A. *et al.* Structural and functional changes in tau mutant mice neurons are not linked to the presence of NFTs. *Experimental Neurology* **223,** 385–393. doi:`https://doi.org/10.1016/j.expneurol.2009.07.029` (2010).

106. Hatch, R. J., Wei, Y., Xia, D. & Götz, J. Hyperphosphorylated tau causes reduced hippocampal CA1 excitability by relocating the axon initial segment. *Acta neuropathologica* **133,** 717–730. doi:`10.1007/s00401-017-1674-1` (2017).

107. Müller-Thomsen, L. *et al.* Consequences of hyperphosphorylated tau on the morphology and excitability of hippocampal neurons in aged tau transgenic mice. *Neurobiology of Aging* **93,** 109–123. doi:`https://doi.org/10.1016/j.neurobiolaging.2020.03.007` (2020).

108. Hoover, B. R. *et al.* Tau Mislocalization to Dendritic Spines Mediates Synaptic Dysfunction Independently of Neurodegeneration. *Neuron* **68,** 1067–1081. doi:`https://doi.org/10.1016/j.neuron.2010.11.030` (2010).

109. Fu, H. *et al.* A tau homeostasis signature is linked with the cellular and regional vulnerability of excitatory neurons to tau pathology. *Nature Neuroscience* **22,** 47–56. doi:`10.1038/s41593-018-0298-7` (2019).

110. Salvadores, N., Gerónimo-Olvera, C. & Court, F. A. Axonal Degeneration in AD: The Contribution of Abeta and Tau. *Frontiers in Aging Neuroscience* **12,** 581767. doi:`10.3389/fnagi.2020.581767`. (2024) (15, 2020).

111. Angulo, S. *et al.* Tau and amyloid-related pathologies in the entorhinal cortex have divergent effects in the hippocampal circuit. *Neurobiology of Disease* **108,** 261–276. doi:`https://doi.org/10.1016/j.nbd.2017.08.015` (2017).

112. Maia, L. F. *et al.* Changes in Amyloid-β and Tau in the Cerebrospinal Fluid of Transgenic Mice Overexpressing Amyloid Precursor Protein. *Science Translational Medicine* **5,** 194re2–194re2. doi:`10.1126/scitranslmed.3006446` (2013).

113. Sturchler-Pierrat, C. *et al.* Two amyloid precursor protein transgenic mouse models with Alzheimer disease-like pathology. *National Academy of Sciences* **94,** 13287–13292. doi:`10.1073/pnas.94.24.13287` (1997).

114. Adams, J. N., Maass, A., Harrison, T. M., Baker, S. L. & Jagust, W. J. Cortical tau deposition follows patterns of entorhinal functional connectivity in aging. *eLife* **8,** e49132. doi:`10.7554/eLife.49132` (2019).

115. Jacobs, H. I. L. *et al.* Structural tract alterations predict downstream tau accumulation in amyloid-positive older individuals. *Nature Neuroscience* **21,** 424–431. doi:`10.1038/s41593-018-0070-z` (2018).

116. Wang, L. *et al.* Evaluation of Tau Imaging in Staging Alzheimer Disease and Revealing Interactions Between β-Amyloid and Tauopathy. *JAMA Neurology* **73,** 1070–1077. doi:`10.1001/jamaneurol.2016.2078` (2016).

117. Pascoal, T. A. *et al.* Amyloid-β and hyperphosphorylated tau synergy drives metabolic decline in preclinical Alzheimer's disease. *Molecular Psychiatry* **22,** 306–311. doi:`10.1038/mp.2016.37` (2017).

118. Hulbert, S. & Adeli, H. EEG/MEG- and imaging-based diagnosis of Alzheimer's disease. *Reviews in the Neurosciences* **24,** 563–576. doi:`10.1515/revneuro-2013-0042.` (2024) (1, 2013).

119. Gaubert, S. *et al.* EEG evidence of compensatory mechanisms in preclinical Alzheimer's disease. *Brain* **142,** 2096–2112. doi:`10.1093/brain/awz150` (2019).

120. Liu, X. *et al.* Multiple characteristics analysis of Alzheimer's electroencephalogram by power spectral density and Lempel–Ziv complexity. *Cognitive Neurodynamics* **10,** 121–133. doi:`10.1007/s11571-015-9367-8` (2016).

121. Lizio, R. *et al.* Neurophysiological Assessment of Alzheimer's Disease Individuals by a Single Electroencephalographic Marker. *Journal of Alzheimer's Disease* **49,** 159–177. doi:`10.3233/JAD-143042` (2016).

122. Schmidt, M. *et al.* Index of Alpha/Theta Ratio of the Electroencephalogram: A New Marker for Alzheimer's Disease. *Frontiers in Aging Neuroscience* **5,** 60. doi:`10.3389/fnagi.2013.00060` (2013).

123. Wang, R. *et al.* Power spectral density and coherence analysis of Alzheimer's EEG. *Cognitive neurodynamics* **9,** 291–304. doi:`10.1007/s11571-014-9325-x` (2015).

124. Garn, H. *et al.* Quantitative EEG markers relate to Alzheimer's disease severity in the Prospective Dementia Registry Austria (PRODEM). *Clinical Neurophysiology* **126,** 505–513. doi:`https://doi.org/10.1016/j.clinph.2014.07.005` (2015).

125. Moretti, D. V. Association of EEG, MRI, and regional blood flow biomarkers is predictive of prodromal Alzheimer's disease. *Neuropsychiatric disease and treatment* **11,** 2779–2791. doi:`10.2147/NDT.S93253` (2015).

126. de Waal, H. *et al.* Young Alzheimer patients show distinct regional changes of oscillatory brain dynamics. *Neurobiology of Aging* **33,** 1008.e25–1008.e31. doi:`https://doi.org/10.1016/j.neurobiolaging.2011.10.013` (2012).

127. Bruña, R. *et al.* MEG Oscillatory Slowing in Cognitive Impairment is Associated with the Presence of Subjective Cognitive Decline. *Clinical EEG and Neuroscience.* doi:`10.1177/15500594221072708` (2022).

128. Devos, H. *et al.* EEG/ERP evidence of possible hyperexcitability in older adults with elevated beta-amyloid. *Translational Neurodegeneration* **11,** 8. doi:`10.1186/s40035-022-00282-5` (1 2022).

129. Weller, M. *et al.* Glioma. *Nature Reviews Disease Primers* **1,** 1–18. doi:`10.1038/nrdp.2015.17`. (2024) (16, 2015).

130. Liu, J., Shi, W. & Lin, Y. Interactive relationship between neuronal circuitry and glioma: A narrative review. *Glioma* **5,** 43. doi:`10.4103/glioma.glioma_15_22`. (2024) (2022).

131. Maas, D. A. & Douw, L. Multiscale network neuroscience in neuro-oncology: How tumors, brain networks, and behavior connect across scales. *Neuro-Oncology Practice* **10,** 506–517. doi:`10.1093/nop/npad044`. (2023) (1, 2023).

132. Hsieh, K., Tsai, R.-J., Teng, Y.-C. & Lo, C.-M. Effect of a computer-aided diagnosis system on radiologists' performance in grading gliomas with MRI. *PLOS ONE* **12,** e0171342. doi:`10.1371/journal.pone.0171342` (3, 2017).

133. Fox, M. E. & King, T. Z. Functional Connectivity in Adult Brain Tumor Patients: A Systematic Review. *Brain Connectivity* **8,** 381–397. doi:`10.1089/brain.2018.0623`. (2023) (2018).

134. Derks, J., Reijneveld, J. C. & Douw, L. Neural network alterations underlie cognitive deficits in brain tumor patients. *Current Opinion in Oncology* **26,** 627. doi:`10.1097/CCO.0000000000000126`. (2023) (2014).

135. Esposito, R. *et al.* Modifications of Default-Mode Network Connectivity in Patients with Cerebral Glioma. *PLOS ONE* **7,** e40231. doi:`10.1371/journal.pone.0040231`. (2023) (9, 2012).

136. Harris, R. J. *et al.* Altered functional connectivity of the default mode network in diffuse gliomas measured with pseudo-resting state fMRI. *Journal of Neuro-Oncology* **116,** 373–379. doi:`10.1007/s11060-013-1304-2`. (2023) (1, 2014).

137. Ghumman, S., Fortin, D., Noel-Lamy, M., Cunnane, S. C. & Whittingstall, K. Exploratory study of the effect of brain tumors on the default mode network. *Journal of Neuro-Oncology* **128,** 437–444. doi:`10.1007/s11060-016-2129-6`. (2023) (1, 2016).

138. Maesawa, S. *et al.* Evaluation of Resting State Networks in Patients with Gliomas: Connectivity Changes in the Unaffected Side and Its Relation to Cognitive Function. *PLOS ONE* **10,** e0118072. doi:`10.1371/journal.pone.0118072`. (2023) (6, 2015).

139. Bartolomei, F. *et al.* Disturbed functional connectivity in brain tumour patients: Evaluation by graph analysis of synchronization matrices. *Clinical Neurophysiology* **117,** 2039–2049. doi:`10.1016/j.clinph.2006.05.018`. (2023) (1, 2006).

140. Bartolomei, F. *et al.* How do brain tumors alter functional connectivity? A magnetoencephalography study. *Annals of Neurology* **59,** 128–138. doi:`10.1002/ana.20710`. (2023) (1, 2006).

141. Guggisberg, A. G. *et al.* Mapping Functional Connectivity in Patients with Brain Lesions. *Annals of neurology* **63,** 193–203. doi:`10.1002/ana.21224`. (2023) (2008).

142. Bosma, I. *et al.* Synchronized brain activity and neurocognitive function in patients with low-grade glioma: A magnetoencephalography study. *Neuro-Oncology* **10,** 734–744. doi:`10.1215/15228517-2008-034`. (2023) (2008).

143. Bosma, I. *et al.* Disturbed functional brain networks and neurocognitive function in low-grade glioma patients: a graph theoretical analysis of resting-state MEG. *Nonlinear Biomedical Physics* **3,** 9. doi:`10.1186/1753-4631-3-9` (23, 2009).

144. Van Dellen, E. *et al.* MEG Network Differences between Low- and High-Grade Glioma Related to Epilepsy and Cognition. *PLoS ONE* **7,** e50122. doi:`10.1371/journal.pone.0050122`. (2023) (14, 2012).

145. Xu, H. *et al.* Reduced efficiency of functional brain network underlying intellectual decline in patients with low-grade glioma. *Neuroscience Letters* **543,** 27–31. doi:`10.1016/j.neulet.2013.02.062`. (2023) (24, 2013).

146. Derks, J. *et al.* Understanding Global Brain Network Alterations in Glioma Patients. *Brain Connectivity* **11,** 865–874. doi:`10.1089/brain.2020.0801`. (2023) (1, 2021).

147. Coombes, S. & Wedgwood, K. C. A. *Neurodynamics: An Applied Mathematics Perspective* 1st ed. (Springer International Publishing AG, Cham, 2023).

148. Gerstner, W., Kistler, W. M., Naud, R. & Paninski, L. *Neuronal Dynamics: From Single Neurons to Networks and Models of Cognition* doi:`10.1017/CBO9781107447615`. (2024) (Cambridge University Press, Cambridge, 2014).

149. Cowan, J. D., Neuman, J. & van Drongelen, W. Wilson–Cowan Equations for Neocortical Dynamics. *The Journal of Mathematical Neuroscience* **6,** 1. doi:`10.1186/s13408-015-0034-5`. (2024) (4, 2016).

150. Ashwin, P., Coombes, S. & Nicks, R. Mathematical Frameworks for Oscillatory Network Dynamics in Neuroscience. *Journal of Mathematical Neuroscience* **6,** 2. doi:`10.1186/s13408-015-0033-6` (2016).

151. Bick, C., Goodfellow, M., Laing, C. R. & Martens, E. A. Understanding the dynamics of biological and neural oscillator networks through exact mean-field reductions: a review. *The Journal of Mathematical Neuroscience* **10,** 9. doi:`10.1186/s13408-020-00086-9`. (2023) (27, 2020).

152. Wilson, H. R. & Cowan, J. D. Excitatory and Inhibitory Interactions in Localized Populations of Model Neurons. *Biophysical Journal* **12,** 1–24. (2024) (1972).

153. Perko, L. *Differential Equations and Dynamical Systems* red. by Marsden, J. E., Sirovich, L. & Golubitsky, M. doi:`10.1007/978-1-4613-0003-8`. (2024) (Springer, New York, NY, 2001).

154. Deco, G., Jirsa, V., McIntosh, A. R., Sporns, O. & Kötter, R. Key role of coupling, delay, and noise in resting brain fluctuations. *Proceedings of the National Academy of Sciences* **106,** 10302–10307. doi:`10.1073/pnas.0901831106` (2009).

155. Cabral, J., Hugues, E., Sporns, O. & Deco, G. Role of local network oscillations in resting-state functional connectivity. *NeuroImage* **57,** 130–139. doi:`10.1016/j.neuroimage.2011.04.010`. (2023) (1, 2011).

156. Freyer, F. *et al.* Biophysical Mechanisms of Multistability in Resting-State Cortical Rhythms. *Journal of Neuroscience* **31,** 6353–6361. doi:`10.1523/JNEUROSCI.6693-10.2011`. (2023) (27, 2011).

157. Deco, G., Jirsa, V. K. & McIntosh, A. R. Emerging concepts for the dynamical organization of resting-state activity in the brain. *Nature Reviews Neuroscience* **12,** 43–56. doi:`10.1038/nrn2961`. (2023) (2011).

158. Jirsa, V. K. *et al.* The Virtual Epileptic Patient: Individualized whole-brain models of epilepsy spread. *NeuroImage. Individual Subject Prediction* **145,** 377–388. doi:`10.1016/j.neuroimage.2016.04.049`. (2023) (15, 2017).

159. Taylor, P. N., Kaiser, M. & Dauwels, J. Structural connectivity based whole brain modelling in epilepsy. *Journal of Neuroscience Methods* **236,** 51–57. doi:`10.1016/j.jneumeth.2014.08.010`. (2023) (30, 2014).

160. Demirtaş, M. *et al.* A whole-brain computational modeling approach to explain the alterations in resting-state functional connectivity during progression of Alzheimer's disease. *NeuroImage: Clinical* **16,** 343–354. doi:`10.1016/j.nicl.2017.08.006`. (2023) (1, 2017).

161. Goriely, A., Kuhl, E. & Bick, C. Neuronal Oscillations on Evolving Networks: Dynamics, Damage, Degradation, Decline, Dementia, and Death. *Physical Review Letters* **125,** 128102. doi:`10.1103/PhysRevLett.125.128102` (2020).

162. Cabral, J. *et al.* Structural connectivity in schizophrenia and its impact on the dynamics of spontaneous functional networks. *Chaos: An Interdisciplinary Journal of Nonlinear Science* **23,** 046111. doi:`10.1063/1.4851117`. (2023) (23, 2013).

163. Anticevic, A. *et al.* NMDA receptor function in large-scale anticorrelated neural systems with implications for cognition and schizophrenia. *Proceedings of the National Academy of Sciences* **109,** 16720–16725. doi:`10.1073/pnas.1208494109`. (2023) (9, 2012).

164. Yang, G. J. *et al.* Altered global brain signal in schizophrenia. *Proceedings of the National Academy of Sciences* **111,** 7438–7443. doi:`10.1073/pnas.1405289111`. (2023) (20, 2014).

165. Alstott, J., Breakspear, M., Hagmann, P., Cammoun, L. & Sporns, O. Modeling the Impact of Lesions in the Human Brain. *PLoS Computational Biology* **5.** doi:`10.1371/journal.pcbi.1000408`. (2023) (2009).

166. Aerts, H., Fias, W., Caeyenberghs, K. & Marinazzo, D. Brain networks under attack: robustness properties and the impact of lesions. *Brain* **139,** 3063–3083. doi:`10.1093/brain/aww194`. (2023) (1, 2016).

167. Aerts, H. *et al.* Modeling Brain Dynamics in Brain Tumor Patients Using the Virtual Brain. *eNeuro* **5.** doi:`10.1523/ENEURO.0083-18.2018`. (2023) (1, 2018).

168. Aerts, H. *et al.* Modeling brain dynamics after tumor resection using The Virtual Brain. *NeuroImage* **213,** 116738. doi:`10.1016/j.neuroimage.2020.116738` (2020).

169. Ton, R., Deco, G. & Daffertshofer, A. Structure-Function Discrepancy: Inhomogeneity and Delays in Synchronized Neural Networks. *PLOS Computational Biology* **10,** e1003736. doi:`10.1371/journal.pcbi.1003736`. (2024) (31, 2014).

170. Raj, A., Kuceyeski, A. & Weiner, M. A network diffusion model of disease progression in dementia. *Neuron* **73,** 1204–1215. doi:`10.1016/j.neuron.2011.12.040` (22, 2012).

171. Weickenmeier, J., Jucker, M., Goriely, A. & Kuhl, E. A physics-based model explains the prion-like features of neurodegeneration in Alzheimer's disease, Parkinson's disease, and amyotrophic lateral sclerosis. *Journal of the Mechanics and Physics of Solids* **124,** 264–281. doi:`10.1016/j.jmps.2018.10.013` (2019).

172. Weickenmeier, J., Kuhl, E. & Goriely, A. Multiphysics of Prionlike Diseases: Progression and Atrophy. *Physical Review Letters* **121,** 158101. doi:`10.1103/PhysRevLett.121.158101`. (2023) (12, 2018).

173. Thompson, T. B., Chaggar, P., Kuhl, E., Goriely, A. & Alzheimer's Disease Neuroimaging Initiative. Protein-protein interactions in neurodegenerative diseases: A conspiracy theory. *PLoS computational biology* **16,** e1008267. doi:`10.1371/journal.pcbi.1008267` (2020).

174. Bennett, R. E. *et al.* Enhanced Tau Aggregation in the Presence of Amyloid beta. *The American Journal of Pathology* **187,** 1601–1612. doi:`10.1016/j.ajpath.2017.03.011`. (2024) (1, 2017).

175. Zhang, Y., Wu, K.-M., Yang, L., Dong, Q. & Yu, J.-T. Tauopathies: new perspectives and challenges. *Molecular Neurodegeneration* **17,** 28. doi:`10.1186/s13024-022-00533-z`. (2024) (7, 2022).

176. Thompson, T. B., Chaggar, P., Kuhl, E., Goriely, A. & for the Alzheimer's Disease Neuroimaging Initiative. Protein-protein interactions in neurodegenerative diseases: A conspiracy theory. *PLOS Computational Biology* **16,** 1–41. doi:`10.1371/journal.pcbi.1008267` (2020).

177. Goriely, A., Kuhl, E. & Bick, C. Neuronal Oscillations on Evolving Networks: Dynamics, Damage, Degradation, Decline, Dementia, and Death. *Physical Review Letters* **125.** doi:`10.1103/physrevlett.125.128102` (2020).

178. Vogel, J. W., Iturria-Medina, Y., Strandberg, O. T., Initiative, A. D. N. & the Swedish BioFinder Study. Spread of pathological tau proteins through communicating neurons in human Alzheimer's disease. *Nature Communications* **11,** 2612. doi:`10.1038/s41467-020-15701-2` (2020).

179. Cho, H. *et al.* Progressive Tau Accumulation in Alzheimer Disease: 2-Year Follow-up Study. *Journal of Nuclear Medicine* **60,** 1611–1621. doi:`10.2967/jnumed.118.221697` (2019).

180. Harrison, T. M. *et al.* Longitudinal tau accumulation and atrophy in aging and alzheimer disease. *Annals of Neurology* **85,** 229–240. doi:`https://doi.org/10.1002/ana.25406` (2019).

181. Pontecorvo, M. J. *et al.* A multicentre longitudinal study of flortaucipir in normal ageing, mild cognitive impairment and Alzheimer's disease dementia. *Brain* **142,** 1723–1735. doi:`10.1093/brain/awz090` (2019).

182. Busche, M. A. *et al.* Tau impairs neural circuits, dominating amyloid-β effects, in Alzheimer models in vivo. *Nature Neuroscience* **22,** 57–64. doi:`10.1038/s41593-018-0289-8` (2019).

183. Deco, G. *et al.* Single or multiple frequency generators in on-going brain activity: A mechanistic whole-brain model of empirical MEG data. *NeuroImage* **152,** 538–550. doi:`https://doi.org/10.1016/j.neuroimage.2017.03.023` (2017).

184. Szalkai, B., Kerepesi, C., Varga, B. & Grolmusz, V. Parameterizable consensus connectomes from the Human Connectome Project: the Budapest Reference Connectome Server v3.0. *Cognitive neurodynamics* **11,** 113–116. doi:`10.1007/s11571-016-9407-z` (2017).

185. Swadlow, H. A. Efferent neurons and suspected interneurons in S-1 forelimb representation of the awake rabbit: receptive fields and axonal properties. *Journal of Neurophysiology* **63,** 1477–1498. doi:`10.1152/jn.1990.63.6.1477` (1990).

186. Braak, H. & Braak, E. Neuropathological stageing of Alzheimer-related changes. *Acta Neuropathologica* **82,** 239–259. doi:`10.1007/BF00308809`. (2024) (1, 1991).

187. Mattsson, N., Palmqvist, S., Stomrud, E., Vogel, J. & Hansson, O. Staging β-Amyloid Pathology With Amyloid Positron Emission Tomography. *JAMA Neurology* **76,** 1319–1329. doi:`10.1001/jamaneurol.2019.2214` (2019).

188. Nakao, H. Phase reduction approach to synchronisation of nonlinear oscillators. *Contemporary Physics* **57,** 188–214. doi:`10.1080/00107514.2015.1094987` (2 2016).

189. Bhattacharya, B. S., Coyle, D. & Maguire, L. P. A thalamo–cortico–thalamic neural mass model to study alpha rhythms in Alzheimer's disease. *Neural Networks* **24,** 631–645. doi:`https://doi.org/10.1016/j.neunet.2011.02.009` (2011).

190. Segneri, M., Bi, H., Olmi, S. & Torcini, A. Theta-Nested Gamma Oscillations in Next Generation Neural Mass Models. *Frontiers in Computational Neuroscience* **14,** 47. doi:`10.3389/fncom.2020.00047` (2020).

191. Chehelcheraghi, M., Nakatani, C., Steur, E. & van Leeuwen, C. A neural mass model of phase–amplitude coupling. *Biological Cybernetics* **110,** 171–192. doi:`10.1007/s00422-016-0687-5` (2 2016).

192. Qin, Y., Menara, T., Bassett, D. S. & Pasqualetti, F. Phase-amplitude coupling in neuronal oscillator networks. *Phys. Rev. Research* **3,** 23218. doi:`10.1103/PhysRevResearch.3.023218` (2 2021).

193. Stefanovski, L. *et al.* Linking Molecular Pathways and Large-Scale Computational Modeling to Assess Candidate Disease Mechanisms and Pharmacodynamics in Alzheimer's Disease. *Frontiers in Computational Neuroscience* **13,** 54. doi:`10.3389/fncom.2019.00054` (2019).

194. Harris, S. S., Wolf, F., De Strooper, B. & Busche, M. A. Tipping the Scales: Peptide-Dependent Dysregulation of Neural Circuit Dynamics in Alzheimer's Disease. *Neuron* **107,** 417–435. doi:`https://doi.org/10.1016/j.neuron.2020.06.005` (2020).

195. Pooler, A. M., Phillips, E. C., Lau, D. H., Noble, W. & Hanger, D. P. Physiological release of endogenous tau is stimulated by neuronal activity. *EMBO reports* **14,** 389–394. doi:`10.1038/EMBOR.2013.15` (4 2013).

196. Thiele, M., Berner, R., Tass, P. A., Schöll, E. & Yanchuk, S. Asymmetric adaptivity induces recurrent synchronization in complex networks. *Chaos: An Interdisciplinary Journal of Nonlinear Science* **33,** 023123. doi:`10.1063/5.0128102.` (2023) (15, 2023).

197. Erdös, P. & Rényi, A. On Random Graphs I. *Publicationes Mathematicae Debrecen* **6,** 290 (1959).

198. Duits, F. H. *et al.* Four subgroups based on tau levels in Alzheimer's disease observed in two independent cohorts. *Alzheimer's Research & Therapy* **13,** 2. doi:`10.1186/s13195-020-00713-3.` (2023) (4, 2021).

199. Ferreira, D., Nordberg, A. & Westman, E. Biological subtypes of Alzheimer disease: A systematic review and meta-analysis. *Neurology* **94,** 436–448. doi:`10.1212/WNL.0000000000009058`. (2023) (10, 2020).

200. Wu, J. W. *et al.* Neuronal activity enhances tau propagation and tau pathology in vivo. *Nature Neuroscience 2016 19:8* **19,** 1085–1092. doi:`10.1038/nn.4328` (8 2016).

201. Seemiller, J. *et al.* Indication of retrograde tau spreading along Braak stages and functional connectivity pathways. *European Journal of Nuclear Medicine and Molecular Imaging* **48,** 2272–2282. doi:`10.1007/s00259-020-05183-1`. (2023) (1, 2021).

202. Franzmeier, N. *et al.* Functional brain architecture is associated with the rate of tau accumulation in Alzheimer's disease. *Nature Communications* **11,** 347. doi:`10.1038/s41467-019-14159-1`. (2023) (17, 2020).

203. Szalkai, B., Kerepesi, C., Varga, B. & Grolmusz, V. Parameterizable consensus connectomes from the Human Connectome Project: the Budapest Reference Connectome Server v3.0. *Cognitive Neurodynamics* **11,** 113–116. doi:`10.1007/s11571-016-9407-z` (2017).

204. Freyer, F., Roberts, J. A., Ritter, P. & Breakspear, M. A Canonical Model of Multistability and Scale-Invariance in Biological Systems. *PLOS Computational Biology* **8,** e1002634. doi:`10.1371/journal.pcbi.1002634`. (2023) (9, 2012).

205. Robinson, P. A., Rennie, C. J. & Rowe, D. L. Dynamics of large-scale brain activity in normal arousal states and epileptic seizures. *Physical Review E* **65,** 041924. doi:`10.1103/PhysRevE.65.041924`. (2023) (11, 2002).

206. Cocchi, L., Gollo, L. L., Zalesky, A. & Breakspear, M. Criticality in the brain: A synthesis of neurobiology, models and cognition. *Progress in Neurobiology* **158,** 132–152. doi:`10.1016/j.pneurobio.2017.07.002`. (2023) (1, 2017).

207. Cabral, J., Kringelbach, M. L. & Deco, G. Exploring the network dynamics underlying brain activity during rest. *Progress in Neurobiology* **114,** 102–131. doi:`10.1016/j.pneurobio.2013.12.005`. (2023) (1, 2014).

208. Hansen, E. C. A., Battaglia, D., Spiegler, A., Deco, G. & Jirsa, V. K. Functional connectivity dynamics: Modeling the switching behavior of the resting state. *NeuroImage* **105,** 525–535. doi:`10.1016/j.neuroimage.2014.11.001`. (2023) (15, 2015).

209. Van Nifterick, A. M. *et al.* A multiscale brain network model links Alzheimer's disease-mediated neuronal hyperactivity to large-scale oscillatory slowing. *Alzheimer's Research & Therapy* **14,** 101. doi:`10.1186/s13195-022-01041-4` (25, 2022).

210. Byrne, Á., Brookes, M. J. & Coombes, S. A mean field model for movement induced changes in the beta rhythm. *Journal of computational neuroscience* **43,** 143–158. doi:`10.1007/s10827-017-0655-7` (2017).

211. Montbrió, E., Pazó, D. & Roxin, A. Macroscopic Description for Networks of Spiking Neurons. *Physical Review X* **5,** 021028. doi:`10.1103/PhysRevX.5.021028`. (2024) (19, 2015).

212. Kiss, I. Z., Miller, J. C. & Simon, P. L. *Mathematics of epidemics on networks : from exact to approximate models* (Springer, Cham, Switzerland, 2017).

213. Louis, D. N. *et al.* The 2021 WHO Classification of Tumors of the Central Nervous System: a summary. *Neuro-Oncology* **23,** 1231–1251. doi:`10.1093/neuonc/noab106` (2, 2021).

214. Breedt, L. C. *et al.* Multimodal multilayer network centrality relates to executive functioning. *Network Neuroscience* **7,** 299–321. doi:`10.1162/netn_a_00284`. (2023) (1, 2023).

215. Tzourio-Mazoyer, N. *et al.* Automated Anatomical Labeling of Activations in SPM Using a Macroscopic Anatomical Parcellation of the MNI MRI Single-Subject Brain. *NeuroImage* **15,** 273–289. doi:`10.1006/nimg.2001.0978`. (2023) (1, 2002).

216. Hillebrand, A. *et al.* Direction of information flow in large-scale resting-state networks is frequency-dependent. *Proceedings of the National Academy of Sciences* **113,** 3867–3872. doi:`10.1073/pnas.1515657113`. (2023) (5, 2016).

217. Hillebrand, A., Barnes, G. R., Bosboom, J. L., Berendse, H. W. & Stam, C. J. Frequency-dependent functional connectivity within resting-state networks: An atlas-based MEG beamformer solution. *NeuroImage* **59,** 3909–3921. doi:`10.1016/j.neuroimage.2011.11.005`. (2023) (15, 2012).

218. Andersson, J. L. R., Skare, S. & Ashburner, J. How to correct susceptibility distortions in spin-echo echo-planar images: application to diffusion tensor imaging. *NeuroImage* **20,** 870–888. doi:`10.1016/S1053-8119(03)00336-7`. (2023) (1, 2003).

219. Smith, R. E., Tournier, J.-D., Calamante, F. & Connelly, A. Anatomically-constrained tractography: Improved diffusion MRI streamlines tractography through effective use of anatomical information. *NeuroImage* **62,** 1924–1938. doi:`10.1016/j.neuroimage.2012.06.005`. (2023) (1, 2012).

220. Tournier, J.-D. *et al.* MRtrix3: A fast, flexible and open software framework for medical image processing and visualisation. *NeuroImage* **202,** 116137. doi:`10.1016/j.neuroimage.2019.116137`. (2023) (15, 2019).

221. Jeurissen, B., Tournier, J.-D., Dhollander, T., Connelly, A. & Sijbers, J. Multi-tissue constrained spherical deconvolution for improved analysis of multi-shell diffusion MRI data. *NeuroImage* **103,** 411–426. doi:`10.1016/j.neuroimage.2014.07.061`. (2023) (1, 2014).

222. Smith, R. E., Tournier, J.-D., Calamante, F. & Connelly, A. SIFT2: Enabling dense quantitative assessment of brain white matter connectivity using streamlines tractography. *NeuroImage* **119,** 338–351. doi:`10.1016/j.neuroimage.2015.06.092`. (2023) (1, 2015).